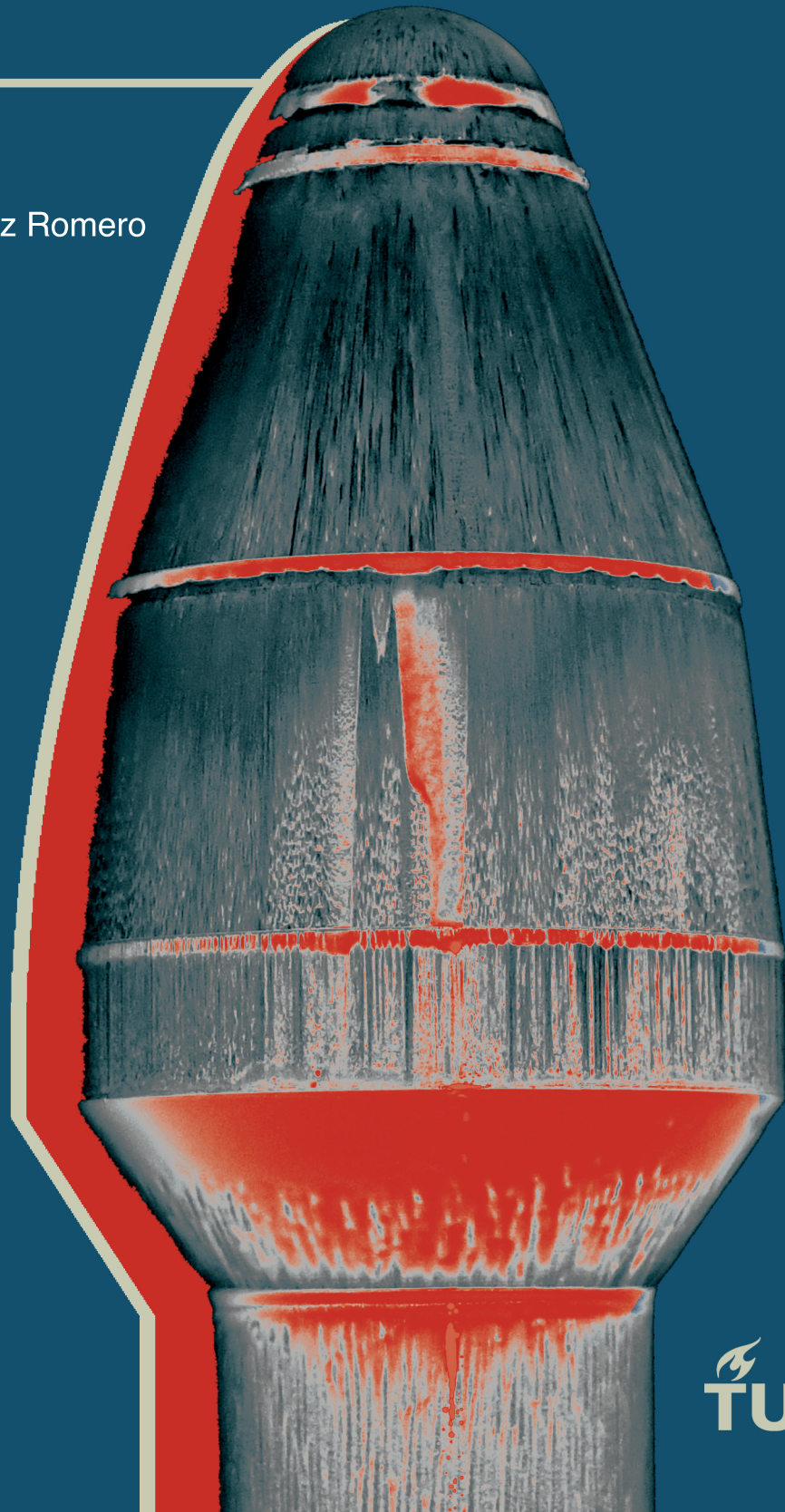


# Experimental Investigation into the Aerodynamics of Hammerhead Launcher Configurations in Transonic Flow Regime

---

MSc Thesis  
Andrea González Romero





# Experimental Investigation into the Aerodynamics of Hammerhead Launcher Configurations in Transonic Regime

by

Andrea González Romero

in partial fulfilment of the requirements for the degree of

**Master of Science**  
in Aerospace Engineering

at the Flow Physics and Technology Department of the  
Aerospace Engineering Faculty of TU Delft

**Student Number:** 5462592  
**MSc. Track:** Aerodynamics  
**Supervisors:** Dr. ir. A. D'Aguanno  
Dr. ir. B.W. van Oudheusden  
Dr. ir. F.F.J. Schrijer  
**Date:** November 10, 2023

Cover image: Miriam González Romero



# Abstract

As the space industry continues to grow rapidly, the development of reusable launch vehicles has become crucial in achieving cost-effective and sustainable access to space. Payload capacity optimisation has been at the forefront of this effort, leading to a renewed interest in hammerhead or bulbous payload fairing (PLF) configurations. These designs feature a larger diameter in the PLF than in the rest of the launch vehicle, enabling the same structure to be used for large payloads. However, the transonic regime poses unique challenges for these PLFs due to their susceptibility to flow separation and strong pressure fluctuations.

This master thesis investigates the influence of nose and boat-tail geometries on flow phenomena, particularly shock wave generation, around hammerhead configurations in transonic conditions. The research was conducted through three distinct experimental campaigns in the transonic wind tunnel TST-27 at the high-speed laboratory of TU Delft, employing schlieren, oil flow, and Particle Image Velocimetry (PIV) techniques.

The study revealed notable insights into the aerodynamics of the hammerhead PLF configurations. Boat-tails set at five and 15-degree angles were observed to broaden the range of shock wave oscillations, introducing an additional shock wave that could occasionally merge with existing ones. Moreover, the conic nose design induced higher shock wave oscillations, while the bi-conic nose introduced an extra shock wave compared to the conic and ogive noses. The study also found that altering the nose shape while keeping the boat-tail constant, or vice versa, resulted in similar effects on flow dynamics.

These findings underscore the critical role that nose and boat-tail geometries play in shaping the aerodynamic behaviour of hammerhead PLF configurations. The results have implications for such configurations' design and stability considerations in transonic conditions. It was observed that raising the Mach number heightened shock wave oscillations and flow detachment. The angle of attack disrupted model symmetry, primarily impacting reattachment patterns. Furthermore, the conic nose exhibited greater unsteadiness due to oscillations in the shock waves compared to the other geometries. The study also provided detailed insights into shock wave spectral characteristics and identified potential influences of pressure wave oscillations on shock wave behaviour. The conclusions lead to recommend designs with bi-conic nose, and avoid boat-tail angles around 15 degrees.

**Keywords:** Hammerhead Configuration, PIV, Schlieren, Oil Flow Visualization, Transonic Flow, Flow Separation, Payload Fairings, Buffeting



# Acknowledgements

*Quem deseja ver o arco-íris,  
precisa aprender a gostar da chuva.*

Paulo Coelho

Before you lies my master's thesis report, needed to fulfil the graduation requirements of the MSc. Aerospace Engineering program at the Delft University of Technology. I was engaged in researching and writing this thesis from January to October 2023.

I am really happy with both the journey and outcome of this rollercoaster ride that was my thesis. Considering how easy is to take for granted what others do for us in this frenetic life, I want to take this section to acknowledge that this would not have been possible alone.

First, my gratitude goes towards my supervisors: Alessandro, Bas and Ferry, for allowing me to perform this research, where I felt free and entrusted to make decisions and mistakes, and most importantly, for the excellent guidance and support. A special appreciation goes to Alessandro, for being so patient in teaching me and helping with all the problems that arose throughout the experimental campaigns, which were not few. *Grazie mille*. I was also really lucky to count with the help of all the technicians at the HSL. Particularly, I want to thank Frits Donker Duyvis, vital in the model design and testing development; Peter Duyndam, who always made time to help me and perform all the runs I needed to do, and Adam Head, for all the assistance setting up the PIV campaign. I would like to also thank Ed Roessen, who manufactured the models; Eddy van den Bos and Daniel Atherstone, for solving my doubts during the model concept drawings, and Barry Zandbergen, for his insights from the launcher design side. Many other TU Delft staff have helped me, and the truth is that I have always felt there was someone available and eager to help me, for what I am really thankful.

On a more special note, my gratitude to all the people around me daily goes beyond what any words can express. You may think you are not doing anything special, but for me, any successes that come will also be yours. Uncertainty about what to do next is easier when surrounded by people who trust and encourage you along the way.

Thanks to my family and friends, who even at distance, are always there. To my parents, to whom I owe everything. To Miriam, the best graphic designer, but most importantly, the best sister anyone could ask for. To Belén, for the flowers and cheerfulness even if we did not know what we were doing anymore. To Laura, lecture partner from Terrassa to the world. To my flatmates, for creating a home where I could return every day. To Mirthe, for being an incredibly supportive boss. To Àlex, Jan, Joel and Jose, for their feedback in anything I need. To Adri, my podcast listener of excellence. To Carla, always ready to switch from professional advisor to attentive friend.

As for those obsessed with embracing me as a compatriot, treating me as one of their own, becoming my reviewers, cheerleaders, and even my punching bag when necessary. Thank you for sharing both the highs and lows, for listening to my complaints, for the laughter, the songs, everything. No words can express how thankful I am for having crossed paths with all of you. *Saudade* will be (and already is) intense after all I have lived with you. Bernardo, *o melhor professor de todos (e o mais persistente), apaixonado pela vida. Pessoas como tu tornam este mundo melhor*; you illuminate wherever you go. Diogo, *extraordinária bondade e inteligência*; I hope you fight for what you deserve, which is a lot. Miguel, *confio que o mundo te*

*descubra, a música em pessoa; stay true to your humor and values. Pedro, the coach to work, train, and simply give my best. You are a professional in aerodynamics now. Obrigada pelo teu apoio incondicional (com a verdade sempre na frente). Embora difícil, a minha admiração e apreciação por ti não param de crescer. Nunca deixes a tua chama apagar-se, nada nem ninguém merece, haters will always hate.*

*Gràcies, gracias, obrigada.*

Finally, to the reader, I hope this thesis provides valuable insights and contributes to the engineering field. Thank you for taking the time to read it.

*Andrea González Romero  
Manresa, October 2023*

# Contents

<b>Abstract</b>	<b>iii</b>
<b>Acknowledgements</b>	<b>v</b>
<b>List of Figures</b>	<b>xiv</b>
<b>List of Tables</b>	<b>xv</b>
<b>Nomenclature</b>	<b>xvii</b>
<b>1 Introduction</b>	<b>1</b>
<b>2 Literature Review</b>	<b>5</b>
2.1 Flow Phenomena around Hammerhead PLFs . . . . .	5
2.1.1 Transonic Flow . . . . .	5
2.1.2 Flow Separation . . . . .	7
2.1.3 Unsteady Loads . . . . .	10
2.1.4 Wake Reattachment . . . . .	13
2.2 Payload Fairings Design . . . . .	14
2.2.1 Nose Shapes . . . . .	15
2.2.2 Boat-Tail Region . . . . .	17
2.2.3 Common Hammerhead Payload Fairing Geometries . . . . .	18
2.3 Flow Measurement Techniques Used in PLFs Aerodynamic Research . . . . .	25
2.4 Discussion . . . . .	28
2.5 Research Questions . . . . .	28
<b>3 Experimental Methodology</b>	<b>31</b>
3.1 Test Facility . . . . .	31
3.2 Test Models . . . . .	33
3.3 Flow Conditions . . . . .	36
3.4 Experimental Campaigns . . . . .	39
3.4.1 Oil Flow Visualisation . . . . .	39
3.4.2 Schlieren Visualisation . . . . .	41
3.4.3 Particle Image Velocimetry . . . . .	45
3.5 Uncertainty Analysis . . . . .	52
3.6 Data Analysis . . . . .	54
3.6.1 Schlieren Images Processing . . . . .	54
3.6.2 PIV Data Processing . . . . .	55
<b>4 Results</b>	<b>59</b>
4.1 General Flow Field . . . . .	59
4.2 Geometrical Effects . . . . .	66
4.2.1 Nose . . . . .	66
4.2.2 Boat-Tail . . . . .	69
4.2.3 Nose and Boat-Tail Effects Dependence . . . . .	73
4.3 Mach Number Effect . . . . .	74

---

4.4	Angle of Attack Effect . . . . .	77
4.5	Shock Wave Spectral Analysis . . . . .	80
4.6	Wake Reattachment Location . . . . .	84
<b>5</b>	<b>Conclusions and Future Work</b>	<b>91</b>
5.1	Design Recommendations . . . . .	93
5.2	Future Work . . . . .	93
	<b>References</b>	<b>95</b>
<b>A</b>	<b>Model Drawings</b>	<b>101</b>
<b>B</b>	<b>Test Matrices</b>	<b>111</b>
<b>C</b>	<b>Oil Flow Visualisation Images and Diagrams Comparison</b>	<b>113</b>

# List of Figures

1.1	Falcon 9 launcher. Credit: Space Exploration Technologies photo. . . . .	1
1.2	VEGA-C rocket illustration. Credit: Arianespace/UPI. . . . .	1
1.3	Schematic representation of a hammerhead shaped fairing. [3] . . . . .	2
2.1	Subsonic flow patterns around hammerhead payload fairing. [4] . . . . .	5
2.2	Transonic flow patterns around hammerhead payload fairing. [4] . . . . .	6
2.3	Schematic sketch of flow field over payload shroud at transonic speed. [6] . . . . .	7
2.4	Separated flow due to geometric change at boat-tail region. [4] . . . . .	8
2.5	Backward-Facing Step (BFS) flow topology. [8] . . . . .	9
2.6	Transonic flowfield around hammerhead PLF. [12] . . . . .	10
2.7	Causes of unsteady loads: (a) Movement of shock wave during transonic regime; (b) Shock Wave-Boundary Layer Interaction (SWBLI) which induces flow separation; (c) Pressure oscillation due to wake, and (d) Flow separation due to geometric shape and reattachment. [4] . . . . .	10
2.8	Geometrical parameters of the forebody representing a hammerhead PLF configuration. [4] . . . . .	12
2.9	Pressure distribution on NASA's hammerhead geometry Model 11 at an angle of attack of 4 deg for subsonic and transonic speeds. [32] . . . . .	14
2.10	Schematic representation of a hammerhead-shaped fairing with the boat-tail region indicated. Based on [4]. . . . .	15
2.11	Generic PLFs nose shapes. Based on [4]. . . . .	15
2.12	Sears-Haack minimum drag for given length and diameter series type nose shape (also known as Von Kármán). Source: Wikipedia . . . . .	16
2.13	Shadowgraphy of the flow over a (a) Cone-Cylinder Body and the (b) Saturn IB SA-203 vehicle at Mach 0.89 and 0.9, respectively. [35] . . . . .	17
2.14	Model profiles tested by Coe [16] to evaluate the impact of nose shape at transonic speeds. . . . .	17
2.15	Schematic of observed boat-tail flows. [13] . . . . .	18
2.16	Hammerhead launch vehicles models tested by Coe and Nute [16]. . . . .	19
2.17	Dimensions of the NASA-developed Hammerhead Launch Vehicle Model 11, originally tested by Coe and Nute [16], in inches. [39] . . . . .	20
2.18	Shadowgraphy images of the upper half of the model at an angle of attack of 4 degrees and the indicated Mach numbers: (a) $Ma = 0.6$ ; (b) $Ma = 0.8$ ; (c) $Ma = 0.85$ ; (d) $Ma = 0.92$ ; (e) $Ma = 1.05$ ; (f) $Ma = 1.2$ . [39] . . . . .	20
2.19	Composite of shadowgraph image, rms (root mean square) of light intensity fluctuations calculated from the high-speed shadowgraph images, and distribution of $C_{prms}$ measured by dynamic pressure sensors at an angle of attack of 4 degrees and the indicated three Mach numbers. (a) $Ma = 0.6$ ; (b) $Ma = 0.8$ ; (c) $Ma = 1.1$ . [39] . . . . .	21
2.20	Payload fairing options for the Atlas V launcher. Source: ULA Launch . . . . .	22
2.21	Payload fairing options for the Delta II launcher. Source: Wikipedia . . . . .	23
2.22	Titan IVB launcher. Source: National Museum . . . . .	23
2.23	Delta II launcher. Source: ULA Launch . . . . .	23

2.24 Falcon 9 and Falcon Heavy launchers. [2] . . . . .	24
2.25 VLS-1, Vega C and Soyuz-2 launchers. . . . .	24
2.26 GSLV-MK-III, H-IIB and CZ-6 launchers. . . . .	25
2.27 Oil flow visualisation (a) and CFD skin friction lines (b) at Mach 1.8 and angle of attack, $\alpha$ , of $10^\circ$ . [45] . . . . .	26
2.28 Oil flow visualisation photographs for a diameter ratio $d/D = 0.65$ , a Mach velocity $M = 0.8$ , and two different boat-tail angles $\beta$ : 90 and 31.5 degrees. The boundary-layer separation is indicated by an S, and the reattachment by an R. [13] . . . . .	26
2.29 Schlieren image together with PSP (Pressure Sensitive Paint) results for $Ma = 1.0$ and boat-tail angle of $90^\circ$ . [3] . . . . .	27
2.30 Mean horizontal field on the base of the Ariane 5's configuration 5000 main launcher for $Ma = 0.5$ . [19] . . . . .	27
3.1 TST-27 wind tunnel (air flow from right to left) with the Schlieren set-up at z-configuration mounted (table on the right, the last mirrors and lenses together with the camera can be seen from setup described in Figure 3.15). . . . .	31
3.2 TST-27 test section with Coe and Nute's Model 11 base geometry configuration, also referred as benchmark configuration along the report. On the background, one of the mirrors used for the z-configuration Schlieren set-up is seen. . . . .	32
3.3 Technical drawing of TST-27 with indication of supersonic throat ( $A_{t1}$ ), test section ( $A_{test}$ ) and transonic throat ( $A_{t2}$ ). [50] . . . . .	33
3.4 Transonic throat visualization (left) and schematic (right). [50] . . . . .	33
3.5 Schematic representation of the upper part of Model 11 used by Coe and Nute [34], showcasing the diameters of the PLF, $D$ , and the rest of the vehicle, $d$ . . . . .	34
3.6 Schematic representation of the wind-tunnel model including the most representative dimensions in mm. In blue is shadowed the section numbered as 02 for the manufacturing, and in orange is coloured section 04 (being 01 the nose, and 03 the boat-tail area removable part). . . . .	34
3.7 Representation of the three nose geometries modelled to be manufactured and tested along the project: a) Sears-Haack, b) Conic and c) Bi-conic. All the shapes have been spherically blunted for an improved aerodynamic performance. . . . .	35
3.8 Drawings with dimensions (in mm) of the three nose geometries modelled to be manufactured and tested along the project: a) Sears-Haack, b) Conic and c) Bi-conic. All the shapes have been spherically blunted for an improved aerodynamic performance. . . . .	35
3.9 Drawings with dimensions (in mm) of the three boat-tail angle geometries modelled to be manufactured and tested along the project: a) 5 degrees, b) 15 degrees and c) 34 degrees. . . . .	35
3.10 Infrared image depicting boundary layer transition wedges in the Model 11 benchmark model. [57] . . . . .	36
3.11 Detail photo of the transition strip located at 20% nose length from the model's leading edge. . . . .	36
3.12 Oil flow patterns for the benchmark model configuration at Mach number of 0.7 and zero degree angle of attack with and without transition strip. . . . .	37
3.13 Air-oil layer interface representation together with the velocity gradient present in the oil. . . . .	40
3.14 TST-27 wind tunnel with the tripod and external light system used to record the oil flow runs. . . . .	41
3.15 Schlieren visualization arrangement in z-type configuration. [61] . . . . .	42

3.16	Schematic showing the refraction of light rays by density fields with density and its first, second, and third derivatives constant. The two-dimensional description is easily extended to three dimensions. [62] . . . . .	44
3.17	Experimental arrangement for planar 2C-2D PIV in a wind tunnel. [63] . . . . .	45
3.18	Diagram of the PIV set-up, with top (left) and lateral (right) views. The field of views (FOV) numbers refer to the areas designated in Figure 3.23. . . . .	46
3.19	PIV set-up featuring the benchmark Coe and Nute model positioned at 4 degrees. In the background, two cameras are positioned at different heights to ensure full coverage of the field of view. . . . .	47
3.20	Illuminated test section as seen from one of the optical access windows. . . . .	48
3.21	Illumination and imaging system. . . . .	48
3.22	Laser probe 3D CAD with cut-outs to facilitate overall system view. [64] . . . . .	49
3.23	Fields of view (FOV) for the three cameras used at PIV. . . . .	50
3.24	Average modular velocity field $ U $ with streamlines. Data extracted through PIV for benchmark case (Coe and Nute's model 11 [34] composed by bi-conic nose and 34-degree boat-tail) at Mach 0.7 and angle of attack of 0 degrees (run 1 at Table B.3). . . . .	50
3.25	PIV timing diagram for double-pulse double-frame mode. [65] . . . . .	51
3.26	Consecutive PIV raw images with details on a window of interrogation of 128x128 pixels. . . . .	56
3.27	Horizontal velocity field $U_x$ obtained from performing a cross-correlation procedure of the PIV raw image pair of Figure 3.26 with a multi-pass approach (two passes with squared window size of 128x128 pixels, and three passes with circular interrogation window of 48x48 pixels). . . . .	56
4.1	Schlieren image for benchmark configuration (BC34) at Mach number 0.8 and angle of attack of 4 degrees (run 20 at Table B.2) with flow patterns marked. Red rectangle shows region zoomed in the time sequence of Figure 4.2. . . . .	60
4.2	Time sequence with three Schlieren instantaneous shots, each taken with a time interval of $\Delta t = 0.6$ ms between them. Focus made on the conic transitions of the BC nose (area enclosed in red in Figure 4.1). BC34 at Mach number 0.8 and angle of attack of 4 degrees (run 20 at Table B.2). . . . .	60
4.3	Average horizontal and vertical velocity fields, $U_x$ and $U_y$ , around benchmark configuration at $Ma = 0.8$ and $AoA = 4$ degrees derived from PIV (run 11 at Table B.3). . . . .	61
4.4	Boat-tail area zoom of the average horizontal velocity field $U_x$ for $Ma = 0.8$ and $AoA = 4$ degrees (run 11 at Table B.3). . . . .	62
4.5	Standard deviation field of the horizontal velocity $U_x$ around benchmark configuration at $Ma = 0.8$ and $AoA = 4$ degrees derived from PIV (run 11 at Table B.3). . . . .	62
4.6	Number of times each velocity vector had reverse flow, $n_{rev}$ , over the total 479 PIV images considered, $N$ , for BC34 at $Ma = 0.8$ and $AoA = 4$ degrees (run 11 at Table B.3). . . . .	63
4.7	Schematic and photography of oil flow patterns for BC34 at $Ma = 0.8$ and $AoA = 4$ degrees (run 28 Table B.1). Detail zoom showcases oil flow direction in reattachment area (as seen in recording). . . . .	64
4.8	Comparison between instantaneous (a) shadowgraphy picture from Panda [39] (see Figure 2.18) and (b) schlieren image (run 18 at Table B.2) for $Ma = 0.6$ and $AoA = 4^\circ$ . . . . .	64
4.9	Instantaneous schlieren image (run 19 at Table B.2) for $Ma = 0.7$ and $AoA = 4^\circ$ . . . . .	65

4.10 Comparison of benchmark configuration at AoA = 4 degrees: (a) Instantaneous shadowgraphy from Panda [39] at Ma = 0.8 (see Figure 2.18), (b) Instantaneous shadowgraphy from Panda [39] at Ma = 0.85 (see Figure 2.18), and (c) Schlieren image (Run 20 at Table B.2) at Ma = 0.8. . . . .	65
4.11 Schlieren instantaneous images for Ma = 0.8, AoA = 0 degrees, boat-tail of 34 degrees and bi-conic, conic and ogive noses. . . . .	66
4.12 Comparison between schlieren instantaneous images showing the most downstream and upstream shock wave locations for Ma = 0.8, AoA = 0 degrees and geometries (a) BC34, (b) C34 and (c) SH34 (runs 5, 11 and 13 at Table B.2, respectively). Zoom into red region of Figure 4.11. . . . .	67
4.13 Comparison between pixel intensity standard deviation of the schlieren images for Ma = 0.8, AoA = 0 degrees and geometries (a) BC34, (b) C34 and (c) SH34 (runs 5, 11 and 13 at Table B.2, respectively). . . . .	67
4.14 Schematic representation of the oil flow patterns (see a comparison with photographs in Appendix C) obtained at Ma = 0.8, AoA = 0 degrees (runs 30, 31 and 32 at Table B.1). . . . .	69
4.15 Schlieren instantaneous images for Ma = 0.8, AoA = 0 degrees, bi-conic nose and boat-tail angles of 5, 15 and 34 degrees. . . . .	70
4.16 Comparison between pixel intensity standard deviation of the schlieren images for Ma = 0.8, AoA = 0 degrees, bi-conic nose and boat-tail angles of (a) 5, (b) 15 and (c) 34 degrees (runs 7, 9 and 5 at Table B.2, respectively). . . . .	71
4.17 Time sequence with schlieren instantaneous images, each taken with a time interval of $\Delta t = 0.2 \text{ ms}$ between them for BC5. Focus made on the nose and boat-tail regions at Ma = 0.8 and AoA = 0 degrees (run 7 at Table B.2). . . . .	71
4.18 Time sequence with schlieren instantaneous images, each taken with a time interval of $\Delta t = 0.2 \text{ ms}$ between them. Focus made on the bi-conic nose and 15-degree boat-tail regions at Ma = 0.8 and AoA = 0 degrees (run 9 at Table B.2). . . . .	72
4.19 Pixel intensity standard deviation of schlieren images for Ma = 0.8, AoA = 0 degrees and geometries (a) BC34, (b) BC5, (c) SH34, and (d) SH5 (runs 5, 7, 13 and 15 at Table B.2). . . . .	73
4.20 Time sequence with schlieren instantaneous images, each taken with a time interval of $\Delta t = 0.2 \text{ ms}$ between them. Focus made on the ogive nose and 5-degree boat-tail regions at Ma = 0.8 and AoA = 0 degrees (run 15 at Table B.2). . . . .	73
4.21 Instantaneous schlieren picture and pixel intensity standard deviation from schlieren images for the benchmark case (Coe and Nute's model 11 [34]) at AoA = 0 degrees for Mach numbers of 0.7 and 0.8. . . . .	75
4.22 Horizontal velocity $U_x$ average field for PIV runs with the benchmark configuration (BC34) at 0-degree angle of attack. Top plot corresponds to Mach 0.7, and bottom plot to 0.8 (PIV runs 1+2 and 3+4 in Table B.3). . . . .	76
4.23 Horizontal velocity standard deviation $\sigma_{U_x}$ field from PIV runs with the benchmark configuration (BC34) at 0-degree angle of attack. Top plot corresponds to Mach 0.7, and bottom plot to 0.8 (PIV runs 1+2 and 3+4 in Table B.3). . . . .	76
4.24 Zoom into oil flow visualisation reattachment regions for benchmark case (Coe and Nute's model 11 [34]) at Ma = 0.8 and angles of attack of 0 and 4 degrees. . . . .	77
4.25 Horizontal velocity $U_x$ average field for PIV runs with the benchmark configuration (BC34) at Mach 0.8. Top plot corresponds to 0-degree angle of attack, and bottom plot to 4-degree AoA (PIV runs 3+4 and 11+12 in Table B.3). . . . .	78

4.26	Instantaneous schlieren picture and pixel intensity standard deviation from schlieren images for the benchmark case (Coe and Nute's model 11 [34]) at AoA = 0 and 4 degrees for Mach number of 0.8. . . . .	79
4.27	Zoom in to Schlieren instantaneous image for benchmark configuration (Coe and Nute's model 11 [34] with bi-conic nose and 34-degree boat-tail) at 0-degree angle of attack and Mach 0.8 highlighting in red the pixel line represented along time in Figure 4.28, and in yellow the regions considered for the PSD curves (see Figure 4.29). . . . .	80
4.28	Selected pixel line (red line in Figure 4.27) along 500 timesteps for Schlieren run of the benchmark case (Coe and Nute's model 11 [34]) at Ma = 0.8 and AoA = 0 degrees (run 5 at Table B.2). In blue, highlighted the region where the shock waves location variation is observed. . . . .	81
4.29	Power spectral density multiplied by frequency over frequency for selected pixels (see Figure 4.27 points in blue) along time from Schlieren test of the benchmark case (Coe and Nute's model 11 [34]) at Ma = 0.8 and AoA = 0 degrees (run 5 at Table B.2). . . . .	82
4.30	Reattachment location $L$ and its width $w$ determined from oil-flow image by using the PLF's diameter $D = 50 \text{ mm}$ . . . . .	84
4.31	Bi-colour plot for PIV run 1 (refer to Table B.3) differentiating between positive (light blue) and negative (black) average horizontal velocity $U_x$ . . . . .	84
4.32	Instantaneous horizontal velocity $U_x$ fields for PIV run 1 (refer to Table B.3) corresponding to bi-conic nose, 34-degree boat-tail, 0-degree angle of attack and Mach 0.7. . . . .	85
4.33	Average horizontal velocity $U_x$ fields together with streamlines around boat-tail area for cases with bi-conic nose, 15-degree boat-tail and 0-degree angle of attack. . . . .	86
4.34	Standard deviation of the horizontal velocity $\sigma_{U_x}$ fields around boat-tail area for cases with bi-conic nose, 15-degree boat-tail and 0-degree angle of attack. . . . .	86
4.35	Instantaneous horizontal-velocity $U_x$ together with vector fields for PIV run 5 (refer to Table B.3) corresponding to bi-conic nose, 15-degree boat-tail, 0-degree angle of attack and Mach 0.7. . . . .	87
4.36	Number of times each velocity vector had reverse flow over the total number of images for PIV cases tested at Mach 0.7 and boat-tail of 15 degrees (runs 5 and 13 at Table B.3). . . . .	88
C.1	Comparison between real photography and schematic representation of the oil flow patterns obtained for run 27 at Table B.1: benchmark case based on Coe and Nute's model 11 [34] with bi-conic nose, boat-tail of 34-degrees, Ma = 0.7 and AoA = 4 degrees. . . . .	113
C.2	Comparison between real photography and schematic representation of the oil flow patterns obtained for run 28 at Table B.1: benchmark case based on Coe and Nute's model 11 [34] with bi-conic nose, boat-tail of 34-degrees, Ma = 0.8 and AoA = 4 degrees. . . . .	114
C.3	Comparison between real photography and schematic representation of the oil flow patterns obtained for run 29 at Table B.1: benchmark case based on Coe and Nute's model 11 [34] with bi-conic nose, boat-tail of 34-degrees, Ma = 0.7 and AoA = 0 degrees. . . . .	114

---

C.4	Comparison between real photography and schematic representation of the oil flow patterns obtained for run 30 at Table B.1: benchmark case based on Coe and Nute's model 11 [34] with bi-conic nose, boat-tail of 34-degrees, $Ma = 0.8$ and $AoA = 0$ degrees. . . . .	115
C.5	Comparison between real photography and schematic representation of the oil flow patterns obtained for run 31 at Table B.1: ogive (based on Sears-Haack curve) nose, boat-tail of 34-degrees, $Ma = 0.8$ and $AoA = 0$ degrees. . . . .	115
C.6	Comparison between real photography and schematic representation of the oil flow patterns obtained for run 32 at Table B.1: conic nose, boat-tail of 34-degrees, $Ma = 0.8$ and $AoA = 0$ degrees. . . . .	116
C.7	Comparison between real photography and schematic representation of the oil flow patterns obtained for run 34 at Table B.1: benchmark case based on Coe and Nute's model 11 [34] with bi-conic nose, boat-tail of 34-degrees, $Ma = 0.7$ and $AoA = 0$ degrees. . . . .	116

# List of Tables

2.1	General guidelines for the buffet free configuration as per the geometry of Figure 2.8. [14]	12
3.1	Flow conditions for $Ma_\infty = 0.7$ , total temperature of 288 K, and total pressure of 2 bar.	38
3.2	Flow conditions for $Ma_\infty = 0.8$ , total temperature of 288 K, and total pressure of 2 bar.	38
3.3	Oil flow test matrix.	40
3.4	Schlieren campaign measurement parameters and tested configurations	45
3.5	PIV campaign parameters and tested configurations	47
3.6	Uncertainty values.	54
3.7	PIV post-processing settings	56
4.1	Nose shape abbreviations.	59
4.2	Shock wave average position for all tested configurations in the schlieren campaign. Numbers indicate the first two shock waves, with (1) representing the most upstream and (2) the subsequent shock wave. A hyphen (-) signifies the absence of an extracted value, indicating the non-discernibility or non-existence of a second shock wave.	81
4.3	PSD peak frequencies on main shock wave positions for all tested configurations during Schlieren campaign. Numbers indicate the first two shock waves, with (1) representing the most upstream and (2) the subsequent shock wave. Hyphen (-) denotes the absence of an extracted value due to the non-discernibility or non-existence of a second shock wave.	83
4.4	Parameters characterising the reattachment region (distance $L$ and width $w$ ) obtained from both oil flow (OF) and PIV runs, denoted as $R_{OF}$ and $R_{PIV}$ respectively (same numbering as in Tables B.1 and B.3). Nose configurations are identified by BC (bi-conic), C (conic), and SH (Sears-Haack or ogive). PIV runs with the same configuration are combined for statistical reliability. Hyphen - indicates no extracted value, signifying either the absence of the run or no reattachment.	89
B.1	Oil flow visualisation campaign full test matrix.	111
B.2	Schlieren visualisation campaign full test matrix.	112
B.3	PIV campaign full test matrix. $N$ refers to the number of images taken per run.	112



# Nomenclature

## Abbreviations

<b>Abbreviation</b>	<b>Definition</b>
BC	Bi-conic
BFS	Backward Facing Step
BOS	Background Oriented Schlieren
BT	Boat-Tail
C	Conic
CFD	Computational Fluid Dynamics
TU Delft	Delft University of Technology
DEHS	Di-Ethyl-Hexyl-Sebacat
DFT	Discrete Fourier Transform
DNS	Direct Numerical Simulation
FMT	Flow Measurement Technique
FOV	Field Of View
HHF	Hammerhead Fairing
HSL	High-Speed Laboratory
HWA	Hot Wire Anemometry
LE	Leading Edge
LES	Large-Eddy Simulation
LV	Launch Vehicle
NLR	Netherlands Aerospace Centre
OF	Oil Flow visualisation
PIV	Particle Image Velocimetry
PLF	Payload Fairing
PSD	Power Spectral Density
PSP	Pressure Sensitive Paint
PTU	Programmable Time Unit
RANS	Reynolds Averaged Navier Stokes
SBLI	Shock Boundary Layer Interaction
SH	Sears-Haack
SOA	State of the Art
SW	Shock Wave
TBL	Turbulent Boundary Layer
TUPLE	Transonic PIV based Unsteady Pressure measurements for Launcher Environment
ULA	United Launch Alliance
WS	Window Size

## Symbols

Symbol	Definition	Unit
$A_m$	Projection surface of the model	[mm <sup>2</sup> ]
$A_{t1}$	Surface of continuously variable throat	[mm <sup>2</sup> ]
$A_{t2}$	Surface of variable choke mechanism	[mm <sup>2</sup> ]
$A_{test}$	Cross-sectional area of the test section	[mm <sup>2</sup> ]
$a$	Beam radius	[m]
$\vec{a}_p$	Particle acceleration	[m/s <sup>2</sup> ]
$B_r$	Blockage ratio	[-]
$c$	Velocity of light in vacuum	[m/s]
$c_v$	Velocity of light in the medium	[m/s]
$D$	Lens aperture diameter or PLF's main diameter	[mm]
$d$	Launcher's cylindrical diameter	[mm]
$d_i$	Distance between image and lens	[mm]
$d_o$	Distance between object and lens	[mm]
$d_p$	Particle image diameter	[m]
$d_\tau$	Acceptable approximation of the resulting particle image diameter	[m]
$f$	Frequency or Focal length	[Hz] or [m]
$f\#$	Relation between lens focal length and aperture	[-]
$H$	TST-27 rods height	[mm]
$L$	Length	[m]
$L_{RL}$	Distance between model's leading edge and reattachment location	[mm]
$M$	Magnification factor	[-]
$Ma$	Mach number	[-]
$N$	Number of samples	[-]
$N_{pixels}$	Number of pixels	[-]
$n$	Refractive index	[-]
$n_{rev}$	Number of times a pixel had reverse flow	[-]
$P$	Power spectral density	[s]
$R$	Radius or Specific gas constant	[m] or [ $\frac{J}{kg \cdot K}$ ]
$Re$	Reynolds number	[-]
$SR$	Sample rate	[Hz]
$t_{SW}$	Projected shock wave thickness	[mm]
$U$	Velocity	[m/s]
$w_{FOV}$	Width of the Field of View	[m]
$w_{RL}$	Width of the reattachment location	[mm]
$z_A$	Distance lens-Schlieren object	[mm]
$z_B$	Distance lens-background plane	[mm]
$z_D$	Distance object-background	[mm]
$z_i$	Distance lens-image plane	[mm]
$\Delta t$	Pulse time separation	[ $\mu$ s]
$\Delta y$	Image displacement in y direction	[m]
$\Delta z_0$	Light sheet thickness	[m]
$\delta z$	Focal depth of the optical system	[m]
$\epsilon_y$	Light deflection in y direction	[deg]

<b>Symbol</b>	<b>Definition</b>	<b>Unit</b>
$\varepsilon_\sigma$	Uncertainty in the standard deviation, $\sigma$	[-]
$\varepsilon_U$	Uncertainty in the mean velocity, $U$	[-]
$\lambda$	Wavelength	[m]
$\mu$	Dynamic viscosity	$[\frac{kg}{m \cdot s^{-1}}]$
$\rho$	Density	$[kg/m^3]$
$\sigma$	Standard deviation	[-]
$\tau_p$	Particle response time	$[\mu s]$



# 1

## Introduction

*Research is creating new knowledge.*

Neil Armstrong

The space industry has grown rapidly in recent years, driving the need for cost-effective and sustainable access to space. Reusable launch vehicles have emerged as a key solution to this need, with payload capacity optimisation being a primary focus. Hammerhead or bulbous payload fairing (PLF) configurations have gained renewed interest due to their larger diameter in the PLF than in the rest of the launch vehicle (LV), enabling the reuse of the same LV for large payloads. Industry leaders such as the European Space Agency's Vega-C launcher and SpaceX's Falcon launchers have adopted these designs (see Figures 1.1 and 1.2), demonstrating their relevance and effectiveness [1, 2].



**Figure 1.1:** Falcon 9 launcher. Credit: Space Exploration Technologies photo.



**Figure 1.2:** VEGA-C rocket illustration. Credit: Arianespace/UPI.

The main parts of a Hammerhead Fairing (HHF), as shown in Figure 1.3, are:

- **Nose:** curved, pointed end attached to the front of the launch vehicle. The nose is designed to smoothly transition the airflow from the freestream to the HHF, reducing drag and turbulence. This shape is typically conical or ogive.
- **Payload:** primary cargo or equipment being carried by the launch vehicle. The payload is housed within the HHF and is protected from the harsh aerodynamic forces and environmental conditions experienced during flight. Hammerhead PLFs are distinguishable due to having a larger diameter than the rest of the vehicle, which allows for the accommodation of bigger payloads than other fairing designs.
- **Boat-tail Region:** part of the HHF attached to the launch vehicle's top. Payload fairings without a boat-tail region, known as straight Payload Fairings (PLFs), are preferred from an unsteady loads perspective.

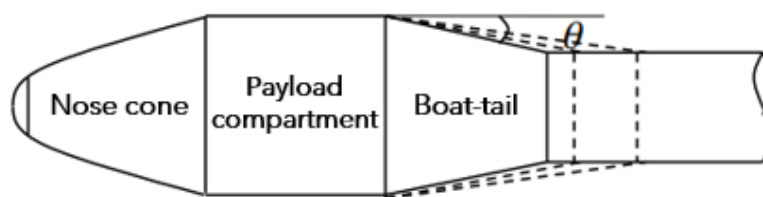


**Figure 1.3:** Schematic representation of a hammerhead shaped fairing. [3]

The design of these parts is crucial to ensure the best performance, and its shapes and dimensions are often optimised to minimise unsteady loads through computational simulations and wind tunnel testing. Such optimisation is much more interesting for launcher design than other more common aerodynamic optimisations as drag minimisation. Launchers are meticulously crafted to meet both structural and mechanical prerequisites. For instance, the shape of the PLF is commonly dictated by the desired opening mechanism for loading purposes. Additionally, the dimensions of the launcher stem from comprehensive structural analyses. When these factors are taken into account, the significance of variations in drag becomes relatively diminished. Any heightened drag can be effectively counterbalanced by augmenting the fuel load within the launcher—a preferable approach. Conversely, mitigating unpredictable loads that could potentially jeopardise the launcher's structural integrity holds paramount importance, as these cannot be offset through alternative means. Along the different regimes that PLFs face during flight, the transonic regime prones unsteadiness the most and can lead to flow separation due to the hammerhead geometry, exposing the vehicle to strong pressure fluctuations which can compromise the structure [3]. Therefore, the relevance of studying the flow phenomena around hammerhead configurations in transonic conditions is justified.

### Research Outline

After the current introduction, the report starts with chapter 2 where an overview of the literature study is given, focused on the flow phenomena around hammerhead configurations, the payload fairing design, and the flow measurement techniques commonly used in PLFs aerodynamic research. This summary outlines the research gaps identified during the literature review, which subsequently guided the formulation of the research questions.

Next, chapter 3 offers a detailed description of the experimental setup. This encompasses detailed information about the models used, the techniques employed for flow measurements, an in-depth explanation of the experimental campaigns, an analysis of uncertainties, and the data processing methodology.

Chapter 4 presents the results of the experimental campaigns. The discussion begins with an overview of the general flow characteristics observed in hammerhead PLF geometries. Subsequently, the focus shifts to exploring the effects of changing the geometry (nose and boat-tail), Mach number, and Angle Of Attack (AoA). Furthermore, the chapter delves into the shock wave spectral analysis results and the reattachment locations of shock waves, offering insightful commentaries.

A concise summary of the study's derived conclusions is provided in chapter 5. Additionally, this chapter suggests directions for future research.

Supplementary data, complementing the information presented in this report, is consolidated in the appendices. These include model drawings (refer to Appendix A) and test matrices from the experimental campaigns (consult Appendix B).



# 2

## Literature Review

This chapter presents the literature review done prior to the current research on the aerodynamics of hammerhead PLFs. First, it presents the flow phenomena that characterise hammerhead configurations in the transonic regime. Following this, it delves into payload fairing design, focusing on the prevailing nose and boat-tail region geometries and their influence on the flow dynamics, which justifies the need for research. Additionally, the flow measurement techniques commonly employed in the field are discussed.

The literature review identified gaps in the existing body of knowledge, and based on these gaps, the chapter concludes by outlining the research questions that will be addressed experimentally in the current research project. This chapter provides the foundation for the subsequent chapters of the thesis.

### 2.1. Flow Phenomena around Hammerhead PLFs

Hammerhead-type fairing structures have become increasingly popular in modern launch vehicles as by having a larger diameter than the rest of the structure, the PLF meets the demands to transport bigger payloads. However, this configuration presents significant aerodynamic challenges in the transonic regime. Flow separation can expose critical areas of the vehicle to the external intense acoustic pressure fields and strong pressure fluctuations characteristic of this flight phase. As a result, understanding the complex flow phenomena around hammerhead PLFs in transonic conditions is essential for developing more efficient and reliable launch vehicles [3].

#### 2.1.1. Transonic Flow

Smooth streamlines without discontinuity characterise subsonic flow, as seen in Figure 2.1. Those conditions happen when the flow speed over the vehicle surface always remains below the local speed of sound.

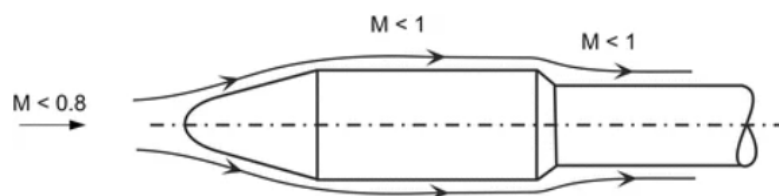


**Figure 2.1:** Subsonic flow patterns around hammerhead payload fairing. [4]

Transonic flow occurs when the flow field around an object is characterised by mixed subsonic and supersonic local flow, typically at flight speeds between Mach 0.8 and 1.2 [5]. The critical Mach number, defined as the free-stream Mach number at which local flow reaches sonic speed, determines the range of velocities where transonic flow exists.

According to Suresh et al. [4], the critical Mach number is usually around 0.8. When such conditions are reached, the subsonic flow locally increases in speed to the sonic speed (Mach number,  $Ma$ , equal to 1) as shown in Figure 2.2a, marking the beginning of the transonic flow regime. As the free stream Mach number increases further, still less than sonic speed, the flow expands locally to a supersonic pocket terminated by a shock, beyond which the flow speed is subsonic (see Figure 2.2b). Due to the instabilities characteristic of these flow conditions, the induced shock wave oscillates. This favours interaction with the boundary layer and can cause the flow to separate. With a further increase in free stream Mach number, a supersonic pocket forms after the cone-cylinder junction, a region of strong expansion. For Mach numbers slightly above unity, a bow shock wave (also called a detached shock or bowed normal shock) is formed in front of the body (see Figure 2.2c) due to the bluntness of the vehicle [5]. At a free stream Mach number of approximately 1.2, already supersonic regime, clear expansion fans are present at the transition between the nose and the cylinder, and an oblique shock appears in front of the vehicle.

Depending on the boat-tail angle, even on transonic conditions, the flow may sometimes separate and reattach, as shown in Figure 2.2d. Moreover, there is recirculation in the boat-tail area [4], as depicted in Figure 2.3.

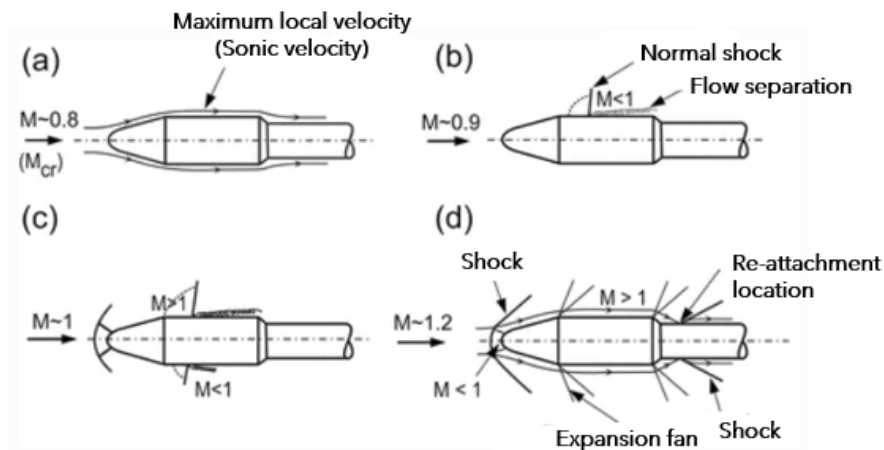


**Figure 2.2:** Transonic flow patterns around hammerhead payload fairing. [4]

Figure 2.3 provides an additional schematic which shows all the flow patterns which can be observed around hammerhead configurations in the transonic regime. This diagram provides a comprehensive overview, encompassing the expansion fan at geometric transitions (as the cone-cylinder junction), the supersonic pocket ended by an oscillating shock that interacts with the boundary layer, shear layer separation due the boat-tail, and the resulting recirculation region and flow reattachment.

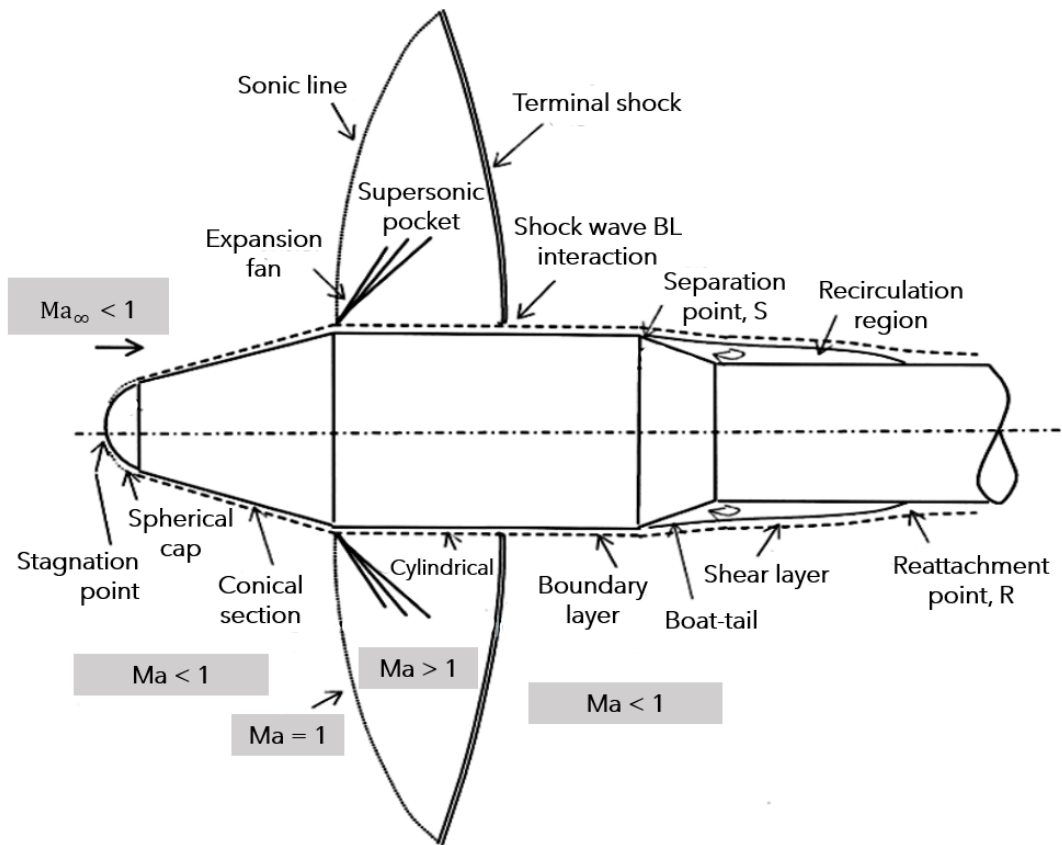


**Figure 2.3:** Schematic sketch of flow field over payload shroud at transonic speed. [6]

### 2.1.2. Flow Separation

Flow separation on a surface occurs when there is an adverse pressure gradient, meaning the pressure along the flow direction increases. Such growth causes the fluid particles in the region near the body's surface to slow down, losing kinetic energy due to viscous dissipation. If the pressure gradient is strong enough, the speed near the surface falls to zero and reverses direction. This creates large eddies and a region of slowly moving, eddying flow known as separated flow.

These flows are unsteady, and as a result, they impart large unsteady loads on the vehicle. Flow separation has three main causes: changes in the vehicle's geometry, shock wave-boundary layer interaction, and the wake behind the body. Geometric changes refer to vehicle shape alterations that disrupt the flow field. Shock wave-boundary layer interactions occur when shock waves induced by the vehicle interact with the boundary layer. Finally, the wake is the region of disturbed flow that occurs downstream of the body where flow rotations occur, forming vortices of varying strengths based on the vehicle's shape and flow speed [4].

### Geometric Change in Vehicle Shape

Geometric changes in the vehicle shape prone flow separation. Hammerhead fairings design, with the diameter transition between the fairing and the following launcher stages, can cause flow separation that exposes critical areas of the vehicle to strong pressure fluctuations. The region along which the diameter change occurs is called boat-tail (see Figure 1.3), and as shown in Figure 2.4 that area induces reverse flow, thus causing the mentioned flow separation.

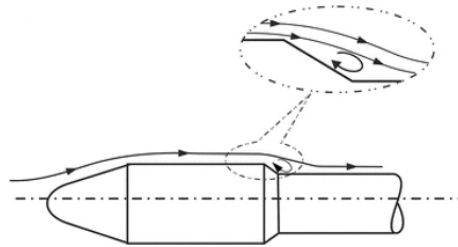


**Figure 2.4:** Separated flow due to geometric change at boat-tail region. [4]

The flow detachment, and consequent recirculation, induced in the boat-tail region justify the need to investigate its impact and seek shapes where unsteadiness is reduced. More in-depth analysis of the research conducted around the boat-tail is presented in section 2.2.2.

In addition, it is worth analysing the flow separation trend in the transition between the nose and the cylindrical portion of the payload fairing due to the aeroelasticity consequences it may have [7]. The cone-cylinder flow separation phenomenon, similar to what occurs in the PLF nose, was extensively researched in the 1960s, as detailed further in subsection 2.2.1.

### Backward Facing Step

Backward-Facing Steps (BFS) refer to expansions where the cross-sectional area suddenly increases. This geometrical configuration leads to a change in flow behaviour, inducing phenomena like separation, recirculation zones, and pressure fluctuations, making them a critical aspect of study in various engineering applications. In the case of launch vehicles, a smooth transition without any diameter change is desirable to avoid unsteady loads, equivalent to the case where no boat-tail exists. On the other side, if the boat-tail angle is set at the maximum angle possible of  $90^\circ$ , the resulting situation corresponds to a BFS.

The flow around a BFS exhibits the distinct features shown in Figure 2.5. The shear layer separation, recirculation region, and reattachment characterise the flow topology. At the BFS edge, the shear layer separates, creating a strong velocity gradient that induces a shearing force in the flow. The shear layer is bounded by the freestream above and the recirculation region below. Kelvin-Helmholtz's instabilities cause it to break down and roll into spanwise-oriented eddies. The maximum size of these eddies is equal to the step height. Depending on the specific geometry and flow conditions, the location where the separated shear layer attaches upon the lower step varies, leading to different levels of unsteadiness due to the shear layer separation and the recirculation region.

The walls of the BFS and the separated shear layer bound the recirculation region, which receives fluid from the impinging shear layer and the primary vortex. The amount of fluid entering the impinging shear layer varies, causing unsteadiness in the recirculation region. Finally, the BFS's wake exhibits large-scale dynamics and low-frequency oscillations due to the interaction of the aforementioned topological features.

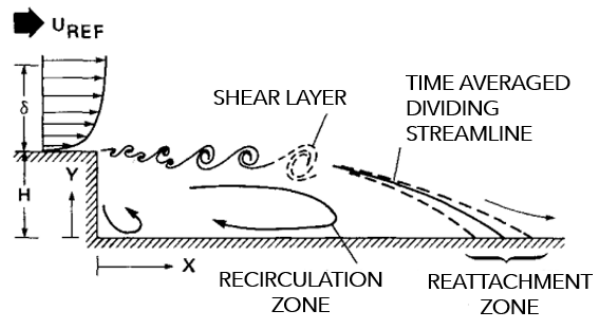


**Figure 2.5:** Backward-Facing Step (BFS) flow topology. [8]

### Shock Wave-Boundary Layer Interaction

Shock Wave-Boundary Layer Interactions (SWBLIs) occur when a shock wave interacts with the boundary layer of a surface. This interaction can occur as a result of a shock wave being generated elsewhere and impinging on the surface or due to the formation of an oblique shock wave caused by a slope in the surface. As a result of this interaction, there is a significant increase in pressure and temperature, as the shock imposes an intense adverse pressure gradient on the BL. This leads to the formation of a thick Turbulent Boundary Layer (TBL) which can cause the flow to separate from the surface [9]. In addition, the interaction between the shock wave and the boundary layer leads to a complex flow pattern that can cause flow unsteadiness and further exacerbate flow separation [10].

If the flow is supersonic, the compression process typically leads to the generation of a shock wave originating from the boundary layer. This phenomenon has an equivalent impact on the viscous flow as that of an impinging wave from an external source. In the transonic speed range, shock waves form at the downstream end of an enclosed supersonic region. When these shocks approach the surface, a shock wave-boundary layer interaction is produced [9].

SWBLIs can be classified as weak or strong interactions based on the viscous effects. Weakly interacting flows cause the thickening of the boundary layer, and no separation occurs in the interaction region due to a less strong shock wave. The streamlines are diverted, forming compression waves, which eventually merge into a shockwave outside of the boundary layer. Although a high pressure gradient exists across the shockwave, within the boundary layer, the pressure increase is spread on a wider region, leading to a gradual increase in pressure. Hence, in a weak interaction, no separation occurs immediately downstream of the shockwave, but it could still take place further downstream due to an increased adverse pressure gradient.

On the other hand, in strong SWBLIs, boundary layer separation occurs in the interaction region, leading to an upward bending of the streamlines, causing the formation of compression waves from the sonic line that will merge into an oblique shockwave [9, 11]. A second oblique shockwave occurs to realign the streamlines with the surface of the wall. The two oblique shockwaves meet in the triple point where they connect to the normal shockwave above them. This shockwave structure is known as a lambda,  $\lambda$ , shockwave because of its particular configuration. A slip line emanates from the triple point as the decrease in total pressure across the normal shockwave is larger than for the two oblique shockwaves, while the static pressure behind them is the same.

In transonic conditions, the most significant case is the interaction with a normal shock wave. The characteristics of this interaction can vary depending on the state of the boundary layer, allowing for the differentiation between a laminar or turbulent shock wave boundary layer interaction. However, due to the high Reynolds number values typical of these conditions, the flow can generally be assumed to be turbulent.

The formation of shocks in the transonic regime can increase pressure drag, causing large differential pressures that result in an increased lateral load on the launch vehicle. In this regime, shocks formed on the surface oscillate and move back and forth due to shock wave-boundary layer interaction, leading to pressure fluctuations and unsteady loads (see Figure 2.6). The shock also interacts with the boundary layer and can cause flow separation from the vehicle, exacerbating these issues. The high dynamic pressure regime characteristic of this phase of flight makes it a cause for concern.

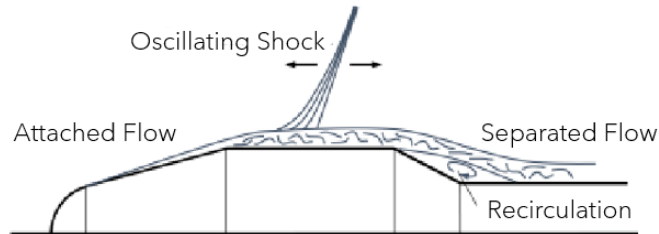


**Figure 2.6:** Transonic flowfield around hammerhead PLF. [12]

Unsteady shock waves lead to pressure fluctuations in the nose region. At higher transonic Mach numbers (between 1 and 1.2), the shock shifts downstream, closer to the boat-tail region, where vital electronic instruments are housed. Vibration transmitted into the structure can affect the performance of this equipment [13, 4].

### 2.1.3. Unsteady Loads

Unsteady flows are characterised by fluctuations in flow quantities over time, with pressure being the most significant variable for vehicle design. These fluctuations result in time-varying unsteady loads on the vehicle, which are critical in structural system design. A range of flow phenomena can cause these loads, including turbulence, wakes from protrusions, shock movements over the surface of the vehicle during transonic flight, and flow separation (see subsection 2.1.2) caused by shock wave-boundary layer interactions or geometrical separation and reattachment as shown in Figure 2.7.

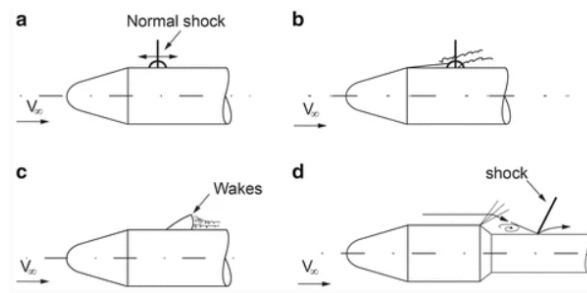


**Figure 2.7:** Causes of unsteady loads: (a) Movement of shock wave during transonic regime; (b) Shock Wave-Boundary Layer Interaction (SWBLI) which induces flow separation; (c) Pressure oscillation due to wake, and (d) Flow separation due to geometric shape and reattachment. [4]

The unsteady loads contain pressure fluctuations with different frequency contents, ranging from low to very high frequencies. Low-frequency contents can excite the vehicle's lateral flexible modes and introduce additional structural loads. Therefore, it is essential to consider them during the overall structural design of the launcher. High-frequency unsteady loads act as acoustic noise for local structural elements and require appropriate design improvements to ensure the structural integrity of sensitive components during flight.

Unsteady pressure measurements are taken at specific locations on rigid models during wind tunnel tests to characterise unsteady loads. Understanding the nature and effects of unsteady loads is critical for designing effective hammerhead PLF configurations, particularly in minimising structural loads and ensuring component durability [4].

### Buffeting

Buffet is the unsteady aerodynamic load that a vehicle structure experiences due to the fluctuating pressure in the surrounding airflow. Typically high-frequency, buffet loads are caused by unsteady airflow over a vehicle's surface and can result in rapid variations in the aerodynamic forces acting on it. This phenomenon can also be defined as "the repeated loading of a structure by an unsteady aerodynamic flow" [14] or as "high-frequency instability caused by airflow separation or shock-wave oscillations from one object striking another" [15]. For example, the flow separation induced by the boat-tail region leads to high levels of low-frequency wall pressure fluctuations (buffet) in areas of TBL separation, reattachment, and shock wave-boundary layer interaction [16, 17, 18]. For launchers, the typical Strouhal numbers for the unsteady modes are in the order of 0.1 to 0.3 [19].

Buffet loads can be classified into three types: transonic buffet, wake buffet, and shock-boundary layer separation buffet. Transonic buffet consists in shock movements during the low to high transonic regime of flight (Mach numbers between 0.8 and 1.2). Wake buffet is caused by unsteady flow generated by wakes from functional protrusions on the vehicle surface. Buffet loads are induced due to flow separation at the shock location, and the location of flow reattachment because of shock wave-boundary layer interaction [4].

Assessing buffet loads is crucial because their combination with the intense acoustic pressure fields typical of the transonic regime can induce significant noise and vibrations throughout the vehicle, potentially causing severe damage to both the structure and payload and leading to the failure of the entire satellite mission [20].

The significance of buffeting in hammerhead configurations has made it a well-researched topic. In the past, experimental methods were the only means of assessing such phenomena, as demonstrated by Andrews [21] and Cole [14]. However, with advancements in numerical techniques, particularly in CFD (Computational Fluid Dynamics), it is now possible to make initial assessments of buffeting before conducting experimental analyses, using available experimental data to validate the models. Several numerical studies are available on the topic, including Camussi et al. [22], Imperatore et al. [23], Kim et al. [12], Liu et al. [24], Panda [25], or Troclet and Depuydt [26]. However, it should be noted that these studies use RANS (Reynolds Averaged Navier Stokes) turbulence models, which may not be the best fit to properly model the characteristic unsteadiness of the flow in such conditions. In contrast, Chae et al. [27] combined RANS and DDES (Delayed Detached Eddy Simulation) models<sup>1</sup>, as only the DDES could reproduce the pressure perturbation induced by the shear layer unsteadiness at the boat-tail. Similarly, Murman and Diosady [29] use the Spalart-Allmaras turbulence model with modifications for DDES as a baseline, which then they complement with results using the Shear-Stress Transport (SST) model with DDES. From that study is worth noting that to properly assess unsteady phenomena, both numerical and experimental analyses were combined and compared. Many other numerical research in the field have followed the same strategy, like the one by Liu et al. [24] who also employs DDES and experimental data to assess the unsteady aerodynamic loads associated with transonic buffet flow.

---

<sup>1</sup> **DDES**: modification of a RANS equations model in which the model switches to a subgrid scale formulation in regions fine enough for large eddy simulation (LES) calculations [28].

### Guidelines for Free-Buffer

As described in the previous section, the combination of buffet loads with the intense acoustic pressure fields common in the transonic regime can provoke noise and vibrations which may damage the structure and payload. For that reason, launch vehicles should avoid buffet loads by implementing a suitable aerodynamic configuration design. The forebody configuration of a launch vehicle is critical, as it heavily influences the aerodynamic flow behaviour during atmospheric flight and dominates the buffet contributions. As a result, the payload fairing configuration plays a significant role in generating buffet loads.

NASA developed a handbook [14] containing general design PLF guidelines for achieving a buffet-free configuration, which is highly recognized and referenced in the field. These guidelines are based on extensive wind tunnel testing. Table 2.1 outlines the main recommendations for achieving a buffet-free configuration for the forebody geometry shown in Figure 2.8.

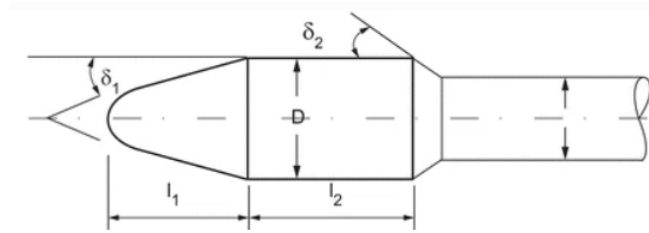


**Figure 2.8:** Geometrical parameters of the forebody representing a hammerhead PLF configuration. [4]

**Table 2.1:** General guidelines for the buffet free configuration as per the geometry of Figure 2.8. [14]

Geometrical parameter	Criteria		
	Buffet free	Stable buffet	Unstable buffet
$l_1/D$	$\geq 0.8$	-	-
$l_2/D$	$> 1.5$	-	-
$\delta_1$	$\leq 15^\circ$	-	-
$D/d$	$< 1.1$	$< 1.6$	$> 1.6$
$\delta_2$	Not critical		

Strict adherence to the buffet-free configuration guidelines may sometimes make it impossible to accommodate the payload within the available space inside the payload fairing. As a result, launch vehicle configurations are generally designed with a stable buffet configuration. Vehicle structural design loads are adjusted to account for these additional contributions from the stable buffet loads.

### Aeroacoustics

Aeroacoustics refers to the noise generated by pressure fluctuations in the aerodynamic flow. This phenomenon is particularly pronounced during transonic shock oscillations, flow separation, and reattachment resulting from geometrical features such as payload fairing boat-tails and protrusions. While buffet loads affect the overall structural design of the vehicle, the dynamic load generated by aeroacoustics affects the design of local structural systems. Therefore, sensitive subsystems like avionics, sensors, and control system actuators installed near critical locations, such as flow reattachment points, need to be tested to determine the levels

of environmental noise they can withstand. If the test results indicate high levels for such components, design modifications are required, and protective measures must be taken.

To accurately assess aeroacoustic levels during different flight regimes at various locations on the vehicle, unsteady pressure measurements are taken using wind tunnel models. These measurements are used to calculate acoustic levels, accounting for the steady and unsteady components of the pressures recorded in the wind tunnel [4]. For example, Camussi et al. [30] used such measurements to evaluate the VEGA-C launcher's aeroacoustic performance, where buffet occurrence was deemed as not expected generally. Moreover, the full-scale extrapolation of the measured spectra showed that pressure fluctuations are not expected to excite the main structural modes of the launcher. While experimental testing is the most reliable method to assess aeroacoustic loads, numerical simulations can also provide valuable insights, as shown in the work of Murman et al. [31].

#### 2.1.4. Wake Reattachment

Hammerhead payload fairings are prone to flow separation, as discussed in Section 2.1.2. However, the separated flow can reattach due to the long, relatively uniform cylindrical region that follows the hammerhead shape. This phenomenon is significant and must be considered during the design of hammerhead payload geometries, as it can impact the vehicle's aerodynamic performance and structural integrity.

Ericsson [32] has emphasised the importance of studying hammerhead wake reattachment. Interestingly, the NASA design criteria [14] does not account for this flow phenomenon, which is unavoidably associated with hammerhead payloads. Maintaining the vehicle's structural integrity relies on the wake reattachment. For instance, early studies of a biconic hammerhead geometry demonstrated the potential danger of hammerhead wake reattachment due to large aeroelastic effects observed at  $Ma = 0.9$  [33]. This finding was further confirmed by Ericsson's [32] comprehensive analysis of available hammerhead launch vehicle data, indicating that the reattachment of the hammerhead wake on the adjacent booster may cause aeroelastic instability for the lowest bending modes.

Another example is the Model 11 configuration (see subsection 2.2.3), which adheres to NASA design guidelines [14]. Experimental results show that the wake reattachment on its downstream cylinder generates a negative normal force, as illustrated in Figure 2.9 [34].

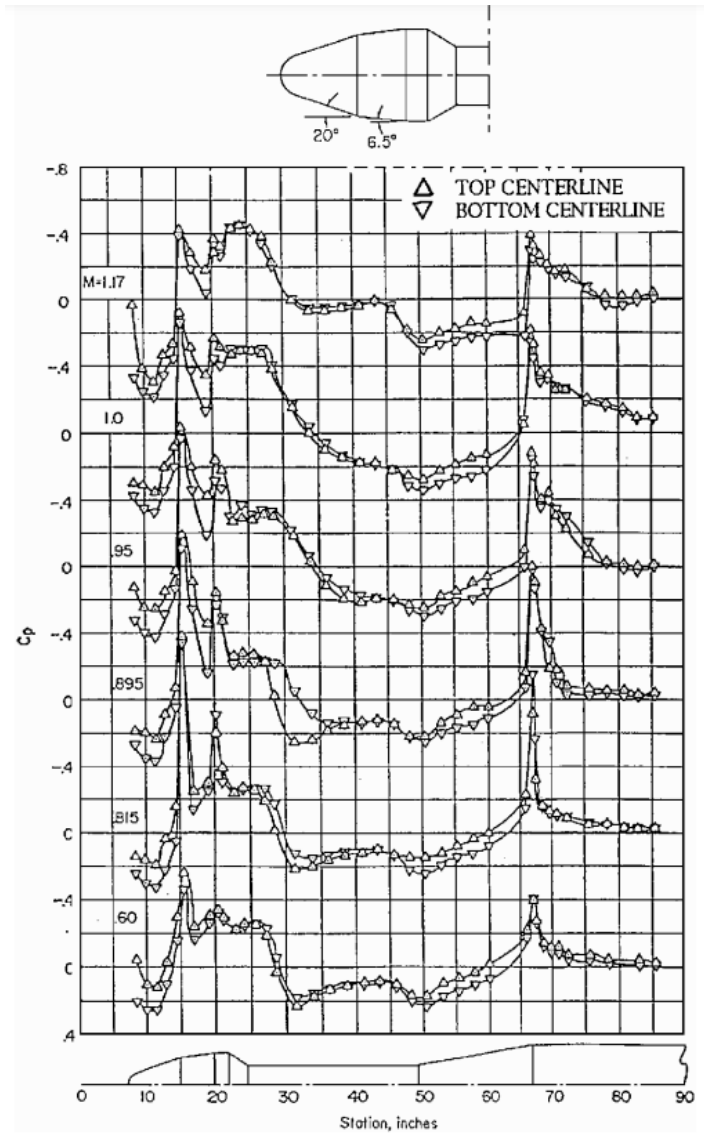


**Figure 2.9:** Pressure distribution on NASA's hammerhead geometry Model 11 at an angle of attack of 4 deg for subsonic and transonic speeds. [32]

## 2.2. Payload Fairings Design

Payload fairings are essential components in the launch vehicle design process, as they protect payloads during the aerodynamic phase of flight. PLFs are designed to ensure minimum drag and provide a smooth, streamlined surface for the payload to travel through the atmosphere. For that reason, the aerodynamic design of PLFs is crucial to ensure the successful deployment of the payload into orbit. Hammerhead payload fairings are characterised by a PLF diameter bigger than the rest of the launch vehicle (see Figure 2.10). The need for such configurations comes, as already discussed in chapter 1, because while the propulsion system determines the vehicle diameter, the diameter of the PLF is decided based on the payload requirements. In situations where the PLF requires a larger diameter than the rest of the vehicle, the cylindrical part of the fairing is joined to the rest through the boat-tail [4]. Over the years, various configurations of hammerhead PLFs have been proposed and studied to improve and understand their aerodynamic performance.

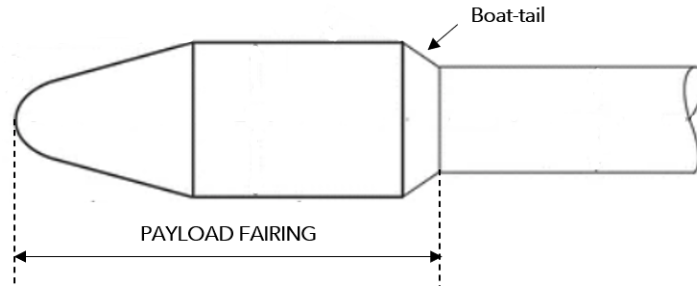


**Figure 2.10:** Schematic representation of a hammerhead-shaped fairing with the boat-tail region indicated. Based on [4].

### 2.2.1. Nose Shapes

The payload's size and volume determine the dimensions of the payload fairing (PLF), whose shape is then optimised to minimise the aerothermal impact on the launch vehicle and its sub-systems. The nose section's design significantly impacts the PLF's aerodynamic performance and overall geometry, which usually takes the form of either an ogive or conical shape (Figure 2.11).

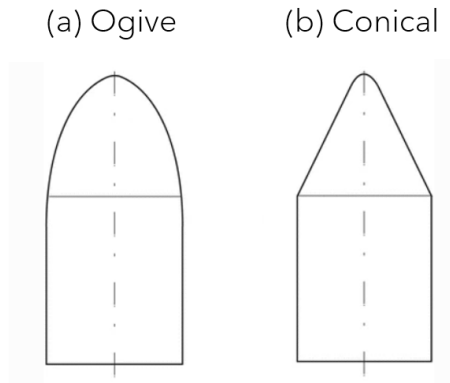


**Figure 2.11:** Generic PLFs nose shapes. Based on [4].

The ogive shape provides a larger volume to accommodate payloads, with better aerodynamic characteristics and reduced drag, resulting in minimum unsteady loads for both the launch vehicle and the satellite. However, manufacturing an ogive-shaped PLF to the required precision level can be challenging, and any deviation can result in higher unsteady loads. In contrast, the conical shape is easier to manufacture but generates more drag and higher unsteady loads. Regardless, the variations in unsteady loads due to manufacturing-induced changes in geometry are minimal. The actual height and mass of the PLF, whether ogive or conical, depends on the satellite's volume requirements and actual aerodynamic loading conditions [4].

In terms of design, the ogive definition encompasses diverse shapes, including the elliptical, parabolic, and Sears-Haack configurations, listed in order of most to least drag. The Sears-Haack shapes are particularly interesting as they are mathematically derived to minimise drag. The series is a continuous set of shapes determined by the value of a constant named  $C$  in the Equations (2.1). Two values of  $C$  have a particular significance. When  $C = 0$ , the shape is also known as the Von Kármán shape, which minimises drag for a given length and diameter (see Figure 2.12). On the other hand, for  $C = 1/3$ , the shape minimises drag for a given length

and volume.

Although the Sears-Haack shape is more commonly observed in academic research, it holds great potential for industrial applications due to its favourable drag characteristics.

$$\begin{aligned}\theta(x) &= \arccos\left(1 - \frac{2x}{L}\right) \\ y(\theta, C) &= \frac{R}{\sqrt{\pi}} \sqrt{\theta - \frac{\sin(2\theta)}{2} + C \sin^3(\theta)}\end{aligned}\tag{2.1}$$

where  $L$  refers to the length,  $R$  to the radius and  $x$  refers to the  $x$ -coordinate.



**Figure 2.12:** Sears-Haack minimum drag for given length and diameter series type nose shape (also known as Von Kármán). Source: Wikipedia

As discussed in subsection 2.1.2, the transition from the nose to the cylindrical portion of the PLF can lead to flow separation, impacting the aeroelastic stability of the launch vehicle. Consequently, research on phenomena such as cone-cylinder flow separation (which can be compared to the nose-PLF transition) has been ongoing since the 1960s. For instance, Coe [16] compared the flow around several models with different nose geometries during NASA's aerodynamic studies on launcher PLF configurations in 1962. However, as the PLFs evaluated in that study were all different (Figure 2.14), drawing specific conclusions about the nose's effect is challenging. For certain geometries as the elliptical used in models II and IV (see Figure 2.14), the conclusions drawn around the advantage of avoiding the boat-tail or reducing the diameter following a payload fairing are clear, but when trying to compare between nose shapes the available results complicate the attempt.

Similarly, Ericsson's [32] conclusion that bi-conic nose geometries prevent sudden changes in flow separation topology and reduce aeroelastic instabilities based on his previous work [35] appears to lack a solid foundation. As shown in Figure 2.13, the results suggest that pre-separation at the bi-conic shoulder allows the boundary layer to negotiate the nose-cylinder shoulder without separating, contrary to the case with a conic nose. Nevertheless, such conclusions cannot directly be extended to any case as the geometric differences between both models are not only in the nose, and the flow conditions tested are not the same. Thus, a comprehensive analysis between conic and bi-conic nose designs for comparable situations is still lacking.

The most common nose shapes in the industry are spherically blunted conic, bi-conic and ogive (see Section 2.2.3). The ogive PLF configuration is commonly preferred over traditional

cone-cylinder designs due to its ability to gradually expand the flow, resulting in a weaker terminal shock on the cylindrical section of the fairing, leading to reduced aero-acoustic noise levels [36].

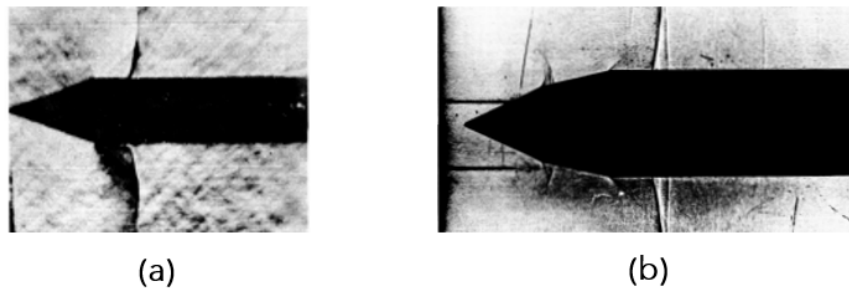


**Figure 2.13:** Shadowgraphy of the flow over a (a) Cone-Cylinder Body and the (b) Saturn IB SA-203 vehicle at Mach 0.89 and 0.9, respectively. [35]

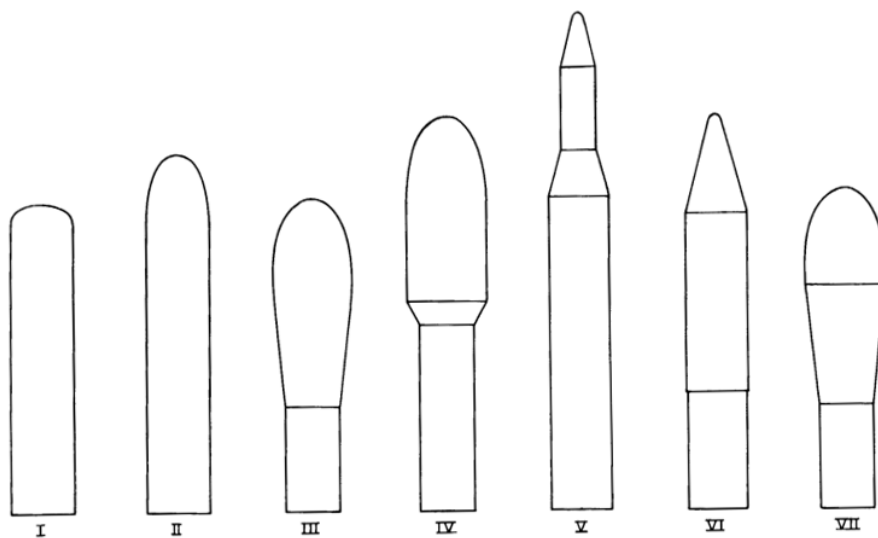


**Figure 2.14:** Model profiles tested by Coe [16] to evaluate the impact of nose shape at transonic speeds.

### 2.2.2. Boat-Tail Region

The Boat-Tail (BT) region in hammerhead configurations corresponds to the area where the cylindrical portion of the fairing transitions to the remainder of the vehicle due to a diameter difference (refer to Figure 1.3 or Figure 2.11). As discussed in Section 2.1.2, this geometric alteration exposes the vehicle to significant areas of flow separation and high-pressure gradients (similar to the ones observed in the “extreme” case where the boat-tail angle equals  $90^\circ$ , equivalent to a backward facing step, see Figure 2.1.2), underscoring the need to investigate the effects of the boat-tail on the flow.

Numerous studies have analysed and characterised the flow around boat-tails, most focusing on conventional conical boat-tail configurations. For instance, Kumar et al. [13] and Medeiros et al. [3] conducted experimental investigations in transonic regime to assess the impact of several boat-tail angles (15, 31.5 and 90 degrees in Kumar’s study and 8, 16, and 90 degrees in Medeiros’) on hammerhead PLFs with a generic ogive shape nose or the VLS-1 shape, respectively. For the range of Mach numbers and model configurations studied by

Kumar et al. [13], two types of boat-tail flows were observed (Figure 2.15): one where the boundary layer separation occurred at the boat-tail corner with reattachment downstream on the cylinder surface (Type I) and another where the shock-induced boundary layer separation took place along the boat-tail with subsequent reattachment on the cylinder surface (Type II) for very few cases. This corresponds to the three ranges set by Suresh et al. [4]: below  $5^\circ$ , the shock is weak; beyond  $30^\circ$ , a wake-like separated flow over a long zone occurs; and between  $5$  and  $30^\circ$ , the shock incidence on the boat-tail is strong, resulting in high loads.

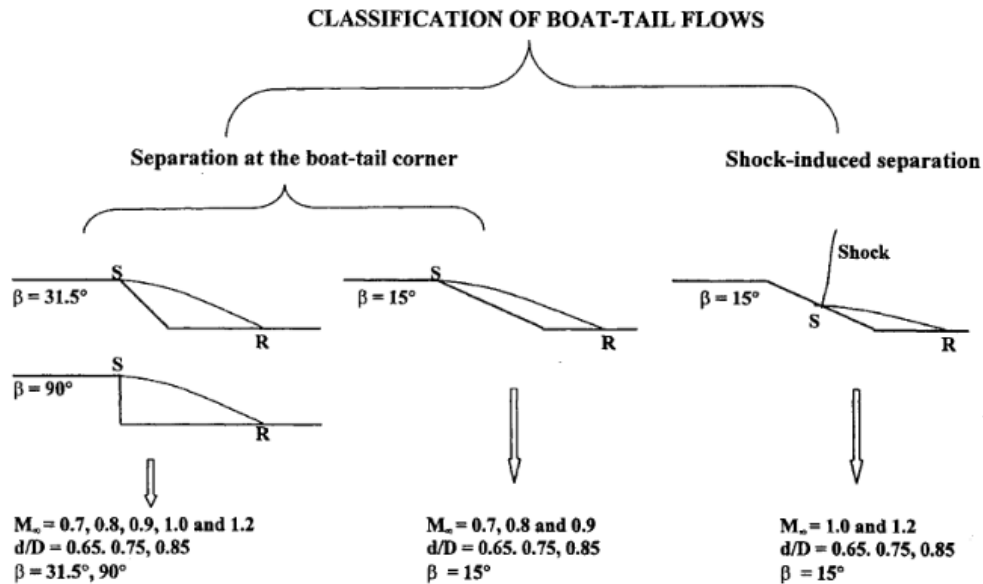


**Figure 2.15:** Schematic of observed boat-tail flows. [13]

However, only some studies have explored the impact of the boat-tail shape. Sachdeva identified this gap [37] and conducted CFD simulations at a Mach number of 0.9 to optimise the boat-tail region (parameterised using a Bézier curve) by reducing flow separation and boat-tail length. The study revealed that a stepped boat-tail configuration with an approximately 7-degree boat-tail angle could reduce the separation length by a minimum of 40% in all Mach numbers studied compared to a conventional BT configuration. Moreover, such a design resulted in lower Turbulent Kinetic Energy (TKE) than a straight boat-tail configuration, which may lead to reduced aeroacoustic levels. Similarly, Sunil [38] conducted an aerodynamic shape optimisation study of PLF boat-tails for various diameter ratios using genetic algorithms and CFD, also resulting in improvements in both TKE and drag reduction compared to conventional conical boat-tails with the same length and height. However, none of these studies consider the specific impact of the nose geometry and instead use a generic, undefined design.

### 2.2.3. Common Hammerhead Payload Fairing Geometries

This section aims to provide a comprehensive overview and comparison of the hammerhead payload fairing configurations commonly used in both academia and industry. The previous chapter presented the basic concepts and geometries of the hammerhead configuration, and this section will delve into the details of specific designs and variations. By examining both academic and industrial designs, this section aims to highlight the differences and similarities between the two and provide insights into the state of the art in hammerhead PLFs design.

### Benchmark Research Configurations

The literature on hammerhead configurations commonly employs a specific geometry for experimental and numerical studies known as Model 11. Coe and Nute [34] initially used this model in their research around steady and fluctuating pressures at transonic speeds on hammerhead launch vehicles, where two other geometries were tested (see Figure 2.16). Their study demonstrated how flow separation due to the hammerhead configuration could expose large areas of the vehicle to pressure fluctuations. Model 11, which is an axisymmetric, protuberance free hammerhead-shaped model (see Figure 2.17), exhibited the highest fluctuations due to separation and the greatest length of unsteady flow among the three models experimented.

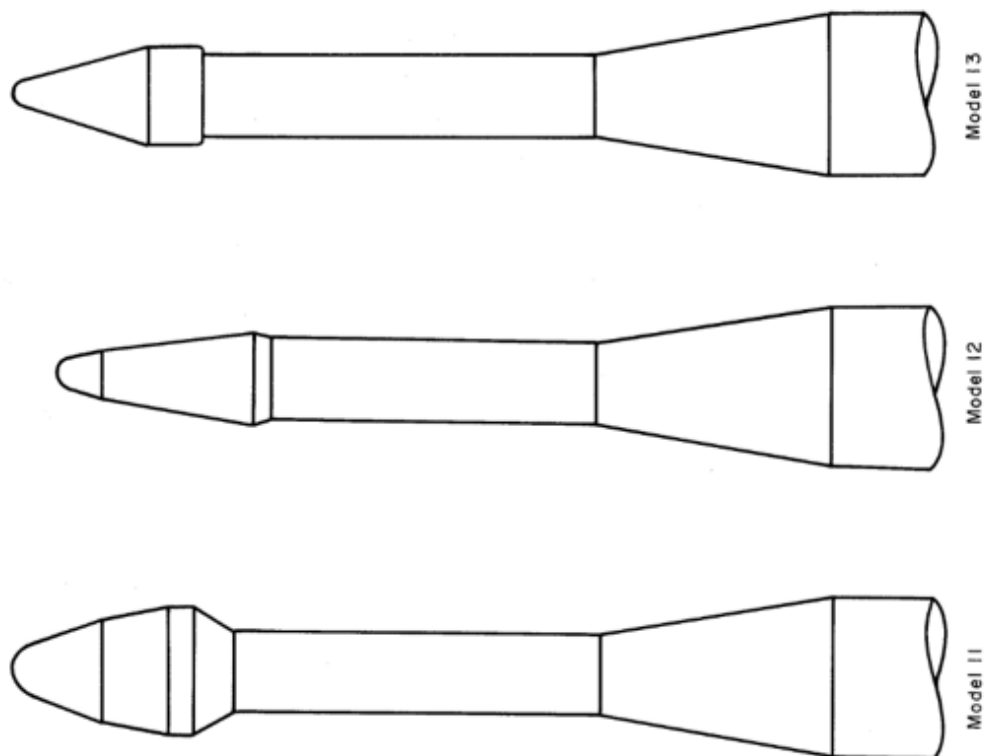


**Figure 2.16:** Hammerhead launch vehicles models tested by Coe and Nute [16].

This model has attracted interest in the test and validation community because it embodies many of the unsteady aerodynamic issues faced by all space vehicles during transonic and supersonic flights through the dense part of the atmosphere. Specifically, it experiences fluid dynamic phenomena such as flow separation, transonic shock formation, and unsteady force generation. Moreover, various dimensions of the model, such as the ratio of the diameters of the payload fairing to that of the second stage and the length of the second stage to the diameter of the payload fairing, follow the general recommendation of the NASA handbook for a buffet-free configuration [14]. Finally, much data valuable to validate numerical models or experimental results is available for this specific geometry.

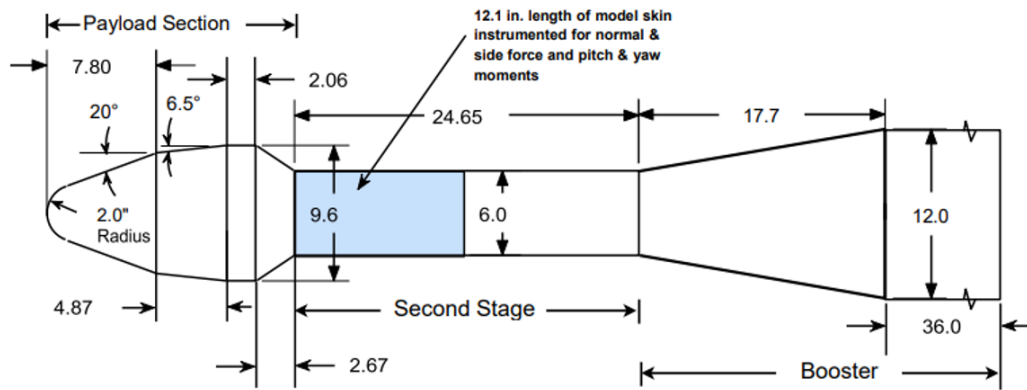


**Figure 2.17:** Dimensions of the NASA-developed Hammerhead Launch Vehicle Model 11, originally tested by Coe and Nute [16], in inches. [39]

Several papers in the literature have used the Model 11 hammerhead configuration, apart from Coe and Nute [16] or Panda [39], including the work by Kim et al. [12], Liu et al. [24], and Murman and Diosady [29].

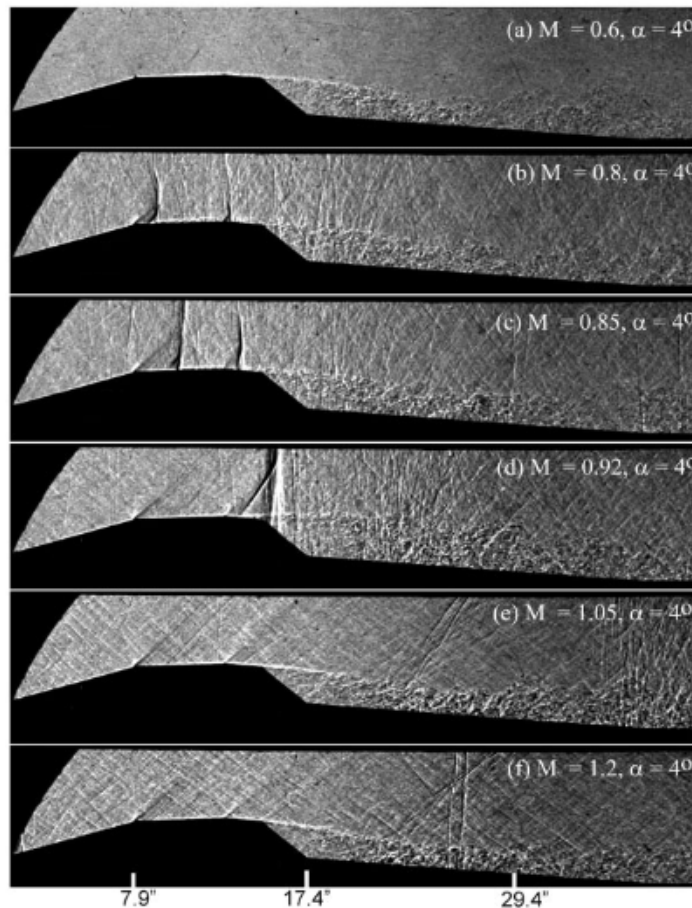


**Figure 2.18:** Shadowgraphy images of the upper half of the model at an angle of attack of 4 degrees and the indicated Mach numbers: (a)  $Ma = 0.6$ ; (b)  $Ma = 0.8$ ; (c)  $Ma = 0.85$ ; (d)  $Ma = 0.92$ ; (e)  $Ma = 1.05$ ; (f)  $Ma = 1.2$ . [39]

Figure 2.18 from Panda et al. [39] shows shadowgraphy images of the model's upper half that allow distinguishing the primary flow phenomena around the model. The central feature is the shear layer separation due to the geometry change induced by the sharpness of the boat-tail. The separated shear layer reattaches some distance downstream in the second stage, creating high-pressure fluctuations around the impingement location. This flow phenomenon is observed at all assessed Mach numbers. At the lowest Mach number of 0.6, no shock waves appear. However, for higher values, local shock and separation events occur. Clear normal shocks form at the end of the two locations (junction between two conic sections and the transition from cone-cylinder) associated with a sudden area increase on the PLF. The SWBLIs in those locations create large spikes in pressure fluctuations, as shown in Figure 2.19 where measured root mean square pressure coefficient distributions are shown. The supersonic bubble grows by increasing the Mach number, pushing the shock waves downstream. At Mach 0.92, the supersonic flow covers almost the entire PLF, with both normal shocks coalesced into one and standing at the boat-tail region. Shock waves disappear with a further increase of the free-stream Mach number to 1.05.

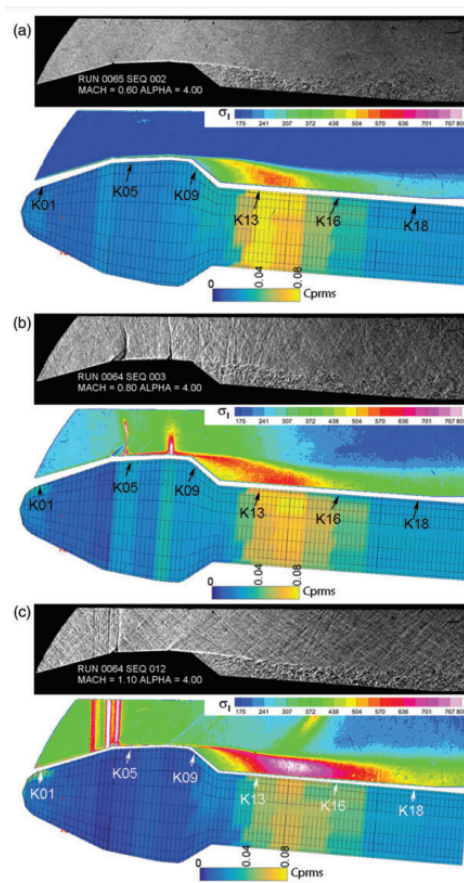


**Figure 2.19:** Composite of shadowgraph image, rms (root mean square) of light intensity fluctuations calculated from the high-speed shadowgraph images, and distribution of  $C_{p,rms}$  measured by dynamic pressure sensors at an angle of attack of 4 degrees and the indicated three Mach numbers. (a)  $Ma = 0.6$ ; (b)  $Ma = 0.8$ ; (c)  $Ma = 1.1$ . [39]

The already presented Figure 2.19 presents composite images that further illustrate the origins of the high-pressure fluctuations. The composite images consist of three parts, two of which come from the high-speed shadowgraph camera, while the third component is sourced from data collected through dynamic pressure sensors. The single frames obtained from the

camera provide snapshots of the flow features, while the 2D plots of the standard deviation of the light fluctuations  $\sigma_l$  offer further information on the airstream's unsteadiness. It is worth noting that the same colour scales were used for all  $\sigma_l$  and  $C_{prms}$  cases. Upon examination of the composite images, it becomes apparent that the pressure fluctuations remain predominantly low on the PLF, except when transonic shocks are present (Figure 2.19b). These shocks tend to thicken the BL and increase unsteadiness. The first shock generates high fluctuations further amplified by the second shock.

### Industry Examples

This section provides an overview of the current and historical industry launchers that utilise the hammerhead payload configuration. In the United States, the Titan IVB was among the launchers that used this configuration from 1989 to 2005, featuring a spherically blunted bi-conic nose (see Figure 2.22). However, due to high operational costs and concerns over propellants, the Titan IVB was retired. The Atlas V, an expendable launch system and the fifth major in the Atlas launch vehicle family replaced the Titan IVB. Although initially designed by Lockheed Martin, the Atlas V is now operated by United Launch Alliance (ULA), a joint venture between Lockheed Martin and Boeing. The Atlas V was retired in 2021, but during its operational period, it had several payload fairing options (see Figure 2.20), all utilising a hammerhead configuration. The fairing options with a 4-m diameter presented a spherically blunted conical nose, while the others had spherically blunted tangent ogive noses.

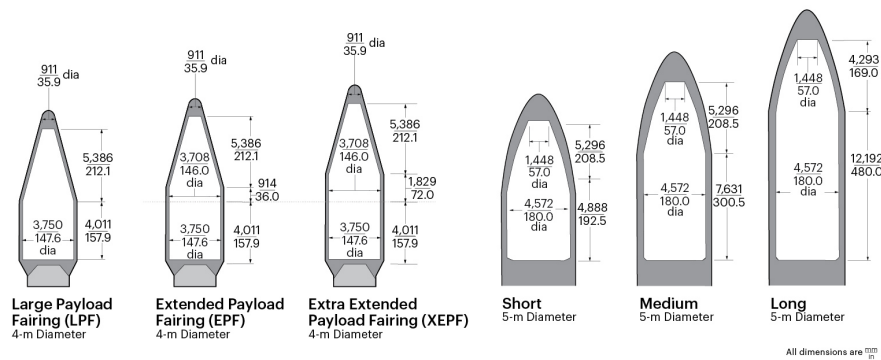


**Figure 2.20:** Payload fairing options for the Atlas V launcher. Source: ULA Launch

Another ULA launcher with the hammerhead PLF configuration was the Delta II (see Figure 2.23), which was retired in 2018. Like the Atlas V, the Delta II also had several payload fairing options (see Figure 2.21) that included spherically blunted tangent ogive or spherically blunted bi-conic noses.

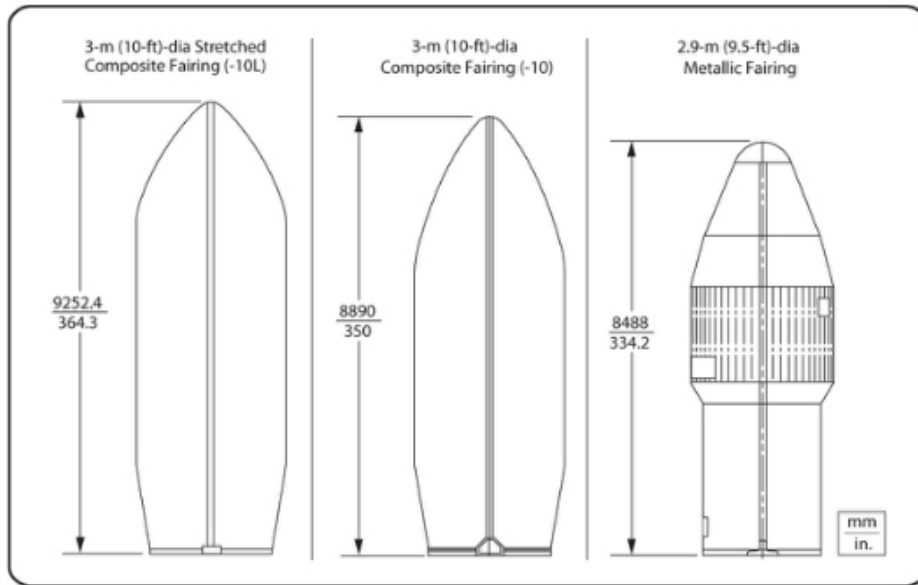


**Figure 2.21:** Payload fairing options for the Delta II launcher. Source: Wikipedia



**Figure 2.22:** Titan IVB launcher.  
Source: National Museum



**Figure 2.23:** Delta II launcher. Source: ULA Launch

The most recent American launchers to use the hammerhead configuration are the Falcon 9 and Falcon Heavy by SpaceX (see Figure 2.24), both featuring a spherically blunted ogive nose.



**Figure 2.24:** Falcon 9 and Falcon Heavy launchers. [2]

In South America, the Brazilian Space Agency's main satellite launch vehicle, the VLS-1, which was operational from 1997 to 1999, also featured a hammerhead configuration (see Figure 2.25a) with a spherically blunted conical nose [40].

In Europe, Ariane's Vega launchers utilise a hammerhead configuration. An example is the Vega C, which features a spherically blunted ogive nose (see Figure 2.25b). The Russian Soyuz-2 PLF, observed in Figure 2.25c, features a spherically blunted conical nose.



(a) VLS-1 launcher. Source: Wordpress

(b) Vega C launcher.  
Source:  
ArianeSpace

(c) Soyuz-2 launcher. Source:  
Gunter's Space page

**Figure 2.25:** VLS-1, Vega C and Soyuz-2 launchers.

In Asia, launchers from the Indian (Figure 2.26a), Japanese (Figure 2.26b), and Chinese (Figure 2.26c) space agencies also utilise the hammerhead configuration. Moreover, for these cases, the noses used are generally spherically blunted bi-conic, or ogive, as observed for the agencies and companies mentioned above.



(a) GSLV-MK-III launcher. Source: SpaceFlight 101 (b) JAXA H-IIB launcher. Source: TechCrunch+ (c) CZ-6 (Long March 6) launcher PLF detail. Source: China Space Report

**Figure 2.26:** GSLV-MK-III, H-IIB and CZ-6 launchers.

### 2.3. Flow Measurement Techniques Used in PLFs Aerodynamic Research

Different types of sensors, such as accelerometers, are used to assess unsteady loads like buffet and aeroacoustics [41]. However, for a proper understanding of the flow phenomena happening around a payload fairing, many authors have relied on optical measurement techniques. Among those, the techniques found in the literature are mostly oil flow visualisation, shadowgraphy and schlieren.

Oil flow visualisation is a qualitative technique widely used in aerodynamic research due to its simplicity and low cost. Moreover, it is often used in conjunction with other flow measurement techniques to validate and supplement quantitative data. Although spatial resolution and accuracy are limited, oil flow visualisation is valuable for gaining initial insights into complex flow phenomena.

Previous studies around the aerodynamics of hammerhead PLFs have used this technique for its simplicity and effectiveness. An example would be the studies around the aerodynamic performance of several VEGA launchers through numerical and experimental tools. Oil flow visualisation allowed CFD results to be validated [42, 43, 44, 45]. Figure 2.27 from Vitagliano et al. [45] shows how the experimental and numerical results provide similar flow patterns, only differing in the location of the boat-tail vortex due to the different Reynolds numbers.

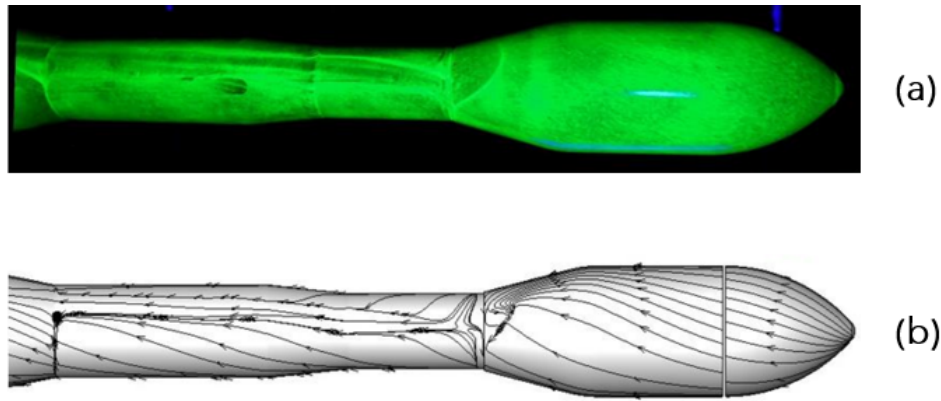


**Figure 2.27:** Oil flow visualisation (a) and CFD skin friction lines (b) at Mach 1.8 and angle of attack,  $\alpha$ , of  $10^\circ$ . [45]

Another case would be the research to understand mean surface pressure fluctuations in boat-tail separated flows relevant to launch vehicle configurations at transonic speeds by Kumar et al. [13]. Figure 2.28 shows the oil flow patterns obtained with two of the three tested boat-tail configurations for a diameter ratio of 0.65 at Mach 0.8. The pictures show that the boundary-layer separation occurred at the boat-tail corner while the reattachment happened downstream on the cylinder.

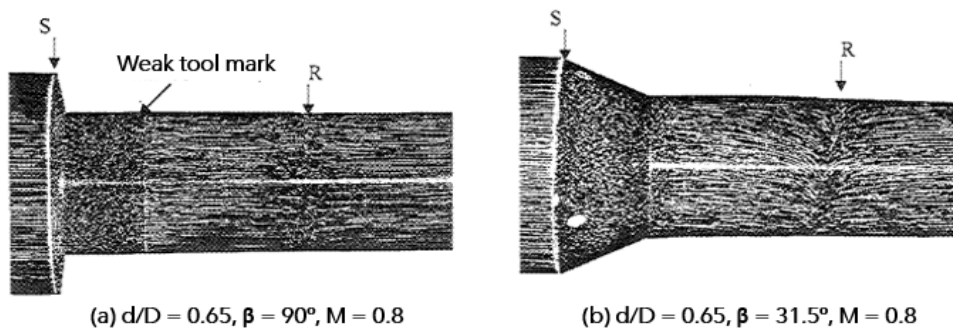


**Figure 2.28:** Oil flow visualisation photographs for a diameter ratio  $d/D = 0.65$ , a Mach velocity  $M = 0.8$ , and two different boat-tail angles  $\beta$ : 90 and 31.5 degrees. The boundary-layer separation is indicated by an S, and the reattachment by an R. [13]

Schlieren visualisation has been widely used in experimental studies of hammerhead PLFs in transonic regimes [22, 13, 3, 46, 47]. An example would be the experimental study of boat-tail variations effect on the flow patterns on a hammerhead PLF carried out by de Medeiros et al. [3]. In that study, Schlieren pictures for different boat-tail angles and Mach numbers are compared, clearly showcasing the shock wave development as the Mach number increases. For a boat-tail angle of  $90^\circ$  and Mach equal to 1, an expansion wave can be observed around the cylindrical section, followed by a normal shock wave downstream the boat-tail section (see Figure 2.29).

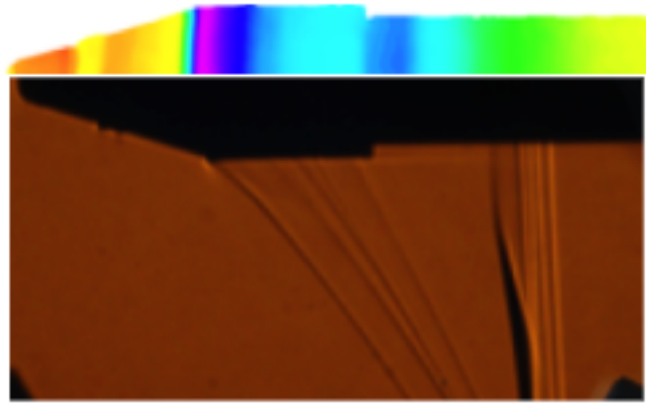


**Figure 2.29:** Schlieren image together with PSP (Pressure Sensitive Paint) results for  $Ma = 1.0$  and boat-tail angle of  $90^\circ$ . [3]

Finally, another very relevant optical measurement technique is PIV (Particle Image Velocimetry). Its effectiveness has been tested in various regimes, including transonic and supersonic flows [48]. In the transonic regime, PIV has been used to study shock waves, boundary layer separation, and flow control. Some examples are the measurements of transonic flow fields at a trailing edge model of a turbine blade made by Raffel [49], and the studies around transonic buffet in supercritical airfoils performed at TU Delft by several researchers [50, 51].

In 2010, the Delft University of Technology (TU Delft) and the Netherlands Aerospace Centre (NLR) collaborated on a research project funded by the European Space Agency's Basic Technology Research Programme (TRP) titled "Unsteady Subscale Force Measurements within a Launch Vehicle Base Buffeting Environment". The project's goal was to investigate the phenomenon of buffeting on the base of an Ariane 5 launch vehicle during the transonic regime. For that purpose, various Ariane 5 configurations were tested using a 1/60 scale model, which included an optimised Vulcan 2 nozzle (the flight configuration of Ariane 5 ECA). The research included both steady and unsteady surface pressure measurements, as well as flow field measurements like velocity fields (as seen in Figure 2.30) based on time-resolved (high-speed) PIV [52, 19].

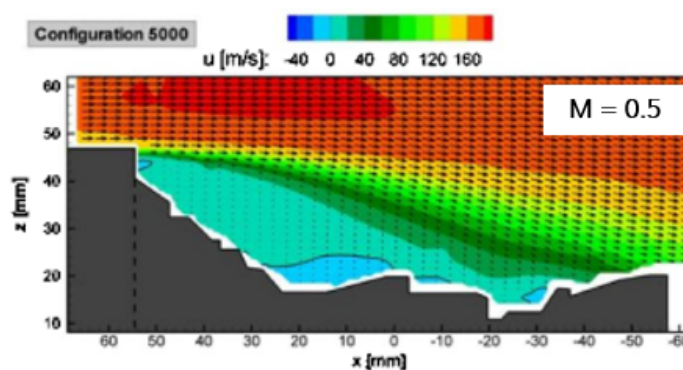


**Figure 2.30:** Mean horizontal field on the base of the Ariane 5's configuration 5000 main launcher for  $Ma = 0.5$ . [19]

The author has not found any application of this technique in hammerhead PLFs aerodynamics studies, the closest is the research by Koike et al. [53] who measured the velocity distributions around a rocket fairing model without boat-tail.

## 2.4. Discussion

This chapter presents an overview of the available literature on the aerodynamics of hammerhead PLFs. First, the transonic flow patterns of hammerhead PLFs are reviewed, emphasising how separated flow regions increase with the Mach number, leading to significant aeroelastic effects (see subsection 2.1.1). The primary causes of flow separation are identified as the geometry of the configuration and the shock wave oscillations induced by the transonic flow [13, 4]. Additionally, subsection 2.1.3 highlights the importance of considering unsteady loads experienced by the PLF during design, as they can cause the vehicle to fail. Neglecting flow separation can lead to aeroelastic instability, making reattachment of separated flow critical to maintaining the vehicle's structural integrity [32].

A comprehensive overview of the different nose shapes used in payload fairings is given in subsection 2.2.1, as their design significantly impacts aerodynamic performance. The literature review shows a research gap, as prior studies have not compared nose shapes under the same geometrical and flow conditions. For instance, Coe's [16] and Ericsson's [35] studies are not directly comparable. This limitation hinders the ability to draw reliable conclusions about the effect of nose shape on aerodynamic performance.

The boat-tail region is addressed in subsection 2.2.2, as it is prone to flow separation and high-pressure gradients. The available literature on the effects of this region is reviewed, showcasing promising results from studies that vary both the boat-tail angle and shape [13, 3, 37, 38].

An overview of common hammerhead PLF geometries is provided in subsection 2.2.3, starting with Model 11, the hammerhead model most commonly researched in academia and first studied by Coe and Nute [16]. Launchers from the leading space agencies and companies worldwide are also reviewed, giving a clear idea of how the industry generally designs hammerhead configurations.

Lastly, the flow measurement techniques used in previous research on PLFs' aerodynamics are summarised in section 2.3. The section highlights optical techniques for measuring airflow because the literature review already indicated the interest that understanding the overall flow patterns around these vehicles has. Another noteworthy aspect of this review is the novelty of utilising PIV within this field. No precedent instances employing PIV in such studies have been found, despite its potential to provide insights into phenomena like reattachment.

In conclusion, this chapter provides a comprehensive review of the aerodynamic features of hammerhead PLFs and valuable insights into the design of payload fairings, focusing on the impact of the nose and boat-tail regions. Future research should aim to improve the design and performance of launch vehicles by understanding the complex flow phenomena occurring in hammerhead PLFs. While aerodynamic optimisation traditionally focuses on minimising drag, the literature review performed in this chapter shows how assessing the unsteadiness and other flow phenomena induced by the geometry is more important in launcher design.

A clear gap in the literature is thus observed, as having proved how relevant it is to understand how such configurations behave in the transonic regime, no study where the combined effect on the flow of the nose and boat-tail geometries has been found.

## 2.5. Research Questions

The literature review showcases the relevance of studying the flow phenomena around hammerhead PLFs in the transonic regime. Moreover, a clear gap was identified, as many have studied the flow behaviour for specific launcher designs, but work in which the effect of varying angle of attack, velocity, nose and boat-tail shapes sequentially has yet to be performed. Thus, the influence that each of the parameters has in the flow has never been assessed and published to the author's knowledge. Being a configuration typically used to transport large

payloads, the flow separation and other unsteadiness that characterise such fairings promote interest in their study, reason why the writer is conscious that research on those matters has possibly been made but may not be publicly available.

An experimental study is chosen over a numerical one because RANS (Reynolds Averaged Navier Stokes) models generally used to study hammerhead configurations cannot correctly simulate the turbulence and unsteadiness characteristic of the flow in transonic conditions. On the other hand, more advanced simulations such as DNS (Direct Numerical Simulation) or LES (Large-Eddy Simulation) imply a very high computational cost.

For that reason, this thesis aims to contribute to the existing knowledge by investigating the effects of different nose cone geometries (conic, bi-conic, and ogive) and boat-tail angles (5, 15 and 34 degrees) at various Mach numbers (in the transonic regime) in a transonic wind tunnel. The study will employ Schlieren, oil flow visualisation, and Particle Image Velocimetry (PIV) techniques to gather detailed data measurements, with the latter being a novelty in the field. The results will offer a comprehensive understanding of the flow characteristics and the effects of nose and boat-tail regions on the aerodynamics of hammerhead payload fairing configurations in the transonic regime. Such research is relevant as the flow phenomena under these conditions may endanger the whole mission, turning these findings valuable for future designs.

The research objective could be phrased as follows:

***How do the nose and boat-tail geometries impact the flow phenomena (e.g., shock wave generation) around a hammerhead configuration PLF in transonic conditions?***

This question is relevant as understanding the effect of several generic shapes in the flow will improve the assessment of possible unsteady loads during the PLF design phase. On the other hand, the instrumentation available in the laboratory ensures that the question is researchable, even introducing novelty techniques in the field, as is the case of PIV.

The proposed question will be assessed by answering a set of sub-questions:

### **1. What are the distinctive flow patterns associated with different configurations?**

- How do flow variations manifest among the considered nose geometries?
- What are the flow distinctions observed across the range of boat-tail angles?
- Do different nose and boat-tail geometries yield similar flow phenomena under varying Mach numbers?
- Do different nose and boat-tail geometries yield comparable flow phenomena under varying angles of attack?

Hammerhead PLF configurations have been extensively researched in the literature. However, no specific studies in which the effect of varying geometry, Mach number and angle of attack separately is known by the author. Comparing flow patterns observed for different combinations can allow to conclude whether the generic flow patterns are common for all configurations and extract conclusions around the particular effect of each variable.

### **2. How do shock waves behave?**

- What are the phenomena surrounding the shock wave/s?
- What frequencies do the shock wave/s have?
- How does the shock wave location vary?

The shock wave behaviour, as it can be its oscillation or location, determines greatly how the forward and backward flow behave. The availability of instrumentation to perform testing with schlieren and oil flow visualisation ensures that the shock wave will be properly observed for all configurations tested.

**3. If existent, how is the hammerhead wake reattachment for each set?**

- Is there hammerhead wake reattachment in all nose and boat-tail combinations considered?
- What phenomena related to the reattachment can be observed?
- Is this phenomenon more prominent in conic nose configurations than bi-conic due to a reattachment in the second conic section as stated by Ericsson [32]?

The hammerhead wake reattachment, identified by Ericsson [32] as a critical factor in the design of hammerhead PLF configurations, can cause unsteadiness and potential structural collapse if not considered. This study aims to observe this phenomenon to discuss the conclusions of Ericsson's research further.

# 3

## Experimental Methodology

This chapter presents the experimental setup used to investigate the effects of the nose and boat-tail regions in the aerodynamics around hammerhead PLFs in transonic regime. The study was conducted at the High-Speed Lab (HSL) of the Aerospace Faculty at Delft University of Technology, specifically, in the transonic-supersonic wind tunnel (TST-27) [54].

The upcoming sections provide a comprehensive overview of the wind tunnel specifications, the aerodynamic models employed in the study, and the prevailing flow conditions. Furthermore, the measurement techniques employed for data collection are presented, along with a concise overview of the conducted uncertainty analysis. The experimental campaigns are also described, encompassing the configurations tested and the utilised setup. Finally, an inclusive portrayal of the data analysis conducted on the results culminates the chapter.

### 3.1. Test Facility

All tests presented in this report were performed in the transonic-supersonic blowdown wind tunnel (TST-27, see Figure 3.1), which can simulate airflow at Mach speeds ranging from 0.5 to 4.2 [54].



**Figure 3.1:** TST-27 wind tunnel (air flow from right to left) with the Schlieren set-up at z-configuration mounted (table on the right, the last mirrors and lenses together with the camera can be seen from setup described in Figure 3.15).

Optical access to the test section is provided by two 30 cm diameter circular quartz glass windows on either side of the wind tunnel (see Figure 3.2). Thanks to those, both PIV and Schlieren optical techniques can be used, and a full recording of the runs when doing oil flow visualisation can be done.



**Figure 3.2:** TST-27 test section with Coe and Nute's Model 11 base geometry configuration, also referred as benchmark configuration along the report. On the background, one of the mirrors used for the z-configuration Schlieren set-up is seen.

The tunnel stores dry and oil-free air at a pressurised vessel with a capacity of 300 m<sup>3</sup> for its functioning. Within the vessel, the air is maintained at a pressure of 40 bar. To ensure an ample air supply during testing, a multi-stage compressor system with a power rating of 230 kW is employed. This compressor system operates overnight in advance of the testing phase, resulting in a total approximate running time of 300 seconds per day, as the pressure in the storage vessel must not drop below 20 bar.

Regarding its aerodynamic performance, the tunnel can generate high Reynolds numbers across different flow regimes. Under transonic conditions, the maximum attainable Reynolds number per meter is 38 million. However, when operating in the supersonic range, the tunnel can achieve even higher Reynolds numbers, reaching up to 130 million per meter [55].

Supersonic Mach numbers ( $Ma = 1.15 - 4.2$ ) are achieved by utilising an adjustable throat equipped with flexible nozzle walls. This design, illustrated in Figure 3.3, incorporates a continuously variable throat ( $A_{t1}$ ) and flexible upper and lower walls. The flexibility of the walls allows for precise adjustments to the Mach numbers during a test run. In contrast, transonic conditions within the range of  $Ma = 0.5$  to  $0.85$  are attained through a variable choke mechanism,  $A_{t2}$ , positioned downstream of the test section,  $A_{test}$ . This mechanism, controlled by a Labview program detailed by van Rijswijk [56], plays a crucial role in achieving the desired Mach numbers. The transonic choke mechanism consists of eight biconvex rods, with four connected to the bottom wall and four to the top. Additionally, a wing, as depicted in Figure 3.4, is incorporated. The rods, whose excursion,  $H$ , can be adjusted, regulate the flow blockage, influencing the effective area of the downstream throat,  $A_{t2}$ , thereby altering the Mach number within the test section. Furthermore, the rotation of the wing allows for meticulous fine-tuning of the Mach number. With a thickness of 6 mm, the wing has a rotation range of 0 to 60 degrees. Prior to initiating a run, the rods are initially set according to the target freestream Mach number. Subsequent minor adjustments during the run are accomplished by rotating the central wing, facilitating precise control of the Mach number with an accuracy of up to the third decimal digit [50].

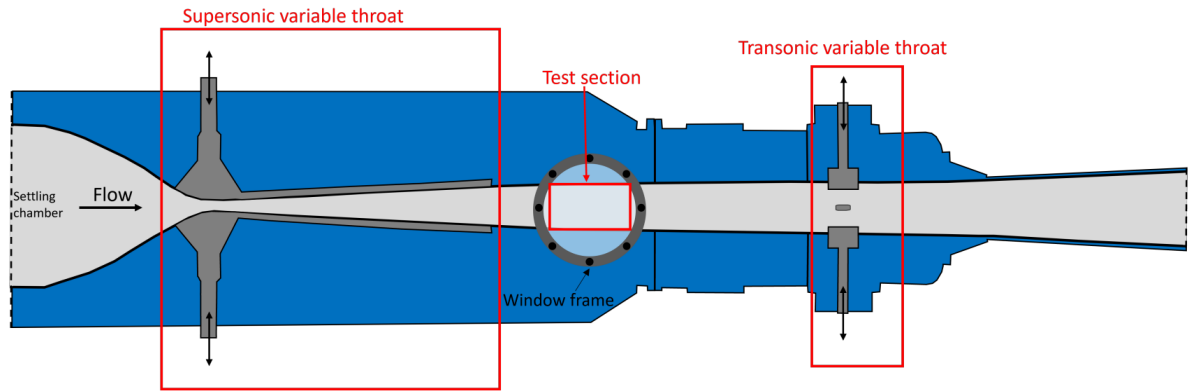


**Figure 3.3:** Technical drawing of TST-27 with indication of supersonic throat ( $A_{t1}$ ), test section ( $A_{t_{est}}$ ) and transonic throat ( $A_{t2}$ ). [50]

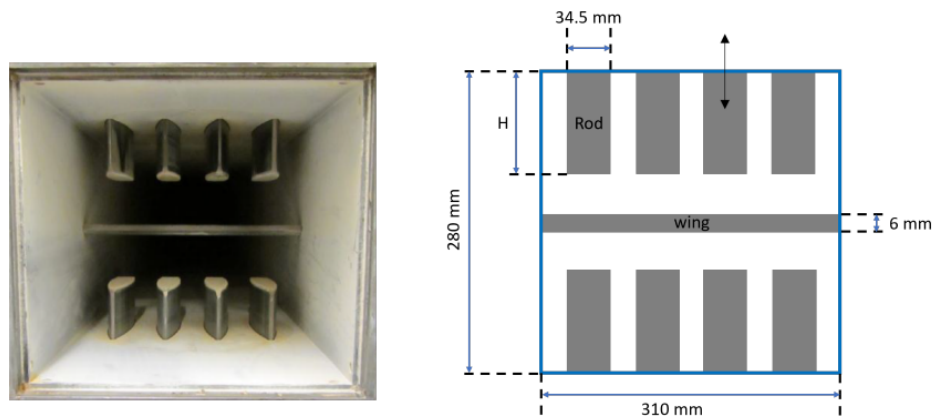


**Figure 3.4:** Transonic throat visualization (left) and schematic (right). [50]

The wind tunnel's modular design allows for the usage of three distinct test sections, namely closed wall, slotted walls, or perforated walls. Each module is equipped with wheels and is interconnected with the rest of the wind tunnel through quick-lock couplings. For the purpose of this thesis, all experiments have been conducted within the solid walls test section. This particular test section has been chosen to optimise the quality of the PIV raw images, considering the specific characteristics of the windows used. The solid walls test section is rectangular in shape, featuring dimensions of 0.255 m in height and 0.280 m in width.

## 3.2. Test Models

The design of the wind-tunnel model is based on the upper part of Model 11<sup>1</sup> (see subsection 2.2.3), which was first used by Coe and Nute [34] and is widely referenced in the literature to validate the aerodynamics of Hammerhead PLFs in the transonic regime (see Garbeff et al. [57] or Panda [39]). This model features a spherically blunted bi-conic nose, which, together with the ogive shape, are the industry's most commonly used nose types (see Figure 2.2.3). Hence, this model's utilization is advantageous as a validation reference and an appropriate starting point for investigating flow phenomena around hammerhead PLF configurations. The

<sup>1</sup>The back part of the launcher model (downstream of the wake reattachment) is not of interest for this research; for that reason, it is left out of the design. See complete original model in Figure 2.17.

model was scaled setting the PLF's diameter  $D$  to 50 mm, equal dimension to the FESTIP model tested at TU Delft [58, 51] (see Figure 3.5).

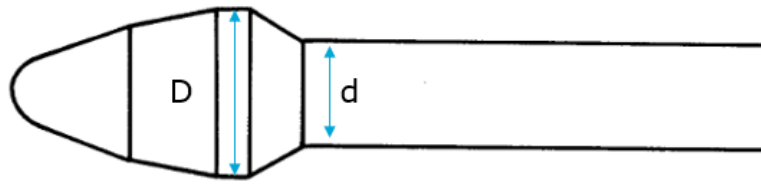


**Figure 3.5:** Schematic representation of the upper part of Model 11 used by Coe and Nute [34], showcasing the diameters of the PLF,  $D$ , and the rest of the vehicle,  $d$ .

Various nose geometries and boat-tail angles needed to be tested to address the research question and evaluate the impact of both the nose and boat-tail regions on the flow around a hammerhead PLF. As a result, a modular design was proposed to enable variations of both the nose and boat-tail. The interchangeable nose geometries and boat-tail angle elements were mounted onto cylinder section 02 (blue shaded in Figure 3.6), serving as the main component of the model.

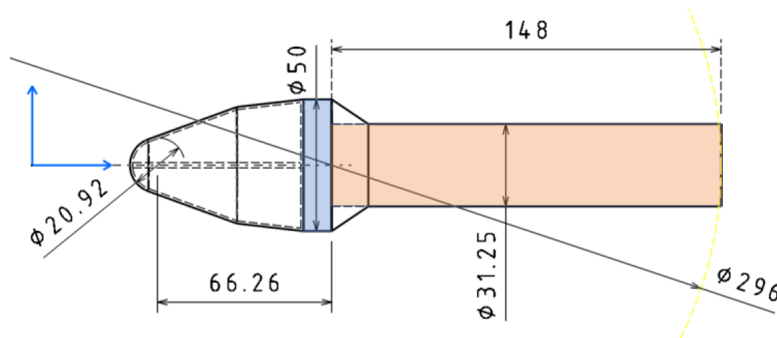


**Figure 3.6:** Schematic representation of the wind-tunnel model including the most representative dimensions in mm. In blue is shadowed the section numbered as 02 for the manufacturing, and in orange is coloured section 04 (being 01 the nose, and 03 the boat-tail area removable part).

The selected nose geometries include the Sears-Haack body cone (an optimised academic case of an ogive shape, chosen for research purposes) on the configuration known as the Von Kármán shape (minimum drag for a given diameter and length configuration, see subsection 2.2.1), conic, and bi-conic (see Figure 3.7). The choice of both bi-conic and ogive shapes stems from their broad applicability in the industry (see Figure 2.2.3). In contrast, the conic shape was chosen to assess Ericsson's [32] conclusion that bi-conic nose geometries mitigate sudden changes in flow separation topology and reduce aeroelastic instabilities compared to conic noses (see subsection 2.2.1) [35]. All these nose shapes were manufactured with equal length and diameter  $D$  (50 mm) to maintain overall model proportions (the specific dimensions can be seen in Figure 3.8). From Figure 3.6, it can be deduced that the diameter ratio for the model is  $D/d = 1.6$ .

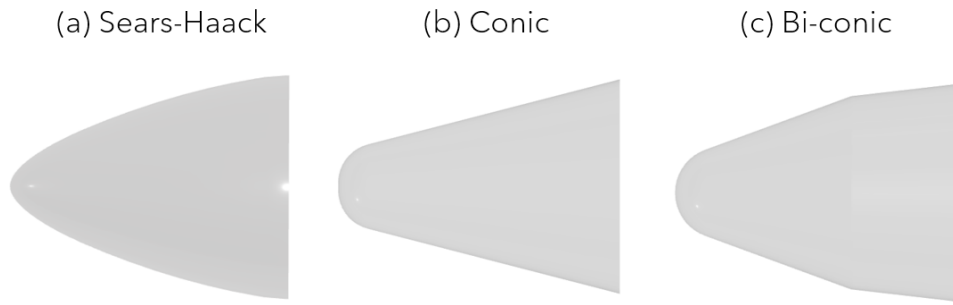


**Figure 3.7:** Representation of the three nose geometries modelled to be manufactured and tested along the project: a) Sears-Haack, b) Conic and c) Bi-conic. All the shapes have been spherically blunted for an improved aerodynamic performance.

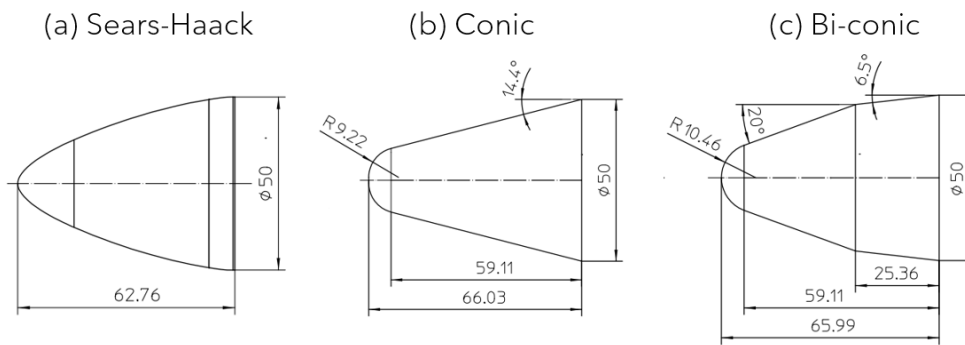


**Figure 3.8:** Drawings with dimensions (in mm) of the three nose geometries modelled to be manufactured and tested along the project: a) Sears-Haack, b) Conic and c) Bi-conic. All the shapes have been spherically blunted for an improved aerodynamic performance.

Regarding the boat-tail area, cylindrical two-piece elements were manufactured to be installed around the cylinder of diameter  $d$  (31.25 mm) to maintain the constant ratio  $D/d$ . The boat-tail angles of 5, 15 and 34 degrees were chosen based on the observed phenomena for different ranges of boat-tail angles (see ???: below  $5^\circ$ , the shock is weak; beyond  $30^\circ$ , a wake-like separated flow over a long zone occurs; and between 5 and  $30^\circ$ , the shock incidence on the boat-tail is strong, resulting in high loads [4].

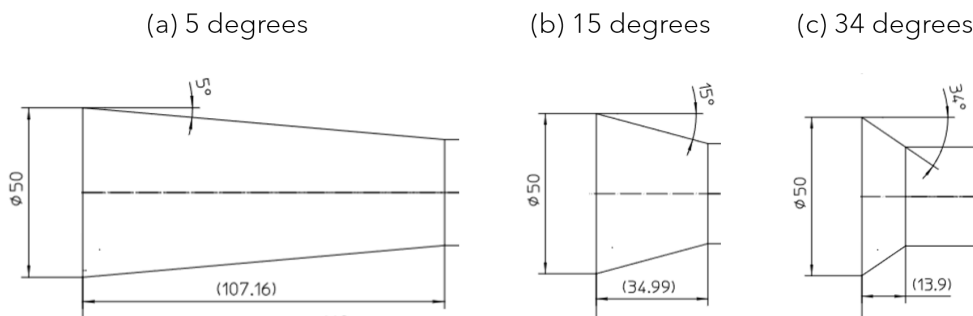


**Figure 3.9:** Drawings with dimensions (in mm) of the three boat-tail angle geometries modelled to be manufactured and tested along the project: a) 5 degrees, b) 15 degrees and c) 34 degrees.

The drawings for all the elements manufactured, which are three noses, three boat-tail sections, the cylindrical flange and the sting, are attached in Appendix A.

In order to simulate a full Reynolds number condition, incorporating artificial roughness strips into the model can expedite the transition from a laminar to a turbulent boundary layer. As stated by Goin and Pope [59], the most commonly favoured positions, which closely resemble the actual transition location, are approximately 5 per cent of the model length from the nose of the fuselage. Remarkably, this aligns with the BL transition wedges observed by Garbeff et al. [57] (see Figure 3.10) in the hammerhead configuration benchmark model, obtained by using the bi-conic nose and the 34° boat-tail. Figure 3.11 shows an example of the 1 mm transition strips of carborundum particles made for this thesis and located at 20% of the nose length (approximately equal to 5% of the whole model length) of the three geometries tested (bi-conic, conic and ogive, see Figure 3.6).

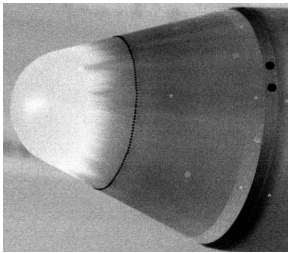


**Figure 3.10:** Infrared image depicting boundary layer transition wedges in the Model 11 benchmark model. [57]

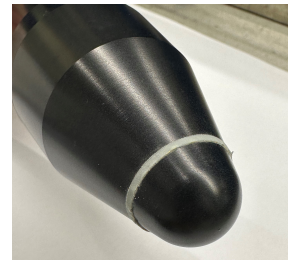


**Figure 3.11:** Detail photo of the transition strip located at 20% nose length from the model's leading edge.

The effect that the transition strip has on the flow was further assessed by performing an oil flow visualisation wind tunnel run at Mach 0.7, for a zero angle of attack and the benchmark model configuration (bi-conic nose and 34° boat-tail) with and without the transition strip (see Figure 3.12). From the images is clear that the oil cumulation due the transition from the spherical bluntness to the first conical section is maintained, as also the patterns due the shock wave at the transition between conical sections, or due the shear layer detachment at the boat-tail region. Moreover, the reattachment location is also around the same area. The main difference is found just after the transition strip location, as the patterns in the case with strip differ from the ones where transition is not forced.

### 3.3. Flow Conditions

The wind tunnel's aerodynamic experimental parameters are primarily determined by three factors: the Mach number within the test section, and the total pressure and temperature within the reservoir. The wind tunnel operator has control over the total pressure, while the Mach number within the test section is derived from static and total pressures. Additionally, the total temperature is measured prior to conducting the experiment. If the flow conditions at the wind tunnel reservoir are known, the flow conditions within the test section can be determined by assuming isentropic relations [55]. Specifically, the wind tunnel static conditions can be calculated using the total pressure and temperature values:

$$T_{\infty} = T_0 \left( 1 + \frac{\gamma - 1}{2} Ma_{\infty}^2 \right)^{-1} \quad (3.1)$$

$$p_{\infty} = p_0 \left( 1 + \frac{\gamma - 1}{2} Ma_{\infty}^2 \right)^{\frac{-\gamma}{\gamma - 1}} \quad (3.2)$$

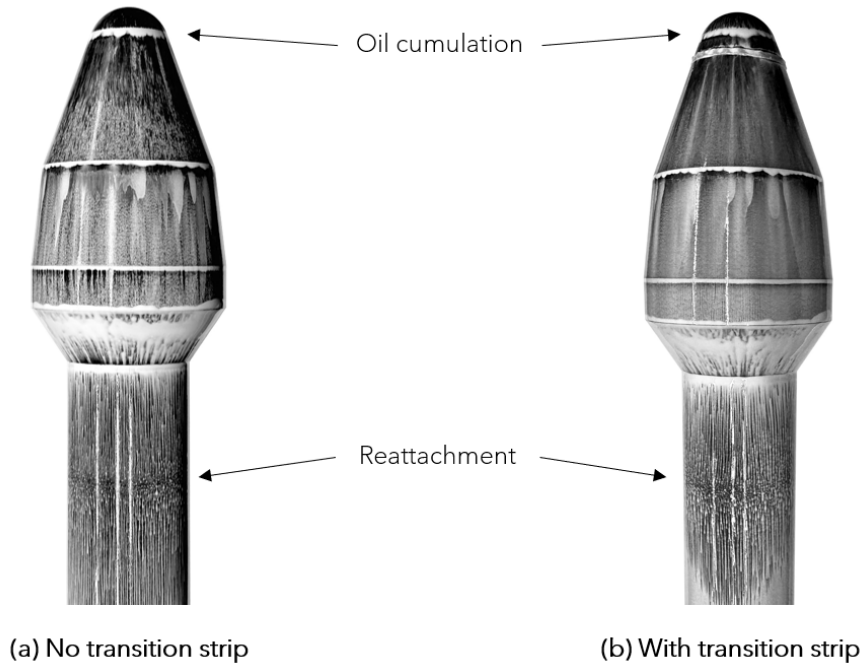


**Figure 3.12:** Oil flow patterns for the benchmark model configuration at Mach number of 0.7 and zero degree angle of attack with and without transition strip.

with  $\gamma = 1.4$ ,  $T_0$  the total temperature, and  $p_0$  the total pressure. From those values, the test section density can be calculated assuming a calorically perfect and ideal gas as

$$\rho_\infty = \frac{p_\infty}{RT_\infty} \quad (3.3)$$

with  $R = 287.057 \text{ J/kg} \cdot \text{K}$ . The flow velocity is derived from the Mach number:

$$U_\infty = Ma_\infty \sqrt{\gamma RT_\infty} \quad (3.4)$$

The dynamic viscosity is calculated using the Sutherland's law of viscosity:

$$\mu_\infty = \mu_{ref} \left( \frac{T_\infty}{T_{ref}} \right)^{3/2} \left( \frac{T_{ref} + S}{T_\infty + S} \right) \quad (3.5)$$

where  $\mu_{ref} = 1.7616 \cdot 10^{-5} \frac{\text{kg}}{\text{m} \cdot \text{s}}$ ,  $T_{ref} = 273 \text{ K}$  and  $S = 111 \text{ K}$ . Having the dynamic viscosity, density and flow velocity, the Reynolds number per unit of length can be evaluated:

$$\frac{Re_\infty}{L} = \frac{U_\infty \rho_\infty}{\mu_\infty} \quad (3.6)$$

For this case, the biggest diameter  $D = 50 \text{ mm}$  is taken as the unit length  $L$ , and total temperature  $T_0 = 288 \text{ K}$  and total pressure  $p_0 = 2 \text{ bar}$  are assumed. Tables 3.1 and 3.2 present the flow conditions parameters for runs with Mach numbers of 0.7 and 0.8, respectively.

The presence of a model in the wind tunnel test section introduces blockage effects that alter the freestream Mach number. These effects arise from both solid blockage caused by the physical obstruction of the model and wake blockage resulting from the interaction between the model and the surrounding flow. Solid blockage refers to the reduction of air passage space due to the model's insertion, causing an increase in flow velocity near the model and a decrease in available space for airflow. The size of the wake, extending several diameters

**Table 3.1:** Flow conditions for  $Ma_\infty = 0.7$ , total temperature of 288 K, and total pressure of 2 bar.

Parameter	Symbol	Value	Unit
Static temperature	$T_\infty$	257.74	[K]
Static pressure	$p_\infty$	1.44	[bar]
Density	$\rho_\infty$	1.95	[kg/m <sup>3</sup> ]
Dynamic viscosity	$\mu_\infty$	$1.71 \cdot 10^{-5}$	[kg/m · s]
Freestream velocity	$U_\infty$	227.27	[m/s]
Reynolds number	$Re$	$1.28 \cdot 10^6$	[-]

**Table 3.2:** Flow conditions for  $Ma_\infty = 0.8$ , total temperature of 288 K, and total pressure of 2 bar.

Parameter	Symbol	Value	Unit
Static temperature	$T_\infty$	255.32	[K]
Static pressure	$p_\infty$	1.31	[bar]
Density	$\rho_\infty$	1.79	[kg/m <sup>3</sup> ]
Dynamic viscosity	$\mu_\infty$	$1.67 \cdot 10^{-5}$	[kg/m · s]
Freestream velocity	$U_\infty$	256.26	[m/s]
Reynolds number	$Re$	$1.37 \cdot 10^6$	[-]

behind the model, is directly related to the resistance encountered by the model against the airflow and the energy extracted from the air stream [60]. By understanding and quantifying these blockage effects, a more accurate representation of the flow conditions in the wind tunnel can be achieved.

The blockage ratio,  $B_r$ , is defined as the ratio between the projection surface of the model,  $A_m$ , and the cross-sectional area of the test section perpendicular to the airflow direction,  $A_{test}$ . The model has a shape approximable as a cylinder, from which the section can be derived considering its maximum diameter is 50 mm (see section 3.2). On the other hand, as stated in section 3.1, the test section is rectangular, 0.255 m in height and 0.280 m in width. Such values give a blockage ratio of:

$$B_r = \frac{A_m}{A_{test}} = \frac{\pi \cdot 0.025^2}{0.255 \cdot 0.280} \approx 0.0275 = 2.75\% \quad (3.7)$$

However, it is important to note that such a minor blockage is primarily observed when the model is at zero angle of attack. As the angle of attack increases to 4 degrees, the blockage experienced undoubtedly intensifies. Additionally, the presence of the support used to position the model in the test section and the laser probe introduce additional blockage that was not considered in the previous approximation.

When assessing the findings of this study, it is essential to consider the potential influence of blockage. Previous research on hammerhead PLFs, such as the studies conducted in the 11-by-11 ft Transonic Wind Tunnel of NASA Ames Research Center by Garbeff et al. [57] and Panda [39], employed test sections with slotted walls. These slotted walls provided an additional pathway for fluid or airflow to bypass the solid blockage, ensuring a more uniform flow distribution and minimizing disruptions caused by solid obstructions.

In contrast, the TST-27 slotted walls were not employed in this study due to the limitations imposed by their double mirror system, which restricts the use of flow measurement techniques like PIV or Schlieren. Therefore, it is important to consider the difference that blockage introduces when interpreting the outcomes of this study. The absence of slotted walls in the experimental setup may affect the flow characteristics and lead to variations in the observed results compared to studies that incorporated slotted walls.

### 3.4. Experimental Campaigns

This study aims to investigate several variables and parameters, such as the airflow speed and angle of attack around the model, and assess the impact of different nose geometries and boat-tail angles on overall performance at the transonic regime.

Experimental aerodynamics is a complex and rapidly evolving field that requires sophisticated techniques for the visualisation and measurement of flow. Accurate and reliable measurement techniques are important in the transonic regime, where shock waves, boundary layers, and other nonlinear effects can drastically alter flow behaviour.

Based on the available instrumentation at TU Delft facilities and the techniques commonly employed in the literature, a focus on optical measurement techniques has been made. These techniques are preferable in research studies investigating the flow phenomena around a body due to their minimally intrusive nature. As such, they offer significant advantages over other techniques, which can affect flow characteristics and introduce measurement errors.

To that purpose, different experimental campaigns using oil flow visualisation, Schlieren imaging, and PIV have been performed. The Schlieren and oil flow visualisation techniques were employed for most model configurations due to their accessibility and convenience in instrumentation. The oil flow visualisation system allows for the visualisation of flow streamlines and surface flow patterns around the hammerhead PLF, enabling the identification of key characteristics such as separation and reattachment locations or turbulent regions. Schlieren, on the other hand, provides a more detailed depiction of flow behaviour in the vicinity of the nose and boat-tail areas, offering insights into the effectiveness of these features in influencing the flow. By conducting tests using a scaled model based on the geometry used by Coe and Nute [34] and Panda [39], the Schlieren results could be compared, thus providing validation.

Additionally, spectral analysis from the Schlieren images was done in different regions of flow field unsteadiness to derive aspects such as the frequencies of the shock-wave oscillations. Combining the results from both techniques, the most interesting configurations for further analysis using PIV and the required field of view were discerned.

The PIV system enabled the measurement of the airflow's velocity and turbulence, allowing further assessment of the geometry configurations which induce more or less unsteadiness, a relevant factor for the industry and the purpose of this research: assessing the effects of different nose and boat-tail combinations. Moreover, as wake reattachment cannot be observed from the Schlieren images, PIV allows that the phenomena can be further studied.

Tests were performed at 0 and 4° angle of attack as launch vehicles incline during ascent, and that disrupts their symmetry. Previous research around hammerhead configurations conducted by Garbeff et al. [57] and Panda et al. [39] influenced the choice of these angles so that their data can be used for comparison and validation. Additionally, both angles fall within the range of -6 to +6 degrees, which is commonly used to evaluate launcher loads [4].

Furthermore, considering the Mach number range of 0.6-1.2 explored in previous studies and the operational capabilities of the wind tunnel used in the experiments, Mach numbers between 0.6 and 0.8 have been studied.

The full test matrices of all wind tunnel campaigns performed can be found in Appendix B.

#### 3.4.1. Oil Flow Visualisation

Oil flow visualisation is a simple and effective technique that provides a preliminary qualitative understanding of flow patterns around a body. This technique can reveal several features of the flow, such as surface streamlines, separation lines, shock wave prints, reattachment lines, and vortices, providing valuable insights into the airflow behaviour and areas of flow separation around the body.

The operating principle relies on the oil properties, such as its high viscosity and low velocity near the model's surface, which generate low Reynolds numbers. This value indicates that the motion of the thin oil layer is dominated by the friction forces exerted by the air flowing around the upper surface of the model. Meanwhile, the advective inertia forces can be neglected, which results in what is known as a creeping flow. The velocity profile of the thin layer of oil is roughly linear, and the no-slip condition at the interface between the oil and air ensures that the velocities of both fluids are equal (see Figure 3.13). Thus, the oil's motion provides information about the flow's direction in the surface's proximity [55, 50].

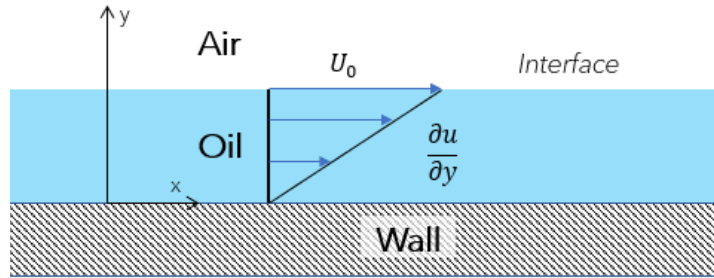


**Figure 3.13:** Air-oil layer interface representation together with the velocity gradient present in the oil.

To apply this technique, a thin homogeneous layer of oil is applied to the surface of the model under study, which is then placed in the wind tunnel. After the experiment, the oil flow patterns on the model surface can be observed and analyzed to gain insights into the airflow behaviour.

This technique has been employed in the present study to obtain preliminary insights into the flow patterns around the model under various configurations while also confirming and validating the observed phenomena using Schlieren and Particle Image Velocimetry techniques. Notably, certain phenomena, such as reattachment, are not discernible through Schlieren. Using oil flow visualisation allowed to determine the region where reattachment occurs so that the field of view on PIV included it.

#### Campaign Setup

The wind tunnel runs were recorded using a Nikon D7500 camera with a 20.9 Megapixel CMOS Sensor and a 4.2  $\mu\text{m}$  pixel size, also used to photograph the obtained flow patterns. The camera was set on top of a tripod in front of one of the two wind tunnel mirrors so that it had a complete view of the test section to record how the oil flowed along the run correctly. An external light system was used to illuminate the test section view, as shown in Figure 3.14. Table 3.3 compiles all the configurations tested through the oil flow visualisation technique (further details of the specific runs performed can be found in Table B.1).

**Table 3.3:** Oil flow test matrix.

Nose	Boat-tail [deg]	Mach	AoA [deg]
Bi-conic	34	0.7, 0.8	0; 4
Conic	34	0.8	0
Sears-Haack	34	0.8	0

The control system of the wind tunnel induces variations in the set Mach number. Specifically, the average Mach number for runs conducted at 0.7 exhibited values around  $0.7 \pm 0.05$ ,



**Figure 3.14:** TST-27 wind tunnel with the tripod and external light system used to record the oil flow runs.

accompanied by standard deviations of up to  $\pm 0.007$ . In contrast, runs conducted at 0.8 displayed increased instability, with an average Mach number around  $0.8 \pm 0.05$  and standard deviations of up to  $\pm 0.01$ .

### 3.4.2. Schlieren Visualisation

The Schlieren technique is a quantitative flow visualisation method which uses an optical system to observe density gradients in the airflow. These air density changes occur due to variations in pressure and temperature, which produce visible distortions in the image, allowing the visualization of flow separation and other phenomena such as shock or pressure waves [61].

The Schlieren technique was first described by Toepler<sup>2</sup>. Objective lenses were initially used as Schlieren heads, but mirror-based systems quickly became the preferred option due to their lower cost and wider field of view. The most commonly used mirror-based configuration is the “Z-type”, which employs two curved mirrors arranged in a Z-shape on opposite sides of the test section. As shown in Figure 3.15, the light passes through a set of lenses and a slit to ensure a parallel circular beam of radius  $a$  travels to the parabolic mirror. The ray is then refracted and crosses the test section, where the model is illuminated, before reaching the second parabolic mirror. This mirror reflects the light to another set of lenses and crosses a knife-edge (perpendicular to the light rays) before arriving at the camera. The knife-edge blocks part of the beam, only allowing a portion to pass through ( $\bar{a} < a$ ). Small changes in the refractive index of the air in the test section cause the outer parts of the beam to deflect, producing a shadowgraph image on the viewing screen.

<sup>2</sup>**Toepler:** Although not the inventor, Toepler described the basis of the Schlieren technique.

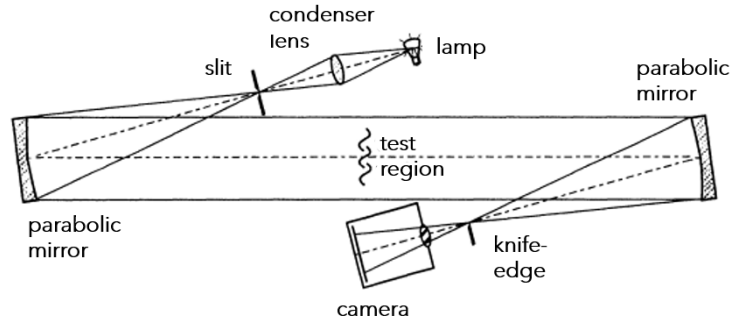


**Figure 3.15:** Schlieren visualization arrangement in z-type configuration. [61]

Z-type configurations are more precise than conventional Schlieren systems as from the off-axis aberrations induced (coma<sup>3</sup> and astigmatism<sup>4</sup>), allowing to suppress coma effects by tilting both mirrors at equal  $\theta$  angles in opposite directions from the central optical axis (using identical mirrors and ensuring that all optical elements are centered in a common plane). On the other hand, they can be more complex to set up and align, and the test section may need to be longer to avoid interference from the mirrors [61].

Removing the knife-edge while maintaining the rest of the set-up leads to the shadowgraphy technique. Unlike Schlieren, which assesses first-order derivatives of density fields, this method captures second-order derivatives. In a uniform test section without density variations, the recording plane is uniformly illuminated with intensity diminishing as  $\bar{a}$  decreases. Conversely, in the presence of density gradients within the test section, light rays refract by an angle  $\epsilon$ , causing them to shift from undisturbed positions at the knife-edge. This displacement introduces a change in the transmitted beam area,  $\Delta a$ , described by the equation:

$$\Delta a = f \tan(\epsilon_y) \quad (3.8)$$

Here,  $f$  signifies the focal length of the schlieren head, and it is assumed that the knife-edge is aligned with the x-direction (“horizontal knife-edge”). This orientation makes the schlieren system responsive to light-ray deviations in the y-direction. The beam shift,  $\Delta a$ , correlates with the alteration in intensity at the recording plane:

$$\frac{\Delta I}{I} = \frac{\Delta a}{\bar{a}} = \frac{f}{\bar{a}} \tan(\epsilon_y) \quad (3.9)$$

The deflection angle,  $\epsilon$ , can further be linked to variations in the refractive index within the test section:

$$\frac{\Delta I(x, y)}{I} = \frac{f}{\bar{a}} \int_{z_1}^{z_2} \frac{1}{n} \frac{\partial n}{\partial y} dz \quad (3.10)$$

Here,  $n$  represents the refractive index, defined as the ratio of the velocity of light in vacuum,  $c$ , to the velocity of light in the medium,  $c_v$ . Given the approximate value  $n \approx 1$ , the equation becomes:

<sup>3</sup>**Coma:** optical aberration that occurs in some optical systems where the shape of the mirror or lens deviates from a perfect paraboloid. This causes light rays that pass through different parts of the mirror to converge at different points, resulting in a distorted, elongated, or comet-shaped image of point sources.

<sup>4</sup>**Astigmatism:** optical aberration that occurs in lenses when the curvature of the lens surface varies in different planes. This causes light rays entering the lens in the sagittal plane to be focused at a different point than light rays entering in the tangential plane. As a result, instead of a single point, the image is focused into a line, causing distortion and blurring in one direction.

$$\frac{\Delta I(x, y)}{I} = \frac{f \cdot k}{\bar{a}} \int_{z_1}^{z_2} \frac{\partial \rho}{\partial y} dz \quad (3.11)$$

Consequently, the detectable ratio  $\frac{\Delta I(x, y)}{I}$  is contingent upon the ratio  $\frac{f}{\bar{a}}$ . Typically, the value of  $f$  is predetermined for a specific wind tunnel, while the system's sensitivity can be heightened by diminishing  $\bar{a}$ . It is crucial, however, to ensure that the reduction in  $\bar{a}$  avoids inducing either increased diffraction or decreased mean signal amplitude [50].

The utilisation of Schlieren imaging in this research facilitated the acquisition of instantaneous snapshots of the flow field. This enabled the analysis of shock wave oscillations and a thorough investigation of other phenomena such as expansion waves, detachment of shear layers, and recirculation (see section 2.1). Additionally, the fluctuating characteristics of the flow field were assessable by calculating both the mean and standard deviation of the instantaneous image sequence. For each run, a total of 5457 images were acquired. The relative simplicity and reduced cost associated with this technique, as compared to PIV, enabled its usage across various configurations. Consequently, it allowed for the general elucidation of the influences of Mach number, angle of attack, nose shape, and boat-tail geometry on the flow characteristics, thereby identifying distinctive dissimilarities between the different configurations.

#### Exposure time

When performing Schlieren visualisation, the optimal exposure time depends on the specific experimental setup, the light source's intensity, and the camera's sensitivity.

Longer exposure times of several microseconds to milliseconds may be suitable to obtain mean photographs, as more photons are captured, giving better signal-to-noise ratios. However, such long exposure times may also result in motion blur or image smearing if the flow is unsteady or the camera or flow field is in motion.

To obtain instantaneous photographs, shorter exposure times of a few nanoseconds to microseconds may be more appropriate, as these can freeze the motion of the flow and provide sharp images of the flow features.

In conclusion, preliminary tests with different exposure times must be taken to find the optimal settings for the specific experimental conditions and ensure high-quality images. A range of exposure times from 1 to 1000 microseconds may be appropriate for transonic Schlieren visualization. However, the optimal exposure time should be determined experimentally for the specific setup and flow conditions.

#### Knife-Edge Orientation

The orientation of the knife-edge is a crucial factor that influences the sensitivity and resolution of the Schlieren technique. Typically, two main orientations are used: horizontal and vertical knife-edges.

In a vertical knife-edge configuration, the knife-edge is placed perpendicular to the optical axis of the Schlieren system. The knife-edge affects only the ray refractions with orthogonal components to it. Thus, this orientation only allows the detection of the horizontal gradients,  $\partial n / \partial x$ . Refractions parallel to the edge, due to  $\partial n / \partial y$ , do not result in a change in cutoff or screen illuminance, causing a flow with purely vertical gradients to remain invisible, even with the presence of the knife-edge. How light rays refract depending on the type of density field encountered can be further understood with Figure 3.16.

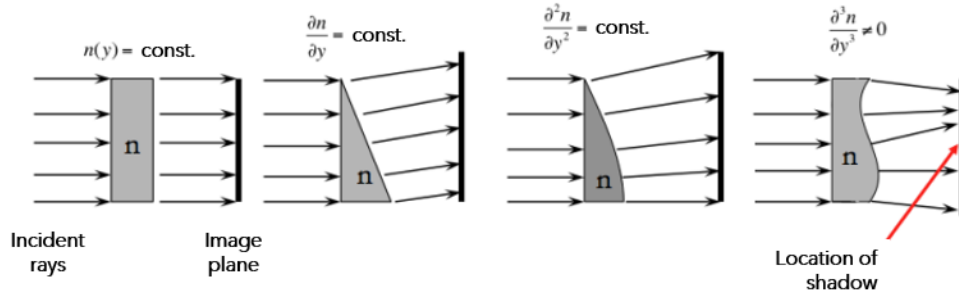


**Figure 3.16:** Schematic showing the refraction of light rays by density fields with density and its first, second, and third derivatives constant. The two-dimensional description is easily extended to three dimensions. [62]

To address this issue, some researchers suggest using two Schlieren images, one with a horizontal and another with a vertical knife-edge, to capture the Schlieren object fully. This approach ensures that all refractive components of the flow field are captured, providing a complete representation of the flow characteristics [61].

In addition to the vertical and horizontal knife-edge orientations, there are also oblique knife-edge orientations. An oblique knife-edge is positioned at an angle to the optical axis of the Schlieren system and can be used to observe flows with oblique shock waves or at an angle to the optical axis. The oblique knife-edge can be rotated to different angles to optimise the visualisation of the specific flow feature of interest. However, the oblique knife-edge set-up can be more complex and require careful alignment and calibration.

The choice of knife-edge orientation depends on the specific experimental setup and the flow feature of interest. Therefore, the best practice is to perform a few preliminary tests with different knife-edge orientations, including oblique, to find the optimal set-up for the specific experimental conditions.

### Campaign Setup

A high-frequency Schlieren campaign at 5 kHz has been performed using Photron FASTCAM SA1.1. The sampling frequency used in this study was selected considering the Nyquist sampling criterion, which states that for a signal sampled at a rate of  $SR$ , the maximum resolvable frequency,  $f_{max}$ , can be determined as:

$$f_{max} = \frac{SR}{2} \quad (3.12)$$

To accurately reproduce the signal and prevent aliasing, the sampling rate must be at least twice the maximum frequency needed to be resolved, denoted as  $f_{max}$ . Therefore, when the sampling rate is set to 5 kHz, the maximum resolvable frequency is 2.5 kHz.

Choosing 5 kHz (with full active sensor size) allows for the resolution of the shock-wave position over time, phenomena required to be studied at most configurations so that the research questions around the shock-wave behaviour could be answered. A  $49.02 \mu s$  exposure time was set for this Schlieren campaign. Moreover, a 300 mm lens was used, and the knife-edge was set at a horizontal orientation with 50% obstruction (a summary of all the configuration parameters is provided in Table 3.4a). All configurations tested in that campaign are compiled in Table 3.4b (further details of the specific runs can be found in Table B.2).

The average Mach number obtained by the wind tunnel control program for runs conducted at 0.7 exhibited values around  $0.7 \pm 0.032$ , accompanied by standard deviations of up to  $\pm 0.002$ . As for the runs at Mach 0.8, the average was of  $0.8 \pm 0.03$  and the standard deviation went up to  $\pm 0.008$ .

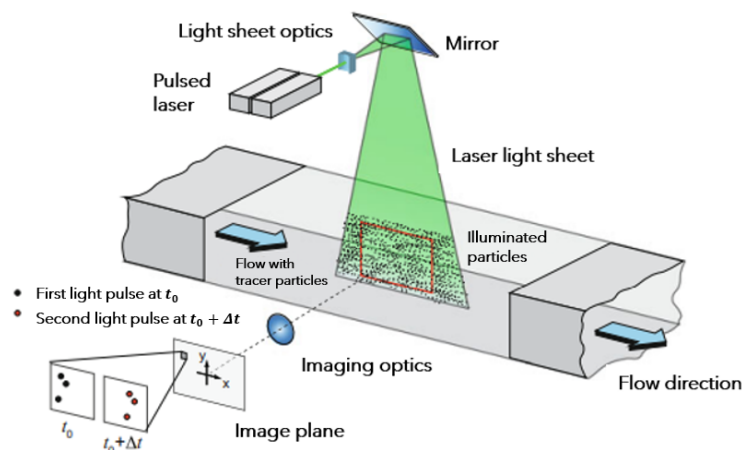
**Table 3.4:** Schlieren campaign measurement parameters and tested configurations

(a) Configuration parameters			(b) Tested configurations			
Parameter	Value	Unit	Nose	BT [deg]	Mach	AoA [deg]
KE Orientation	Horiz.	-	Bi-conic	34	0.6, 0.7, 0.8	0; 4
KE Obstruction	50	[%]		5, 15	0.7, 0.8	0; 4
Exposure Time	49.02	[ $\mu s$ ]	Conic	34	0.7, 0.8	0; 4
Acq. Frequency	5	[kHz]	Ogive	5, 34	0.7, 0.8	0
Lens	300	[mm]		34	0.7, 0.8	4
Number Samples	5457	[-]				

### 3.4.3. Particle Image Velocimetry

Particle Image Velocimetry, known as PIV, is a widely-used, non-intrusive flow measurement technique that allows the evaluation of the velocity field on a plane (with Planar or Stereo PIV) or in a volume (Tomo PIV). PIV employs cameras and advanced algorithms to track the motion of particles within the flow and reconstruct a detailed picture of its velocity field. Unlike other techniques, such as pressure probes or Hot Wire Anemometry (HWA), no probes are inserted into the test section, making PIV particularly useful in high-speed conditions where closed wind tunnels with limited accessibility are commonly employed. Additionally, PIV offers relatively high spatial resolution, limited by the camera's resolution and the optical access of the wind tunnel. A higher spatial resolution can be achieved using a low-speed acquisition (low temporal resolution) PIV system, which is particularly relevant for flow visualization studies in transonic regimes [50, 63].

The experimental set-up for PIV typically involves a laser, a camera, and a seeding system that injects small tracer particles into the flow (Figure 3.17 shows the typical set-up for a 2D PIV within the flow field in a plane in a wind tunnel). The laser beam is expanded and directed into the flow, illuminating a small region of interest filled with tracer particles, which movement is captured by the camera. The seeding system must be carefully designed to ensure the particles are small enough to follow the flow but large enough to be easily imaged. Furthermore, it is crucial to properly regulate the seeding density to avoid particle overlap, which can introduce errors and complicate the subsequent analysis of the obtained data.

**Figure 3.17:** Experimental arrangement for planar 2C-2D PIV in a wind tunnel. [63]

The particles scatter the laser light, illuminating the plane of interest within the flow twice. The time delay between pulses is selected based on the flow velocity and the magnification

at imaging, assuming that the tracer particles move at a velocity representative of the local flow velocity between illuminations. A camera captures images of the light scattered by the particles. The two successive images are cross-correlated to determine the displacement of particles between the two snapshots, which is subsequently used to calculate the velocity and direction of the airflow. The results can be visualized as vector fields, which comprehensively represent the flow pattern [63].

As discussed in section 2.3, the author has not found any application of this technique in hammerhead PLFs aerodynamics studies. Therefore, using PIV in this research is a noteworthy innovation, despite its well-established reputation as a valuable and effective technique for obtaining comprehensive, quantitative measurements of flow fields in the transonic regime. The application of Particle Image Velocimetry has allowed to validate the flow phenomena already observed with oil flow and Schlieren techniques. Moreover, PIV has provided detailed insights into the average velocity fields and the precise location of reattachment. This was accomplished by employing a low-speed acquisition PIV system characterized by enhanced spatial resolution at the expense of temporal resolution.

### Campaign Setup

Planar PIV was selected for the campaign, as a  $y$ -symmetrical model was used, and all phenomena to study occur in a plane. To improve resolution and obtain a larger field of view, three cameras were located in a zig-zag (two on one side and another on the other) of the two windows that provide an idea of the wind tunnel test section (see a diagram of the set-up in Figure 3.18 and a photograph of two of the cameras used in Figure 3.21a). The set-up was completed by the laser, acting as the illumination system, the seeding generator, and the PTU (Programmable Time Unit), which allows the synchronisation and control between the laser and cameras.

In the cases where a zero angle of attack was applied, all three cameras were positioned at the same height. However, in the 4-degree cases, it was necessary to introduce a height difference between the cameras on the same side. This adjustment was required to maintain visibility within the previously established field of views, as depicted in Figure 3.23. The height difference between the cameras ensured that the desired perspectives and coverage were maintained for accurate data capture and analysis (the cameras at different heights can be observed at the background of Figure 3.19).

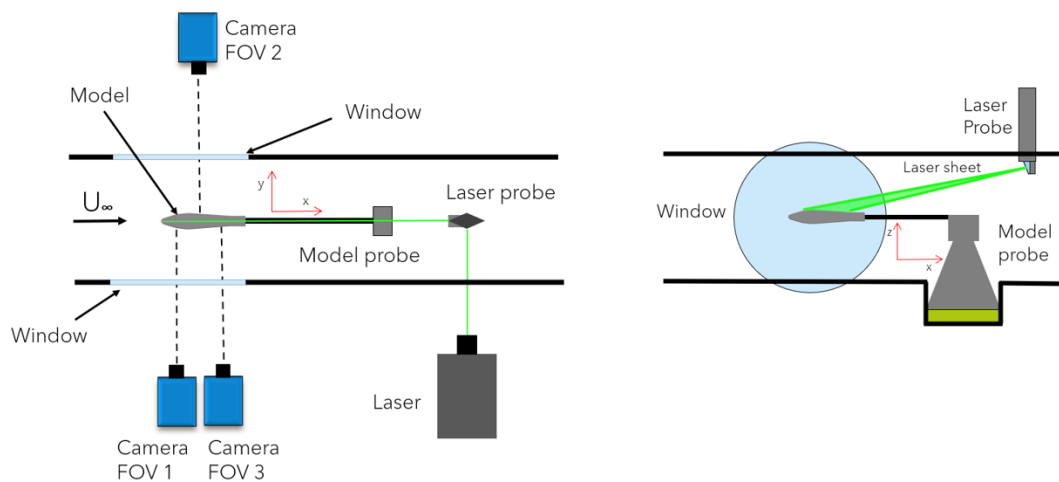


**Figure 3.18:** Diagram of the PIV set-up, with top (left) and lateral (right) views. The field of views (FOV) numbers refer to the areas designated in Figure 3.23.



**Figure 3.19:** PIV set-up featuring the benchmark Coe and Nute model positioned at 4 degrees. In the background, two cameras are positioned at different heights to ensure full coverage of the field of view.

Table 3.5b compiles the configurations tested during the campaign, focusing on assessing reattachment and other average field phenomena observed along and after the boat-tail. The complete test matrix, as shown in Table B.3 (included in Appendix B), outlines further details of each of the runs.

On average, 250 image pairs were acquired per test. Furthermore, each combination of configurations was tested twice to enhance reliability and consistency, as well as converged statistics.

**Table 3.5:** PIV campaign parameters and tested configurations

(a) Configuration parameters

Parameter	Value	Unit
Magnification factor	0.16	-
f-number, $f_{\#}$	3.9	-
Image pairs	250	-
FOV overlap	5	[mm]
Acq. frequency	5	[Hz]
Pulse time sep.	1.5	[ $\mu$ s]
Aperture	75	[mm]

(b) Tested configurations

Nose	BT [deg]	Mach	AoA [deg]
Bi-conic	34	0.7, 0.8	0; 4
	15	0.7, 0.8	0; 4

### Laser System

The laser system consists of a double-pulse Nd:YAG Spectra Physics Quanta Ray PIV-400 laser operated at a laser power of 400 mJ per pulse, with a pulse duration of 6 ns (allowing that the particle displacement during illumination is lower than 0.4 pixels and, thus, introducing a negligible particle blur) at wave-length of 532 nm, and a frequency of 10 Hz between double pulses. The light is conveyed by laser optics to form a laser sheet of about 1.5 mm thickness.

Considering the phenomena sought to study in this thesis, the measurement plane aligns with the streamwise-vertical plane. To introduce the laser sheet inside the wind tunnel (see the path that the laser needs to follow in Figure 3.21b), a laser probe is needed, which can be inserted downstream of the test section from either the upper or the side wall. In this thesis, the upper wall access point has been chosen, location which allows the laser light to impinge on top of the model (Figure 3.21c shows the inserted probe as seen inside the tunnel, downstream

the test section, and Figure 3.20 shows the illuminated test section as seen from one of the optical access windows). Schlieren tests were conducted using the installed laser probe to compare the resulting data to those obtained from the same configuration without the probe. The similarities with those allow to assume that the probe effect on the flow is negligible.

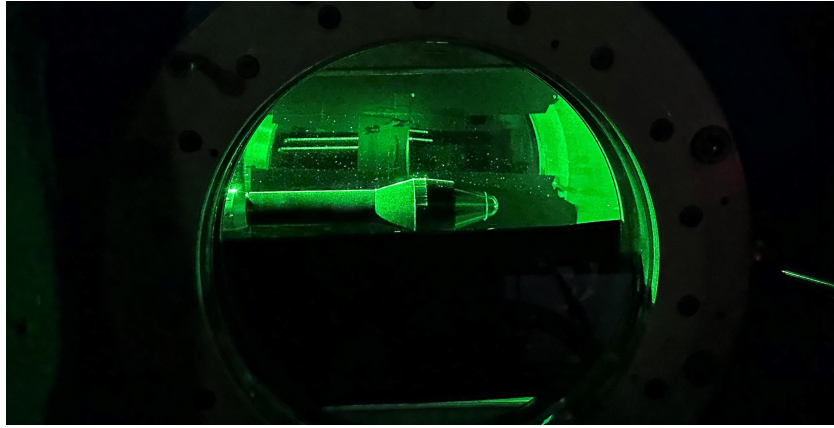
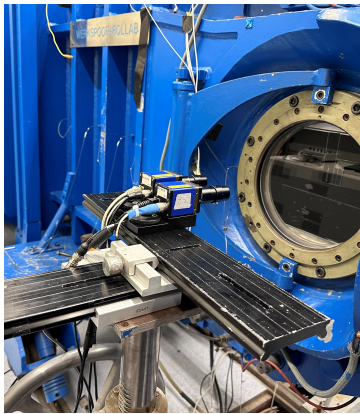
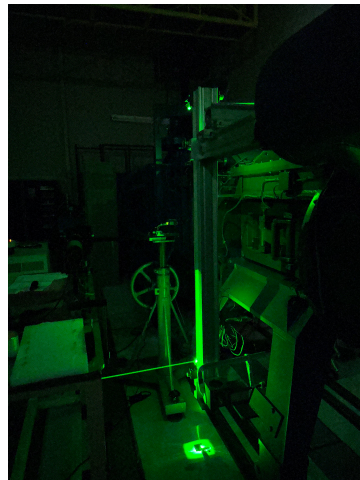


**Figure 3.20:** Illuminated test section as seen from one of the optical access windows.



**(a)** PIV set-up: two cameras on top of tripod to ensure view of the test section from one of the windows.



**(b)** Laser path towards the laser probe.



**(c)** Probe as seen from inside the TST-27 tunnel.

**Figure 3.21:** Illumination and imaging system.

The design of the laser probe was developed by F. J. Donker Duyvis [64] (Figure 3.22 illustrates its constituent components). Comprising a system of lenses and mirrors, the laser probe facilitates the creation and alignment of the laser sheet within the test section.

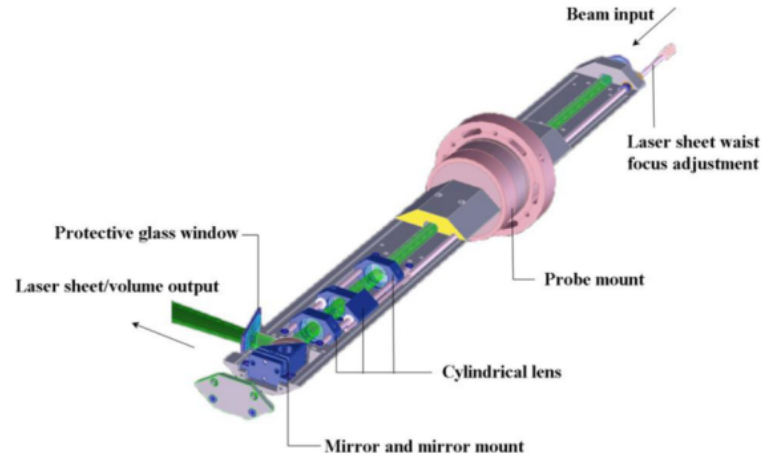


**Figure 3.22:** Laser probe 3D CAD with cut-outs to facilitate overall system view. [64]

### Imaging

An image of the tracer particles in the light sheet is formed using a lens on the surface of an image sensor. The selection of the objective lens to be used in the PIV experiments is based on different parameters that characterise the imaging system: the focal length  $f$ ; f-number (or f-stop)  $f_{\#} = f/D$  (being  $D$  the lens aperture diameter), and image magnification  $M$ . This last parameter is defined as the ratio of the image distance  $d_i$  (between image and lens) and object distance  $d_o$  (between object and lens), as described by the thin lens formula:

$$\frac{1}{f} = \frac{1}{d_i} + \frac{1}{d_o} \quad (3.13)$$

$$M = \frac{d_i}{d_o} \quad (3.14)$$

As a simple consequence of the system, the magnification factor can also be evaluated as the ratio between the image size (sensor size) and the imaged object size (called the Field Of View, or FOV).

$$M = \frac{\text{sensor size}}{FOV} = \frac{\text{pixel size} \cdot N_{\text{pixels}}}{w_{FOV}} \quad (3.15)$$

Observations from the oil flow and Schlieren campaigns informed the field of view selection for the PIV tests. Notably, most phenomena centred around the boat-tail area, particularly the detachment of the shear layer and the ensuing recirculation region. Consequently, it was imperative to encompass the entire boat-tail area within the field of view. Moving upstream from the boat-tail, the focus shifted towards capturing the shock waves. To achieve this, the upstreammost location was determined by identifying where the initial shock wave appeared in the Schlieren images, namely, at the shoulder of the bi-conic section. It is worth noting that due to the positioning of the laser sheet, regions even further upstream (the first conic section) were not expected to be illuminated, making this selection practical.

Regarding the termination of the field of view, a primary objective of the PIV campaign was to observe reattachment. This process had eluded observation using Schlieren. To ensure coverage of the reattachment, the locations derived from the oil flow images (see section 4.6) were considered. Establishing the most upstream shock-wave location and the furthest reattachment location, with an added margin of safety, led to a projected area of approximately 13 cm to be encompassed.

As previously noted, three cameras were available to cover this designated region, resulting in the three distinct FOVs depicted in Figure 3.23. Each FOV has average dimensions of 46x35 mm, with a 7 mm overlap between adjacent windows. This overlap facilitates the comprehensive representation of the entire field of view during post-processing, as demonstrated in Figure 3.24, which displays the obtained average modular velocity field for the benchmark case (bi-conic nose and 34-degree boat-tail) at Mach 0.7 and angle of attack 0 degrees (run 1 at Table B.3).

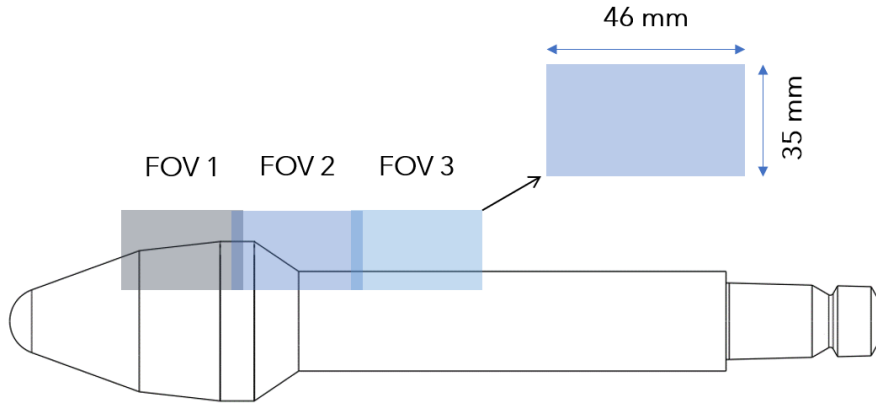


**Figure 3.23:** Fields of view (FOV) for the three cameras used at PIV.

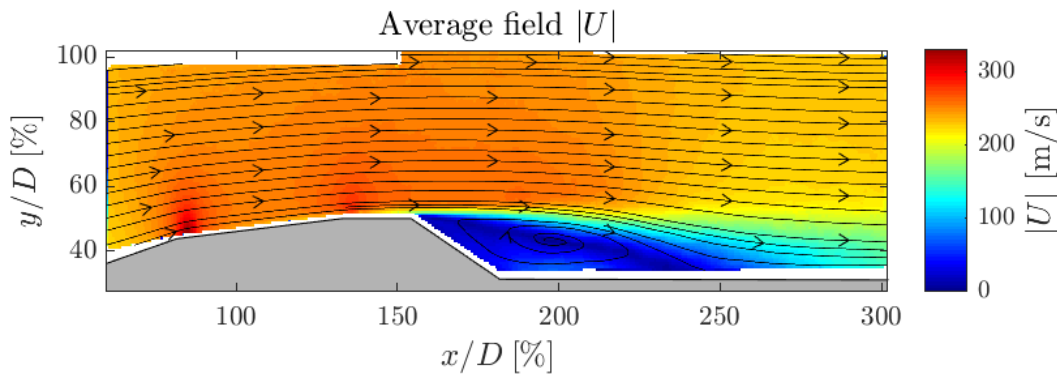


**Figure 3.24:** Average modular velocity field  $|U|$  with streamlines. Data extracted through PIV for benchmark case (Coe and Nute's model 11 [34]) composed by bi-conic nose and 34-degree boat-tail) at Mach 0.7 and angle of attack of 0 degrees (run 1 at Table B.3).

The three cameras used during the PIV campaign are the Bobcat IMPERX IGV-B1610 CCD with a resolution of  $1628 \times 1236$  pixels and  $4.40 \mu m$  pixel size. Their maximum recording rate is 8.3 Hz with a separation time between images of 120 ms. Considering such pixel size and that a total field of view of around 13 cm is covered (4.60 cm per camera), the magnification factor results in:

$$M = \frac{4.4 \cdot 10^{-6} \cdot 1628}{0.046} = 0.1592 \quad (3.16)$$

The  $f_{\#}$  (or f-number or f-stop) of a lens is the ratio between its focal length and the diameter of the aperture, determining the amount of light the lens allows in and the depth of field. The higher the  $f_{\#}$ , the more closed the aperture is, making the image darker while focusing on the

background (large depth of field). Particle images are in focus when the light sheet thickness,  $\Delta z_0$ , is smaller than the focal depth,  $\delta z$ , of the optical system, which gives the distance normal to the image plane in which a particle remains in focus (Equation (3.17)).

$$\delta z = 4.88 \cdot \lambda \cdot f_{\#}^2 \left( \frac{M+1}{M} \right)^2 \quad (3.17)$$

For this case, the focal depth had to be larger or equal than the laser sheet width, of around 1.5 mm. Considering that constraint, the magnification factor previously calculated, and a laser light wavelength,  $\lambda$ , of 532 nm, the f-number is:

$$f_{\#} \geq \sqrt{\frac{\delta z \cdot M^2}{4.88 \cdot \lambda \cdot (M+1)^2}} = 3.3 \quad (3.18)$$

Considering the previous result, the selected lens was a 75 mm aperture lens with a range of  $f_{\#}$  from 3.9 to 32, so that 3.9 could be selected for the tests. An overlap of around 7 mm between field of views was set when locating and focusing the cameras, to cover the field of views highlighted in Figure 3.23.

### Signal Synchronisation

A PTU (Programmable Timing Unit) is used to synchronise the camera and laser trigger signals through the LaVision DaVis 8.1 software (also used for the data post-processing). As the whole PIV campaign was conducted in double-frame mode, two parameters had to be selected: the repetition rate,  $f$ , which defines the frequency between double-pulses, and the laser pulse time separation,  $\Delta t$ . The timing diagram of the camera and laser is depicted in Figure 3.25.

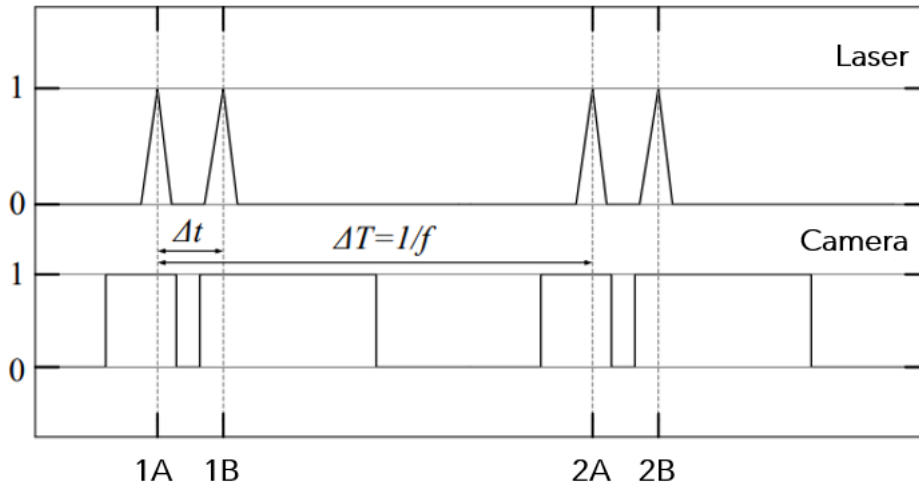


**Figure 3.25:** PIV timing diagram for double-pulse double-frame mode. [65]

The maximum repetition rate is determined by the hardware (camera and laser), resulting in a repetition rate of  $f = 5 \text{ Hz}$ .

As for the time separation  $\Delta t$  between laser pulses, a trade-off emerges. Opting for an excessively long  $\Delta t$  will result in a significant displacement of particles, potentially leading to the loss of correlation due to out-of-plane particle movement in planar measurements, as well as an increase in velocity shear. Conversely, it is not advisable to minimize particle displacement entirely. Practical considerations, such as cross-correlation uncertainty of approximately

0.1 pixel, dictate that a particle displacement of around 20 pixels is desirable. Achieving this optimal displacement requires a compromise between the time separation  $\Delta t$  and the magnification factor  $M$ , as the pixel displacement ( $px_{disp}$ ) can be calculated as a function of the field of view embraced by the cameras ( $fov_{cam}$ ), their own pixel field of view width ( $fov_{px}$ ), the maximum expected particle velocity to be traced ( $U$ ) and the time separation ( $\Delta t$ ):

$$px_{disp} = \frac{fov_{px}}{fov_{cam}} \cdot U \cdot \Delta t \quad (3.19)$$

Considering that the cameras embraced a field of view of approximately 4.6 cm each, while their pixel field of view width is 1628 pixels, and that a maximum velocity of 350 m/s can be expected from the particles when studying the flow at a Mach number of 0.8, the pixel displacement for the particles at a  $\Delta t$  of 1  $\mu s$  and 1.5  $\mu s$  is of 12 and 19 pixels, respectively. Such calculation confirms the adequacy of selecting a pulse separation of  $\Delta t = 1.5 \mu s$ .

### Seeding System

The seeding system consists of the seeding generator, the seeding rake or distributor, and the seeding particles. The seeding generator used for the experiments is the PIVTEC GMBH PIVPART 45 seeder, directly connected to the seeding rake. The latter is placed in the settling chamber of the wind tunnel and consists of several nozzles which eject particles in the stream tube. The seeding stream density can be varied remotely from the control room by selecting the number of active nozzles. In this study, all the 45 nozzles available have been used to achieve a sufficient seeding density during the measurements.

DEHS seeding particles (Di-Ethyl-Hexyl-Sebacat) with a median particle size of 1  $\mu m$  and a particle response time,  $\tau_p$ , of approximately 2  $\mu s$  have been employed [66].

## 3.5. Uncertainty Analysis

For result accuracy and consistency, the experiments were repeated multiple times. Moreover, the initial test involving oil flow and Schlieren visualisation (benchmark configuration with bi-conic nose and 34-degree boat-tail at 0 degrees angle of attack and Mach number 0.7) was redone at the end to confirm result reliability. An evaluation was conducted for the PIV testing, which relies on average fields for analysis, to determine the necessary number of samples for achieving low uncertainty. This assessment considered the following expressions for measuring uncertainty in the mean velocity,  $U$ , and standard deviation,  $\sigma$ :

$$\varepsilon_U = \frac{\sigma_U z_a/2}{U \sqrt{N}} \quad \varepsilon_\sigma = \frac{\sigma_U z_a/2}{U \sqrt{2 \cdot N}} \quad (3.20)$$

where  $\sigma_U/U$  represents the velocity standard deviation normalized by the mean velocity,  $z_a$  is a variable associated with the confidence level of the velocity's probability density function, and  $N$  denotes the number of samples. A turbulence intensity of 10% is assumed, along with a targeted uncertainty level of 1% (at a 95% confidence) and  $z_a$  equal to 2. Moreover, a Gaussian distribution is adopted, and the required confidence level ( $1 - \alpha_u$ ) is set to 0.95 (meaning that 95% of the observations meet the criterion that the measured velocity deviates by no more than  $\varepsilon_U$  from the true mean velocity  $U$ ).

From the expressions at Equation (3.20), the standard deviation gives the more stringent requirement, necessitating 200 samples [67]. However, to maintain reliable statistics, even if a portion of the photographs had to be disregarded (to comply with the requirement of 200 samples), the test quantity was typically doubled. For precise numbers of image pairs taken in each configuration, refer to Table B.3.

In addition to the statistical uncertainties that impact the mean and standard deviation, there exist supplementary sources of uncertainty regarding the individual velocity values. PIV

measurements in high-speed flows present the uncertainty due the finite time response of the seeding particles, remarkable particularly around shock waves. The difference between the particle velocity and the actual flow velocity, known as particle slip velocity, can be computed as described by Melling [68]:

$$\varepsilon_{slip} = \vec{U}_{slip} \approx \tau_p \cdot \vec{a}_p \quad (3.21)$$

where  $\tau_p$  is the particle response time, which for the DEHS particles used is approximately  $2\mu s$  (estimated by Ragni et al. [66]), and  $\vec{a}_p$  is the particle acceleration, which can be calculated as:

$$\vec{a}_p = \frac{du_p}{dt} = \frac{u_p - u_f}{\tau_p} = \vec{U} \cdot \nabla \vec{U} = \vec{U} \cdot \left( \frac{\partial u}{\partial x} + \frac{\partial v}{\partial y} \right) \quad (3.22)$$

Therefore,

$$\varepsilon_{slip} \approx \tau_p \cdot \vec{a}_p = \tau_p \cdot \vec{U} \cdot \left( \frac{\partial u}{\partial x} + \frac{\partial v}{\partial y} \right) \quad (3.23)$$

At the shock wave location the gradients are maximum, thus, the values will be the highest.

When post-processing the PIV images, the cross-correlation performed and the window size used induce uncertainty to the results. The cross-correlation procedure adds uncertainty to the individual velocity vectors [69]:

$$\varepsilon_{cc} = \frac{\varepsilon_{corr}}{M \delta t} \quad (3.24)$$

where  $M$  is the magnification factor,  $\delta t$  the laser pulse separation (see Table 3.5a), and  $\varepsilon_{corr}$  is the correlation uncertainty, which for planar PIV can be assumed is 0.1 pixel.

As for the window size, which determines the spatial resolution of the interrogation window used to obtain the velocity, Schrijer and Scarano [70] modelled the ratio between measured and real velocity,  $u/u_0$ , for a single step interrogation:

$$\varepsilon_{ws} = \frac{u}{u_0} = \text{sinc} \left( \frac{WS}{\lambda} \right) \quad (3.25)$$

where  $WS$  is the window size and  $\lambda$  the wave length of interest. This effect is decreased for multi-step correlation, as used in this study. In particular, when examining cases where the ratio of  $WS$  to  $\lambda$  is less than 0.5, and considering that typically the smallest resolvable scale in the flow has twice the size of the window, a value of  $\varepsilon_{WS} < 1\%$  is generally estimated [71, 50]

Schlieren data is also subject to uncertainties. Within this thesis, the primary focus of schlieren image analysis is evaluating oscillations in the position of shock waves over time, as the discussions around the pixel intensity standard deviation are qualitative. Consequently, it is crucial to recognise that the density gradients visualised in a schlieren image do not offer a cross-sectional perspective; instead, they represent an integration across the complete span of the airfoil.

Hence, when a shock wave does not align perpendicularly with the light propagation vector, the schlieren image depicts the shock wave based on its projected area. Consequently, the displayed shock appears thicker than its actual dimensions. This discrepancy can be quantified as half of the thickness of the projected shock image ( $t_{SW}$ ) while considering the negligible nature of the actual local shock wave thickness [50].

$$\varepsilon_{Sch} = \frac{t_{SW}}{2} \approx 1.5 \text{ mm} \quad (3.26)$$

Finally, it is important to consider that the wind tunnel operation and setup introduce inherent uncertainties. The precision of the model's angle of attack should be accounted for with a range of  $\pm 0.2^\circ$ , and the Mach number varied throughout the experimental runs, as discussed in section 3.4.

The maximum values for some of the uncertainties mentioned in this section are presented in Table 3.6. The highest error corresponds to the velocity particle slip since the relaxation time of the DEHS particles is considerably high. This maximum value (compiled in the table) corresponds to the particle slip in the shock region, being minor in the remaining field of view.

**Table 3.6:** Uncertainty values.

Uncertainty Source	Symbol	Value
Particle Slip	$\varepsilon_{slip}$	$\leq 62.65$ m/s
Cross-correlation	$\varepsilon_{cc}$	$\leq 1.83$ m/s
Window size	$\varepsilon_{ws}$	$\leq 1\%$
Line of sight effect	$\varepsilon_{Sch}$	$\leq 1.5$ mm

## 3.6. Data Analysis

In this section, the main pre- and post-processing performed with the results of both Schlieren and PIV is detailed.

### 3.6.1. Schlieren Images Processing

Schlieren provides a sequence of images from which a large amount of data can be extracted. For all runs performed, a previous run without the wind tunnel was done. Those images of the field of view without flow allow subtracting the non-uniformities present as a base from the pictures with flow. By subtracting from those a photo without flow, all that added "noise" can be removed.

Once the background had been subtracted, different post-processing was made. On the one hand, the standard deviation per pixel allowed to obtain images where the regions with the most instability along the time captured are distinguishable. The standard deviation was calculated as:

$$\sigma = \overline{u'} = \sqrt{u^2 - (\overline{u})^2} = \sqrt{\frac{\sum u^2}{N} - \left(\frac{\sum u}{N}\right)^2} \quad (3.27)$$

where  $u$  refers to the intensity in a specific pixel, and  $N$  to the number of images taken.

On the other hand, from the Schlieren images, both the shock wave location and its oscillatory behaviour can be studied.

The oscillatory behaviour of the shock wave was examined through spectral analysis, similar to what other authors such as d'Aguanno [50] have done. Starting with a time-domain signal, denoted as  $x(t)$ , its Fourier transform, represented as  $X(f)$ , is defined as:

$$X(f) = \int_{-\infty}^{\infty} (x_n \cdot e^{-i2\pi \cdot f \cdot t}) \cdot dt \quad (3.28)$$

Based on this precise definition, the Discrete Fourier Transform (DFT) can be derived when the signal is comprised of a finite number of samples,  $N$ :

$$X_k = \sum_{n=0}^{N-1} x_n \cdot e^{-\frac{i2\pi k n}{N}} \quad (3.29)$$

While the Fourier Transform is suitable for spectral analysis in the absence of noise or random effects, this is often not the case with experimental data. In such situations, it is preferable to compute the Power Spectral Density (PSD), which is obtained by squaring the amplitude rather than using the amplitude itself. The PSD provides information on how the power of a signal is distributed in the frequency domain. From a mathematical standpoint, the PSD can be obtained as the Fourier transform of the autocorrelation function:

$$P(f) = \sum_{n=-\infty}^{\infty} f(k) \cdot e^{-i2\pi k n} \quad (3.30)$$

where  $r(k)$  is defined as:

$$r(k) = E\{y(t)y * (t - k)\} = |Y(k)|^2 \quad (3.31)$$

Among the various methods available for computing the power spectral density, Welch's method has been chosen due to its ability to mitigate the impact of noise, despite a trade-off in frequency resolution. This approach involves dividing the initial signal into overlapping segments, with the overlap percentage typically ranging from 0 to 50%. Each segment is then windowed in the time domain, and a Fast Fourier Transform is performed on each of them. The squared amplitude of the resulting spectrum is computed, yielding a periodogram, denoted as  $P_j(f)$ , for each segment. By averaging these periodograms using Welch's method, the variance of individual power measurements can be significantly reduced. Specifically, when there are a total of  $L$  periodograms, the power spectral density according to Welch's method is obtained as follows:

$$P(f) = \frac{1}{L} \sum_{j=1}^L P_j(f) \quad (3.32)$$

Matlab's `pwelch` function is used to compute the PSD with its defaults settings of using 8 segments per unit length and an overlap between segments of 50%.

A comprehensive analysis can be conducted by selecting a pixel line at a specific height (y-coordinate) that captures the shock wave. This pixel line can then be plotted over time, providing a temporal representation that enables clear observation of the oscillatory movement and position of the shock waves. Furthermore, by performing a PSD analysis for pixels from the selected line, a frequency plot along the x-axis can be derived. This frequency plot helps assess whether the shock waves oscillate in phase with each other or display phase variations.

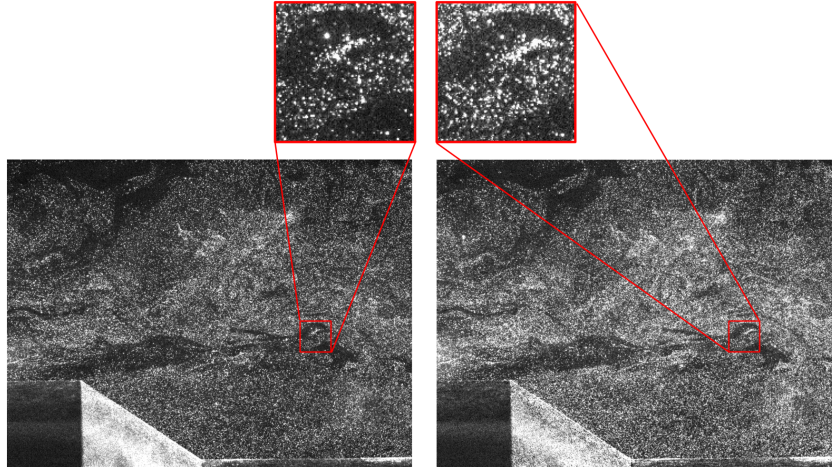
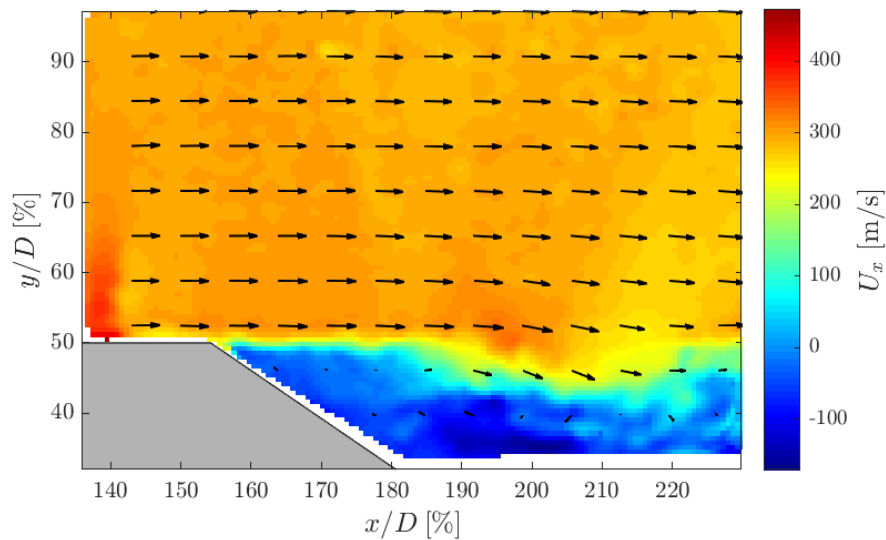
### 3.6.2. PIV Data Processing

As already mentioned, all PIV data processing is performed with DaVis 8.4. The objective of the PIV campaign is to obtain the velocity field. A pre-processing stage is necessary to enhance the quality of the raw PIV images and mitigate the impact of reflections and noise. A time-minimum subtraction filter has been employed as it is considered the most suitable option for low-frequency PIV shots, where the average fields are extracted.

The resulting filtered image pairs (see Figure 3.26) undergo cross-correlation to extract the velocity field. A multi-pass approach is employed, utilising progressively smaller window sizes. Initially, two passes are conducted using a 128x128 squared window size, followed by three passes with a 48x48 pixels circular interrogation window. This iterative process, as described by d'Aguanno [50], enables the solution to evolve from a coarse grid to a final grid. Successive passes contribute to reaching the final solution by iteratively refining the solution. The result of performing this cross-correlation into the PIV raw images from Figure 3.26 is shown in Figure 3.27.

**Table 3.7:** PIV post-processing settings

Parameter	Value
Vector spacing	0.34 mm
Final window size	48x48 px
Window overlap	75 %

**Figure 3.26:** Consecutive PIV raw images with details on a window of interrogation of 128x128 pixels.**Figure 3.27:** Horizontal velocity field  $U_x$  obtained from performing a cross-correlation procedure of the PIV raw image pair of Figure 3.26 with a multi-pass approach (two passes with squared window size of 128x128 pixels, and three passes with circular interrogation window of 48x48 pixels).

To ensure that particle information outside the interrogation window is not lost, a partial overlap of 75% is implemented. This overlap prevents the omission of particles extending beyond the interrogation window's boundaries. The main processing parameters for PIV are also reported in Table 3.7.

Finally, post-processing focuses on correcting or eliminating possible outliers, for which the universal outlier detection was applied [72]. A threshold value of 2 was chosen following

---

the results from Westerweel and Scarano [73], who observed that 90% of the spurious data was filtered with such a value. After such filtering, the average and standard deviation from the velocity fields were obtained.



# 4

## Results

This chapter presents the results of the experimental campaigns described in the preceding chapter. The emphasis is placed on discussing the observed patterns in the average and instantaneous flow fields, the results of performing a spectral analysis, and the behaviour of the wake reattachment, if existent. The aim is to provide a clear understanding of the flow dynamics associated with the different parameters investigated.

To denote the various combinations of nose and boat-tail designs, a specific naming convention is used. Specifically, the nose shape is mentioned first, followed by the boat-tail angle in degrees. This implies that when citing the benchmark case from Coe and Nute featuring a bi-conic nose and a 34-degree boat-tail, the designated nomenclature will be **BC34**. A summary of the nose shape abbreviations can be found in Table 4.1.

**Table 4.1:** Nose shape abbreviations.

Nose shape	Abbreviation
Bi-conic	BC
Conic	C
Ogive (Sears-Haack)	SH

### 4.1. General Flow Field

The experimental campaigns performed in this thesis were preceded by a review of the knowledge behind transonic flow around hammerhead PLFs (refer to section 2.1). Following that same structure, this section starts comparing the flow patterns expected around hammerhead configurations (see Figure 2.3) and the ones observed for the benchmark configuration BC34 (Coe and Nute's Model 11 [34] shown in Figure 3.5). Within this section, the current findings for that same configuration are also compared to those reported in existing literature.

Figure 4.1 shows an instantaneous Schlieren image displaying the manufactured model in the benchmark configuration where the main flow patterns are marked with arrows. This image shows how expansion fans appear in geometric transitions. This phenomenon is particularly noticeable in the zoomed-in views of Figure 4.2, which depict the area outlined in red in Figure 4.1 at various instants.

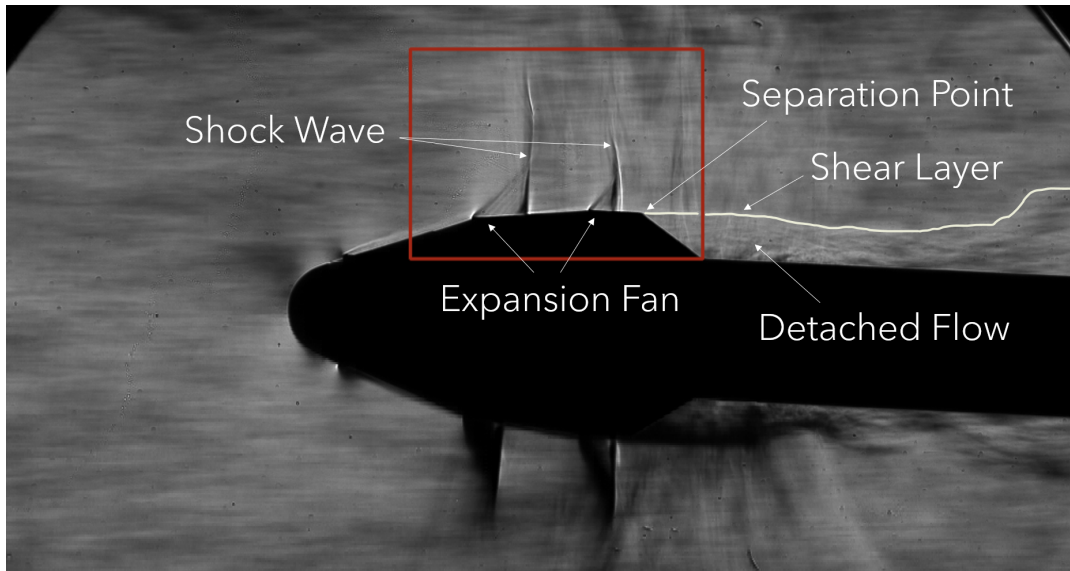


**Figure 4.1:** Schlieren image for benchmark configuration (BC34) at Mach number 0.8 and angle of attack of 4 degrees (run 20 at Table B.2) with flow patterns marked. Red rectangle shows region zoomed in the time sequence of Figure 4.2.

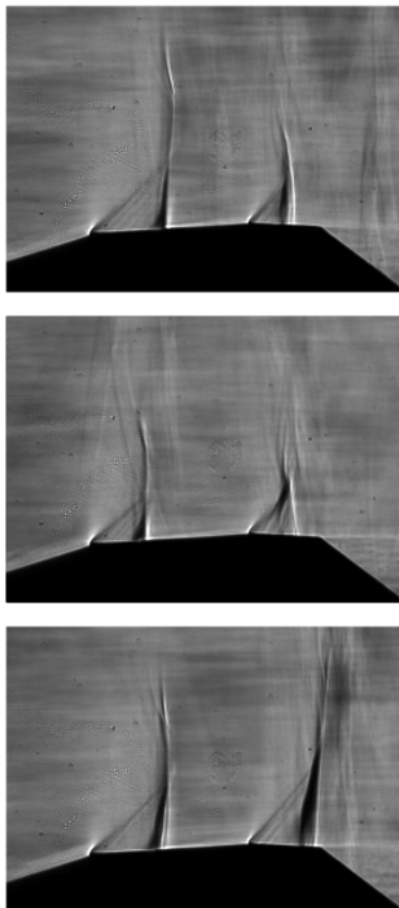


**Figure 4.2:** Time sequence with three Schlieren instantaneous shots, each taken with a time interval of  $\Delta t = 0.6$  ms between them. Focus made on the conic transitions of the BC nose (area enclosed in red in Figure 4.1). BC34 at Mach number 0.8 and angle of attack of 4 degrees (run 20 at Table B.2).

It is worth emphasising that the hammerhead configuration from the reference diagram in Figure 2.3 exhibits only an expansion fan due to its conical nose. In contrast, for alternative geometries like the bi-conical nose employed in the benchmark configuration, two distinct geometrical transitions (between both conical sections and the cone-cylinder junction) lead to the formation of two expansion fans.

These expansion fans often precede the appearance of supersonic pockets (visible as reddish areas in the upper plot of Figure 4.3 with the average x-velocity ( $U_x$ ) field for BC34, taken at a 4-degree angle of attack and a Mach number of 0.8). These supersonic pockets are enclosed by a shock wave, which frequently exhibits oscillatory behaviour.

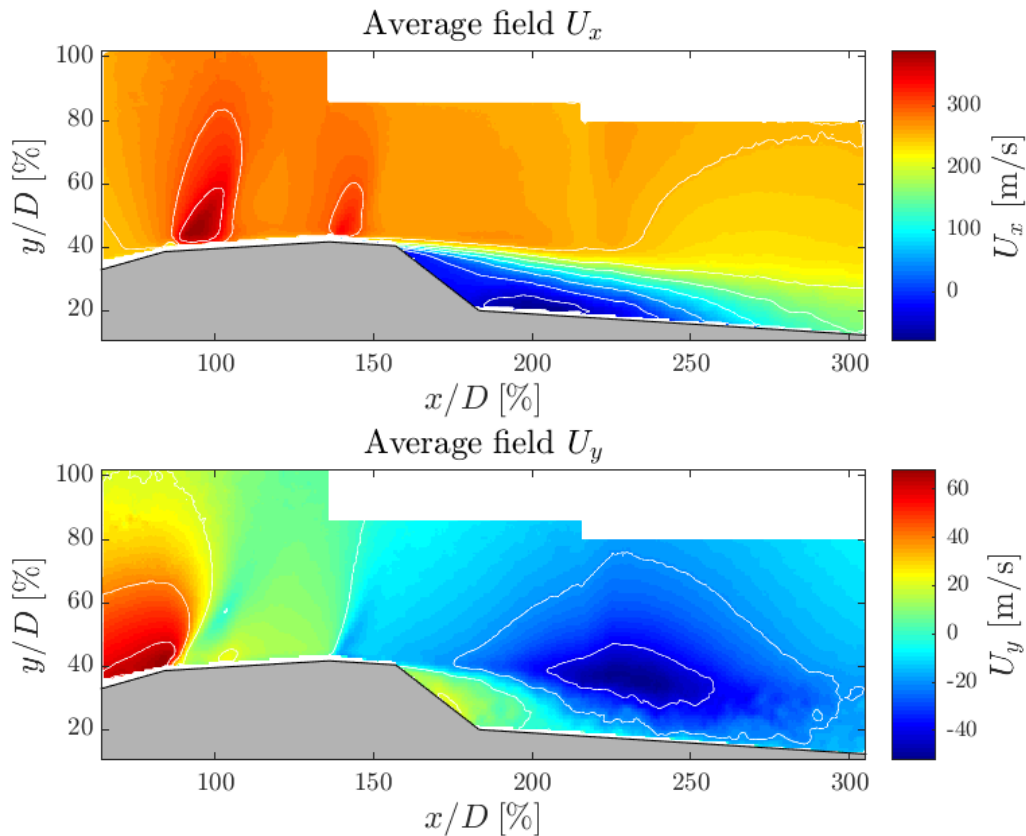


**Figure 4.3:** Average horizontal and vertical velocity fields,  $U_x$  and  $U_y$ , around benchmark configuration at  $Ma = 0.8$  and  $AoA = 4$  degrees derived from PIV (run 11 at Table B.3).

This oscillation is evident in the temporal sequence in Figure 4.2, where successive instantaneous snapshots reveal the variable shock wave positions. As commented in the literature review, knowing the existence of this oscillatory phenomenon is crucial as it intensifies the shock wave's interaction with the boundary layer, consequently inducing unsteady loads.

Hammerhead PLF configurations exhibit a distinct feature in the form of a diameter difference between the PLF and the rest of the launcher. Such change occurs along a diameter transition region known as the boat-tail, as previously discussed in chapter 1 and elaborated upon in section 2.2. Upstream of this transitional section, there is a phenomenon called shear layer detachment which marks the separation point from Figure 2.3. This detachment is evident in both Figure 4.1 and Figure 4.3. As a consequence of this detachment, a recirculation region is formed, potentially leading to reattachment.

The recirculation region is depicted in Figure 4.3. In the upper figure, representing the horizontal velocity field, dark blue areas denote regions with negative horizontal velocities, indicating a flow opposite to the freestream. Progressing downstream, lighter shades indicate a change in direction, signifying the flow's reattachment and the recirculation zone's termination. A more detailed view of this velocity field is given in the zoomed-in Figure 4.4, which includes streamlines that facilitate the visualisation of the recirculation and reattachment points.

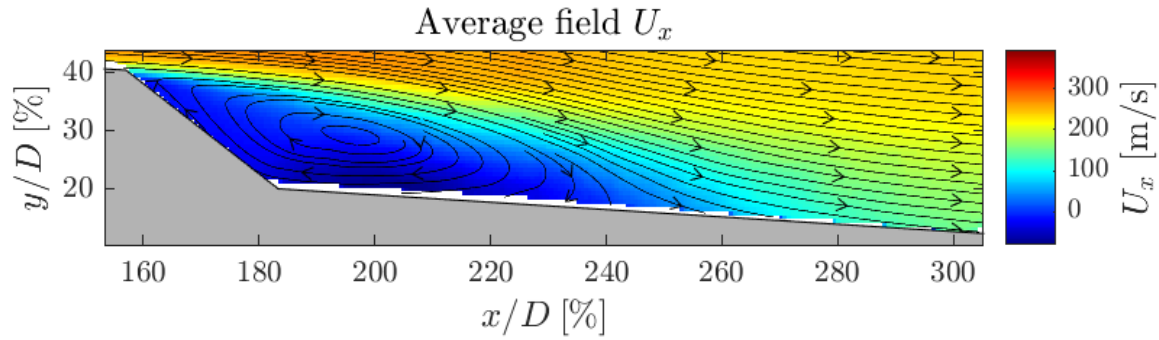


**Figure 4.4:** Boat-tail area zoom of the average horizontal velocity field  $U_x$  for  $Ma = 0.8$  and  $AoA = 4$  degrees (run 11 at Table B.3).

In contrast, the lower plot in Figure 4.3, which displays the vertical flow field, showcases blue regions where the flow descends, while the yellowish area near the boat-tail signifies an upward flow. This transition between upward and downward flow patterns illustrates the recirculation and subsequent reattachment of the flow.

Recirculation is a prime illustration of unsteadiness, with a fluctuating behaviour over time, which turns a challenge to capture its true essence solely through the average flow. While plots like Figure 4.4 shed light on the occurrence of recirculation, it is crucial to recognise that the depicted flow should not be assumed as steady. This concept becomes more apparent when examining Figures 4.5 and 4.6, which display the standard deviation of the x-velocity and the percentage of reverse flow per pixel, respectively.

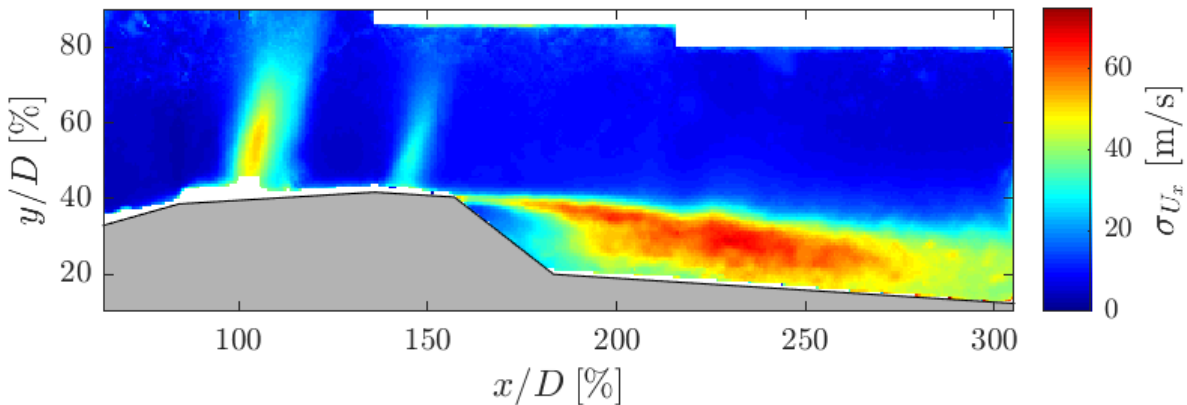


**Figure 4.5:** Standard deviation field of the horizontal velocity  $U_x$  around benchmark configuration at  $Ma = 0.8$  and  $AoA = 4$  degrees derived from PIV (run 11 at Table B.3).

The standard deviation field of Figure 4.5 helps discern areas with high levels of unsteadiness, notably around shock wave locations (after the bi-conic and cone-cylinder transitions of the nose) and in the region of detached flow, where the peak of  $\pm 75.23$  m/s is found.

In Figure 4.6, illustrating the percentage of reverse flow per velocity vector over all available images for PIV run 11, red regions indicate where reverse flow persists in over 80% of the cases. While these regions do indeed exhibit reversed flow in the average fields, the same cannot be said of nearby areas where reversed flow exists in between 20-80% of the images taken (see Figure 4.6) but the flow seems aligned with the freestream direction in Figure 4.4. This contradiction underscores the unsteadiness present in the recirculation region.

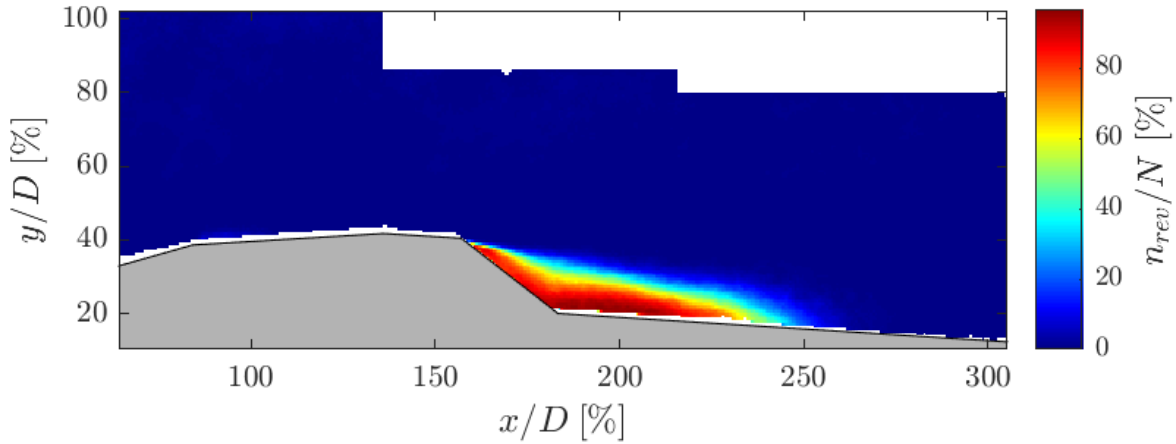


**Figure 4.6:** Number of times each velocity vector had reverse flow,  $n_{rev}$ , over the total 479 PIV images considered,  $N$ , for BC34 at  $Ma = 0.8$  and  $AoA = 4$  degrees (run 11 at Table B.3).

Suppose conclusions were solely drawn from the average fields. In that case, one might assume that these fields represent steady phenomena over time, implying that areas where the flow reverses at specific instants were, instead, always following the freestream direction. Such unsteady behaviour leads to the conclusion that the reattachment location varies over time, a fact that is further discussed and illustrated in later sections.

Finally, the reattachment location can also be identified from the oil flow patterns as in Figure 4.7. The area where the flow reattaches can be discerned because the oil concentration is lower due to the change of flow direction between the recirculation region and when the flow realigns with the freestream direction. It is worth noting that in this case, the angle of attack causes the oil flow patterns around reattachment to curve, as discussed in section 4.4. The inclination disrupts the model's symmetry, leading to pressure differences between the upper and lower parts. Such pressure variations affect how phenomena like flow detachment and reattachment occur along the model, explaining the curvature in the oil patterns.

#### Comparison with Literature

Utilising Coe and Nute's extensively examined model 11 [34] as a reference case (refer to subsection 2.2.3) facilitates a comparative analysis of outcomes obtained within the context of this research's experimental endeavours and those documented by other investigators. Specifically, this section juxtaposes instantaneous Schlieren images captured for the benchmark configuration, BC34, at a 4-degree angle of attack, with shadowgraphy representations put forth by Panda et al. [39].

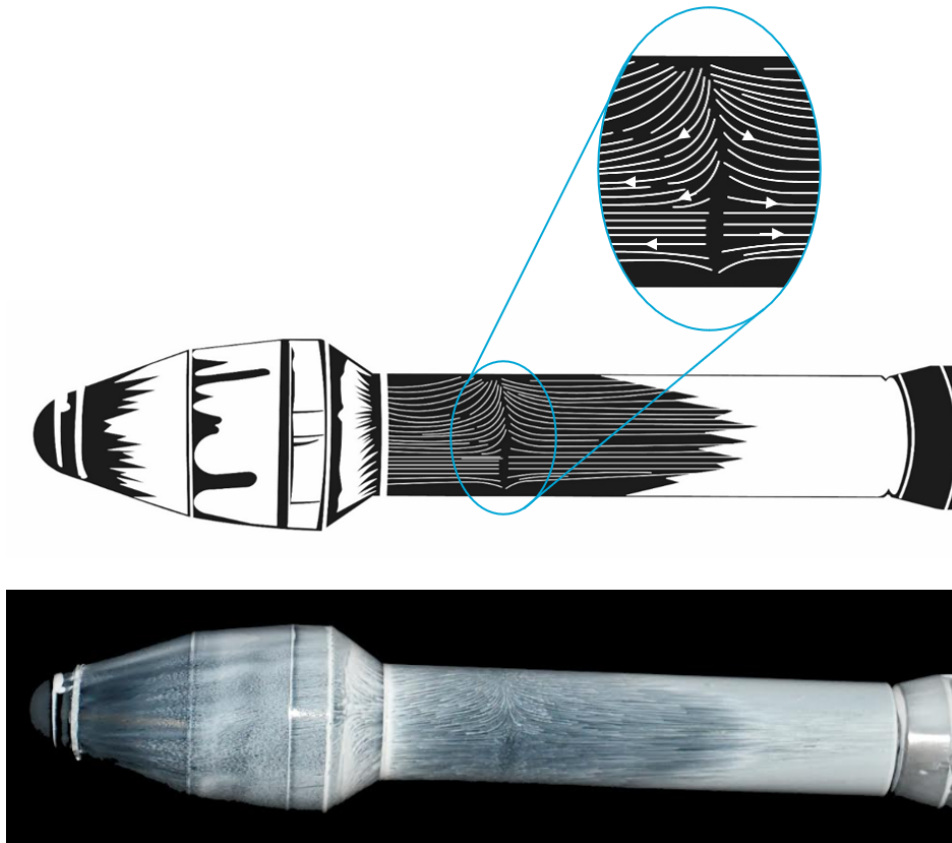


**Figure 4.7:** Schematic and photography of oil flow patterns for BC34 at  $Ma = 0.8$  and  $AoA = 4$  degrees (run 28 Table B.1). Detail zoom showcases oil flow direction in reattachment area (as seen in recording).

Figure 4.8 compares the literature shadowgraphy and the current research's Schlieren pictures for Mach number of 0.6 and a 4-degree angle of attack. Both images showcase the flow around the model with no shock waves and the shear layer detaching at the beginning of the boat-tail region. According to Panda et al., no shock waves are formed at Mach numbers lower than 0.7. However, the data obtained for a Mach number equal to 0.7, which cannot be compared to Panda's for lack of those, shows the opposite, as a shock wave can be hinted at the geometric transition between conic sections (see Figure 4.9).

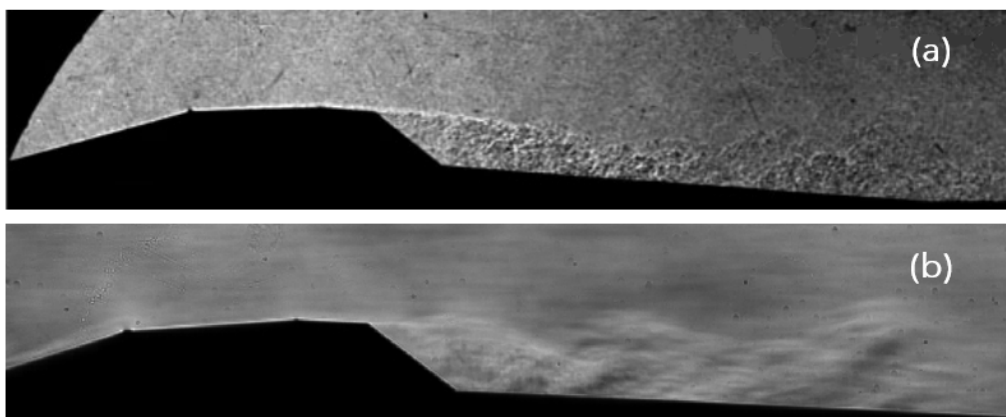


**Figure 4.8:** Comparison between instantaneous (a) shadowgraphy picture from Panda [39] (see Figure 2.18) and (b) schlieren image (run 18 at Table B.2) for  $Ma = 0.6$  and  $AoA = 4^\circ$ .



**Figure 4.9:** Instantaneous schlieren image (run 19 at Table B.2) for  $Ma = 0.7$  and  $AoA = 4^\circ$ .

Lastly, Figure 4.10 compares the outcomes from Panda's analysis for Mach numbers 0.8 and 0.85 with an image at Mach 0.8 from this study. It becomes evident that the locations of shock waves in the present investigation agree more with Panda's findings at Mach 0.85. Specifically, Panda's outcomes at Mach 0.8 portray both shock waves converging at the geometric junctures, while his findings at Mach 0.85 and the results obtained herein for Mach 0.8 display more downstream locations.

This apparent resemblance acquires significance given that the TST-27 test section (the wind tunnel employed in this research, as explained in section 3.1) was not outfitted with slotted walls. Moreover, prior investigations executed within these same facilities mention the presence of blockage effects [50, 74]. This similarity between Panda's Mach 0.85 results and the present study's Mach 0.8 outcomes, surpassing what would be anticipated for equivalent Mach numbers, corroborates the notion that the model's perceptible Mach number exceeded the value set from the control room. Future investigations could incorporate a comprehensive analysis of blockage to determine whether this scenario holds true. One potential approach involves conducting Computational Fluid Dynamics (CFD) simulations with the model within and outside the test section. This method would enable a thorough evaluation of the potential impact of the walls on the Mach number.

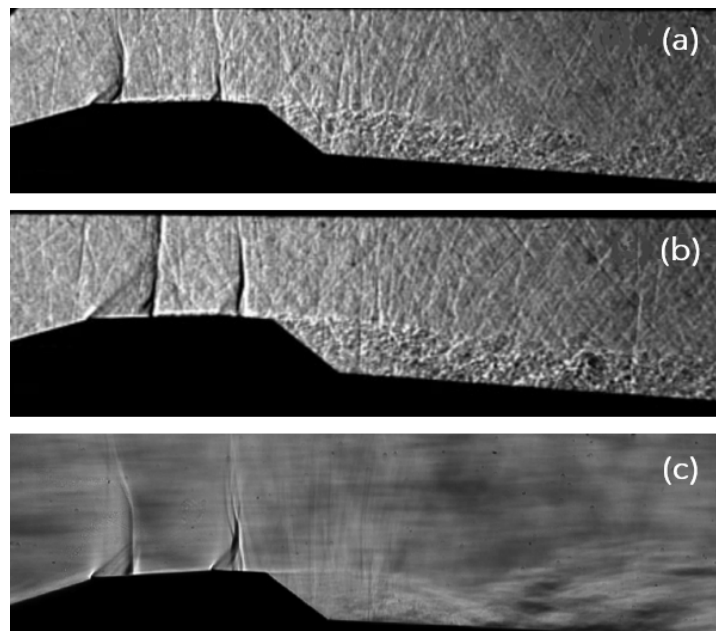


**Figure 4.10:** Comparison of benchmark configuration at  $AoA = 4$  degrees: (a) Instantaneous shadowgraphy from Panda [39] at  $Ma = 0.8$  (see Figure 2.18), (b) Instantaneous shadowgraphy from Panda [39] at  $Ma = 0.85$  (see Figure 2.18), and (c) Schlieren image (Run 20 at Table B.2) at  $Ma = 0.8$ .

## 4.2. Geometrical Effects

To answer the main research question: ***How do the nose and boat-tail geometries impact the flow phenomena (e.g., shock wave generation) around a hammerhead configuration PLF in transonic conditions?***, a model with interchangeable nose and boat-tail regions was designed and manufactured (refer to section 3.2).

This section discusses the effects of the different nose and boat-tail shapes in the flow as observed in the results of the tests performed. Specifically, the differences observed in the flow due to the usage of one geometry or another are commented on, seeking to extract conclusions and prove whether the effects discussed in the literature were also observed.

### 4.2.1. Nose

To study the effect that the nose has on the flow, the three manufactured geometries were tested in different conditions during the oil flow and Schlieren campaigns (refer to Table B.1 and Table B.2 for the specific cases). The flow patterns observed for different nose geometries consistently matched the characteristic patterns for hammerhead configurations in the transonic regime, reviewed and compared to the benchmark case in section 4.1.

This is illustrated in Figure 4.11, which displays three Schlieren images featuring a 34-degree boat-tail, Mach 0.8, and zero angle of attack with the bi-conic, conic and ogive noses. In all cases, expansion fans precede shock waves near geometric transitions, and the flow separates around the boat-tail region, aligning with the trends described in section 4.1.

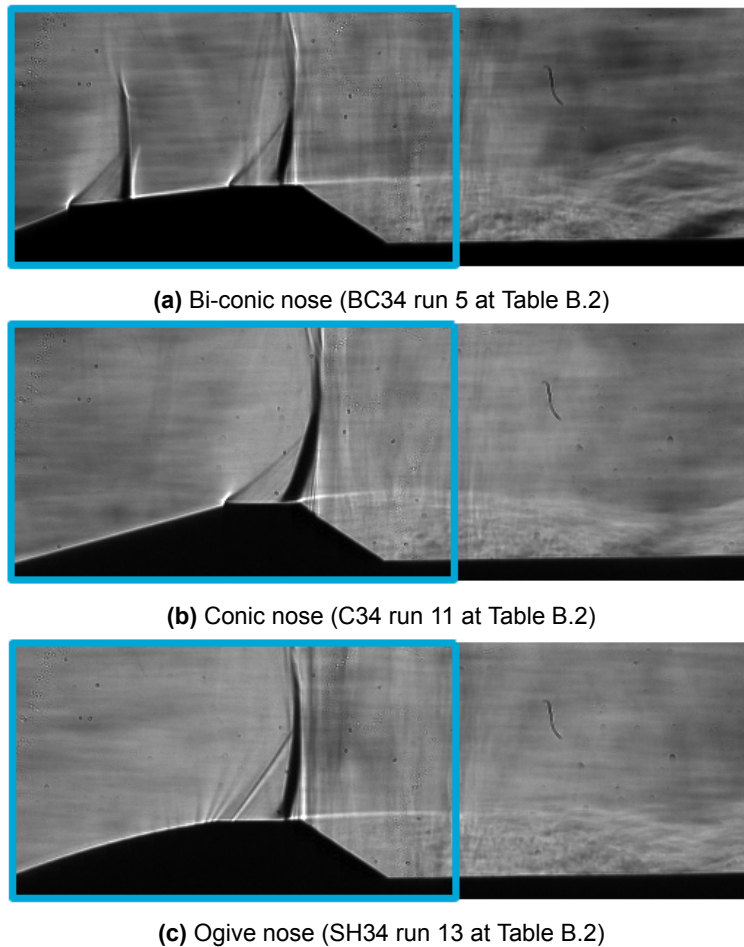


**Figure 4.11:** Schlieren instantaneous images for  $Ma = 0.8$ ,  $AoA = 0$  degrees, boat-tail of 34 degrees and bi-conic, conic and ogive noses.

Focusing on the regions outlined in blue in Figure 4.11, the variations induced by the nose geometry can be observed. With a bi-conic nose, two distinct shock waves form. Conversely, with the conic and ogive noses, only one appears. Moreover, these images show how the expansion fan preceding the shock waves is similar for both bi-conic and conic, while the ogive case seems to extend further following the curvature of the shape. This seems to mitigate its effects, resulting in a lower density variation.

Finally, Figure 4.12 presents a closer look at the areas highlighted in red in Figure 4.11 for a couple of instances that illustrate the shock wave's locations - both furthest downstream and furthest upstream - for each case. These images reveal the initiation of flow separation right at the shock wave for the conical case, with the separation process oscillating alongside it. In contrast, separation commences at the onset of the boat-tail section for the alternative nose geometries. Furthermore, it is noteworthy that the shock wave associated with the conical nose exhibits a notably curved shear layer (noticeable at Figure 4.11b), indicating its higher strength compared to the other cases.

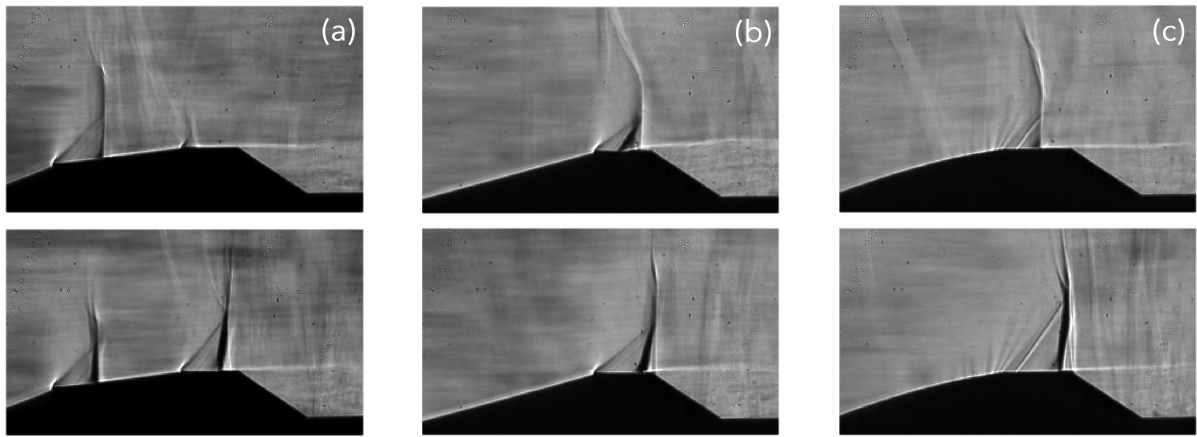


**Figure 4.12:** Comparison between schlieren instantaneous images showing the most downstream and upstream shock wave locations for  $Ma = 0.8$ ,  $AoA = 0$  degrees and geometries (a) BC34, (b) C34 and (c) SH34 (runs 5, 11 and 13 at Table B.2, respectively). Zoom into red region of Figure 4.11.

Each schlieren run comprises 5457 images similar to those shown in Figure 4.11. The variation in pixel intensity across the photographs can be assessed through the standard deviation. Figure 4.13 illustrates this metric for runs 5, 11, and 13, on the area enclosed in red in Figure 4.11.

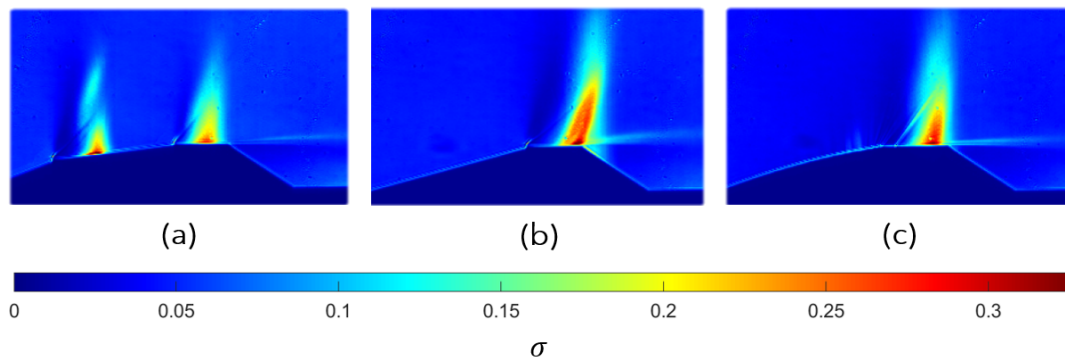


**Figure 4.13:** Comparison between pixel intensity standard deviation of the schlieren images for  $Ma = 0.8$ ,  $AoA = 0$  degrees and geometries (a) BC34, (b) C34 and (c) SH34 (runs 5, 11 and 13 at Table B.2, respectively).

Examining Figure 4.13, it is clear that the conic nose shows the most significant fluctuations near the shock wave location (the ranges of shock wave movement, observed from the schlieren runs, are summarised in Table 4.2 and analysed in section 4.6). By only assessing the standard deviation right before the detached flow, which reflects the unsteadiness associated with shock wave oscillations, the ogive nose would appear more unsteady than the bi-conic. On one side, this would correspond to the literature (refer to subsection 2.2.1) when stating that ogive shapes generate a weaker terminal shock on the cylindrical section of the fairing compared to conical, if it is assumed the level of oscillation corresponds to the strength of the shock wave [36]. Conversely, such a conclusion would paradoxically clash with the notion from literature (refer to subsection 2.2.1) that ogive shapes reduce the most unsteady loads compared to any other nose geometries.

The bi-conic nose, contrary to the others, gives rise to two different shock waves, which overall can imply higher unsteadiness than the ogive with a unique shock, in line with the consensus articulated in the consulted literature. However, this comes by only assessing the apparent unsteadiness due to the shock waves oscillations, and other unsteadiness sources should be considered for a complete conclusion on which geometry induces more or less unsteady loads.

Refocusing on the conic nose configuration and comparing its standard deviation with the bi-conic counterpart provides valuable insights that align with the phenomenon outlined by Ericsson [32]. Ericsson's research concluded that implementing bi-conic nose geometries effectively mitigates abrupt shifts in flow separation patterns, subsequently reducing aeroelastic instabilities compared to their conic counterparts. This mitigation is attributed to the pre-separation effect occurring at the shoulder of the bi-conic shape.

In line with Ericsson's assertions, this behaviour also prevents separation between the cone and cylinder. Notably, in conic configurations, flow detachment occurs within the shock wave generated during the cone-cylinder transition (see Figure 4.11b). In contrast, in the bi-conic configuration, the point of separation appears to align more closely with the start of the boat-tail region.

However, it is important to note that an unequivocal determination regarding whether the separation in the bi-conic configuration occurs within the shock wave or at a later stage cannot be exclusively drawn from the instantaneous images. Nevertheless, the noticeable difference in standard deviation intensity between the shock waves in the bi-conic and conic cases also supports Ericsson's conclusions. The standard deviation intensity of both shock waves in the bi-conic scenario is notably milder than the singular shock wave encountered in the conic configuration. This implies that in the conic case, more oscillations occur, which further substantiates the notion that the shock wave is stronger.

The analysis of oil flow patterns (as shown in Figure 4.14) alongside corresponding recordings for configurations featuring a 34-degree boat-tail with bi-conic, conic, and ogive noses, reveals distinct variations in flow behaviour contingent upon the employed nose geometry. Differences emerge in regions surrounding the nose-cylinder and boat-tail areas.

In both conic and bi-conic nose designs, a noticeable oil accumulation is observed immediately preceding the cumulation resulting from the transition strip, a consistent feature across all three cases. This is followed by a region exhibiting reduced oil presence in all instances, succeeded by a smooth reappearance of oil due to the boundary layer turbulent transition enforced by the transition strip. Notably, in Figure 4.14a, oil exhibits waviness along the second conical section, possibly attributable to the oscillations of the two shock waves present in that area (see Figure 4.2). It is worth highlighting how the point of shear layer separation closely aligns with the initiation of the boat-tail for all cases.

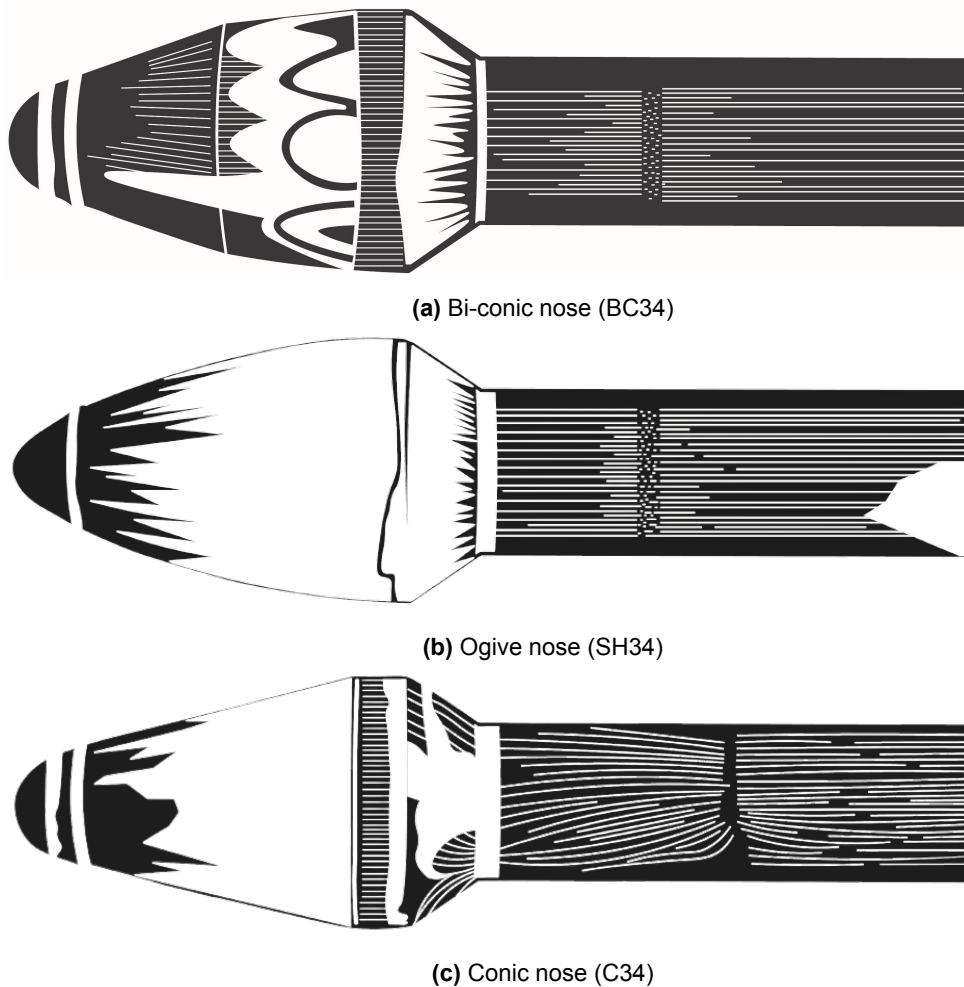


**Figure 4.14:** Schematic representation of the oil flow patterns (see a comparison with photographs in Appendix C) obtained at  $Ma = 0.8$ ,  $AoA = 0$  degrees (runs 30, 31 and 32 at Table B.1).

A distinctive feature among the three configurations is the reattachment section. Specifically, in the conic case, this location appears furthest downstream (as also discussed in section 4.6). Moreover, it is the only configuration exhibiting curvature akin to that induced by angle of attack effects. This behaviour could be attributed to a separated region characterized by a higher energetic level.

In contrast, the reattachment location and shape for the bi-conic and ogive cases are similar. The primary distinction between these configurations lies in the nose region, where patterns for the ogive case suggest a smoother flow.

#### 4.2.2. Boat-Tail

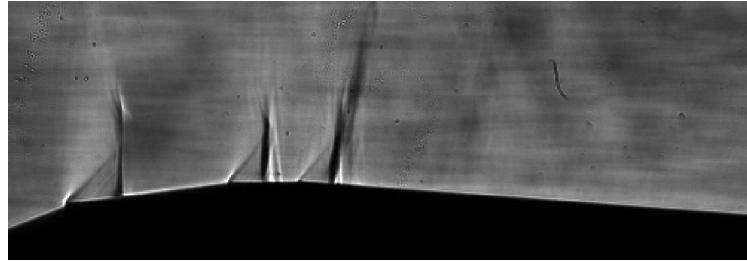
A general overview of the differences observed when only varying the boat-tail can be made by looking at the instantaneous schlieren shots of Figure 4.15. These images correspond to runs conducted at Mach 0.8, with a null angle of attack, a bi-conic nose, and boat-tail angles of 5, 15, and 34 degrees.

The first noticeable difference is that only the 34-degree boat-tail presents two shock waves due to the geometric transitions at the nose. Conversely, the other boat-tail angles result in an additional shock wave emerging at the beginning of the boat-tail.

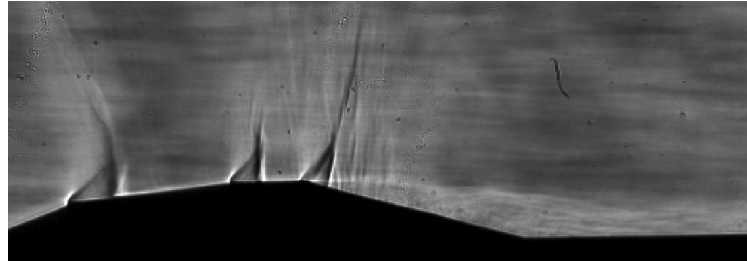
This may be explained by the direct impact of a steeper boat-tail angle, which prompts the detachment of the shear layer, hindering flow attachment and subsequent re-acceleration.

Regarding flow detachment, the setup with a 5-degree boat-tail (Figure 4.15a) lacks a discernible detached region, unlike the other cases. Notably, the width of the detached flow for the 15-degree boat-tail (Figure 4.15b) appears narrower compared to the 34-degree variant (Figure 4.15c).

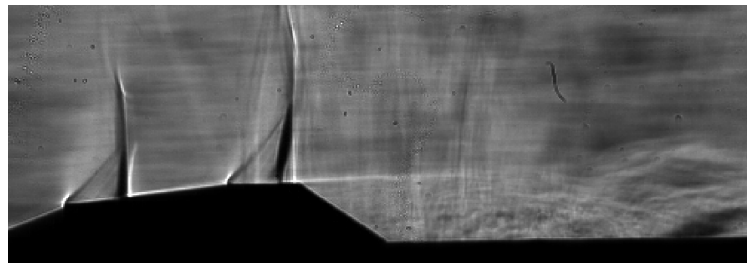
A scenario contrary to expectations might be attributed to the presence of the third shock wave. Conventional wisdom would suggest that cases with more pronounced detached regions would entail higher levels of unsteadiness. However, a contrasting interpretation arises upon careful examination of pixel intensity standard deviation fields and the sequence of snapshot images, in relation to the unsteadiness associated with shock wave oscillations.



(a) Boat-tail of 5 degrees (BC5 run 7 at Table B.2)



(b) Boat-tail of 15 degrees (BC15 run 9 at Table B.2)



(c) Boat-tail of 34 degrees (BC34 run 5 at Table B.2)

**Figure 4.15:** Schlieren instantaneous images for  $Ma = 0.8$ ,  $AoA = 0$  degrees, bi-conic nose and boat-tail angles of 5, 15 and 34 degrees.

Figure 4.16 presents the pixel intensity standard deviation for schlieren runs 7, 9 and 5 as referred in Table B.2. These plots illustrate how an additional shock wave increases the width of the second region characterised by a substantial standard deviation (second shock wave location). This phenomenon can be better understood by referring to Figures 4.17 and 4.18, which present instant image sequences showing the oscillatory behaviour of the shock waves. These figures reveal that the oscillations and the proximity of the last two shock waves induce their fusion. Consequently, the resultant shock wave appears more significant than its initial state, implying an increase in energy. However, the standard deviation peak in the region is lower in both cases (see a and b at Figure 4.16) than for the 34-degree boat-tail.

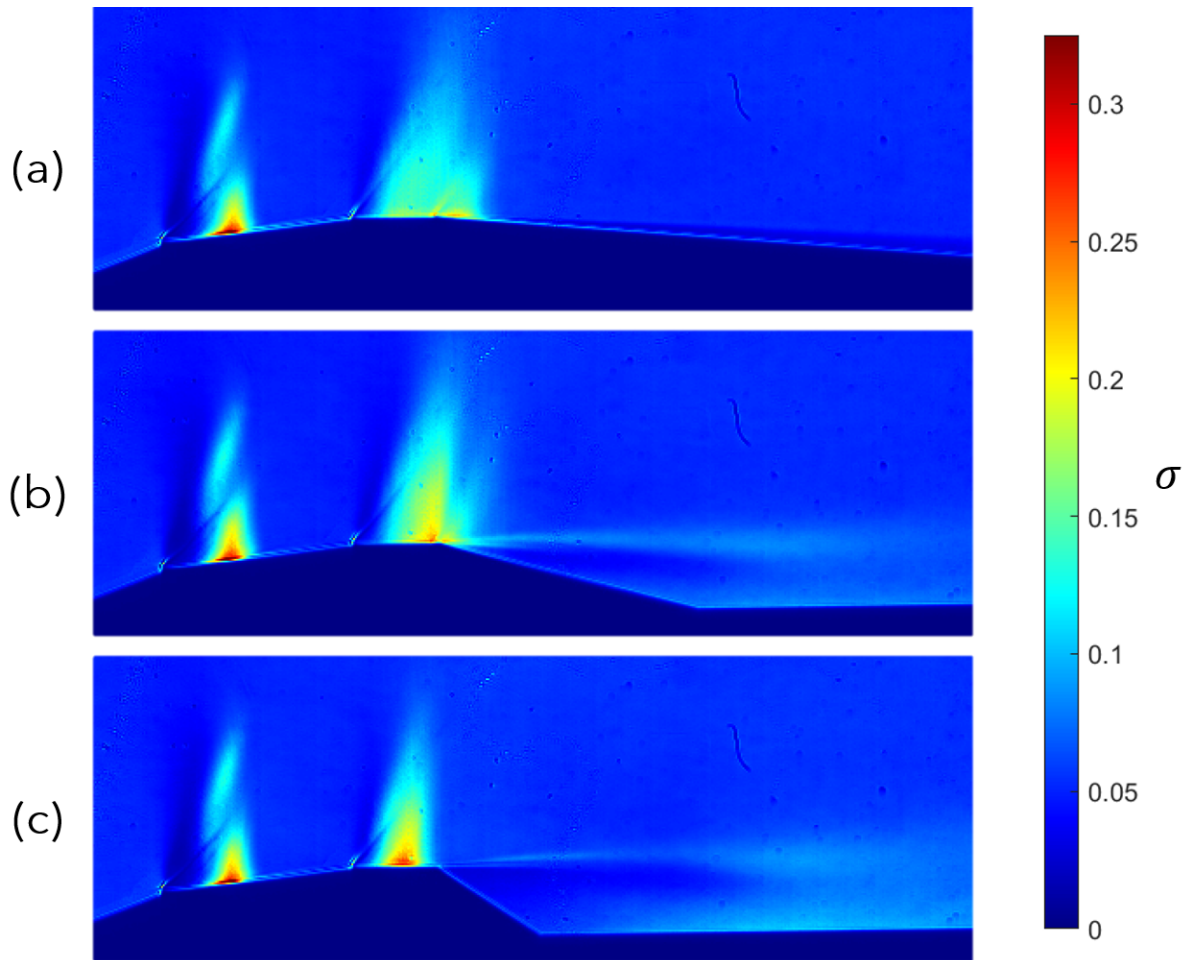


**Figure 4.16:** Comparison between pixel intensity standard deviation of the schlieren images for  $Ma = 0.8$ ,  $AoA = 0$  degrees, bi-conic nose and boat-tail angles of (a) 5, (b) 15 and (c) 34 degrees (runs 7, 9 and 5 at Table B.2, respectively).

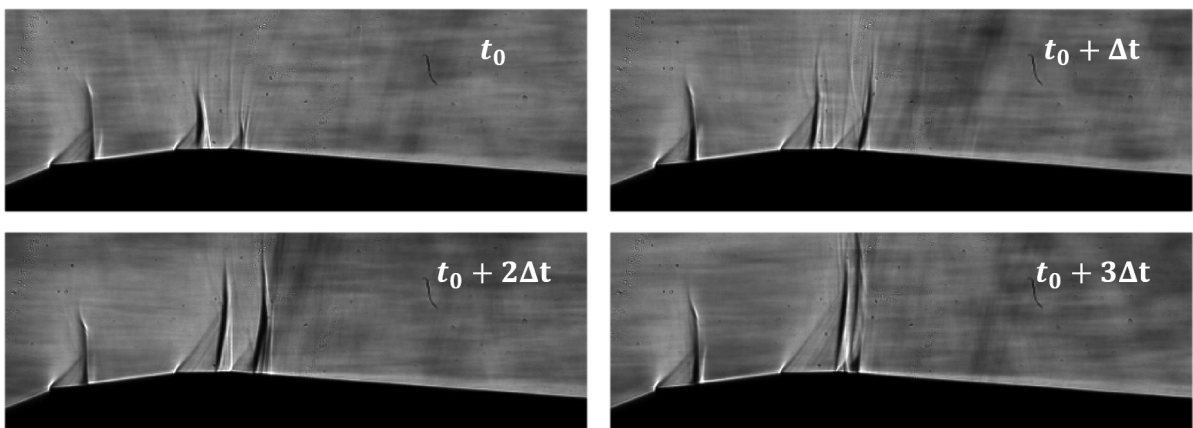


**Figure 4.17:** Time sequence with schlieren instantaneous images, each taken with a time interval of  $\Delta t = 0.2 \text{ ms}$  between them for BC5. Focus made on the nose and boat-tail regions at  $Ma = 0.8$  and  $AoA = 0$  degrees (run 7 at Table B.2).

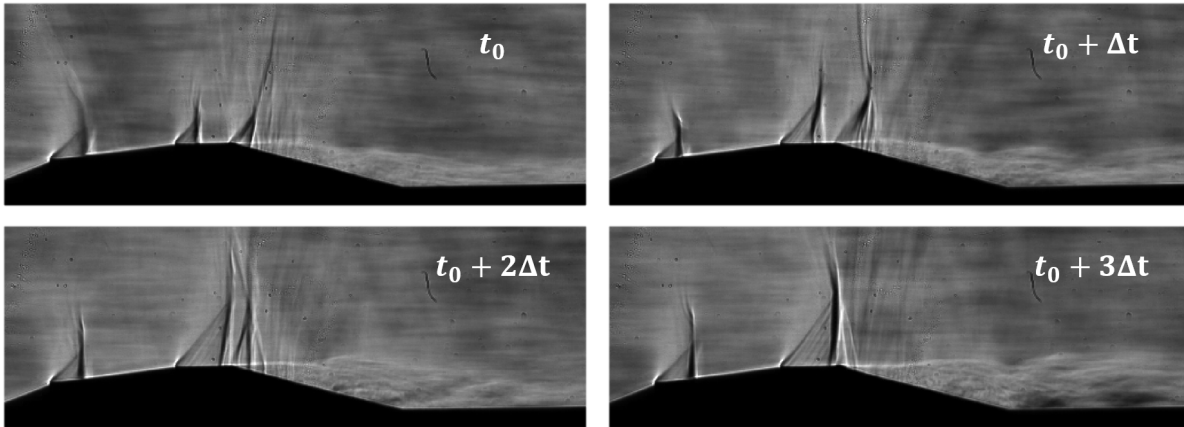


**Figure 4.18:** Time sequence with schlieren instantaneous images, each taken with a time interval of  $\Delta t = 0.2 \text{ ms}$  between them. Focus made on the bi-conic nose and 15-degree boat-tail regions at  $\text{Ma} = 0.8$  and  $\text{AoA} = 0$  degrees (run 9 at Table B.2).

Furthermore, these sequences provide a more precise visualisation of the width of the detached shear layer. This is particularly evident in the case of run 9 with a 15-degree boat-tail, where instances with significantly narrower detached regions are observable. This variation suggests that the shear layer's detachment is subject to width fluctuations, also inducing the reattachment location variation (see section 4.6).

In conclusion, the boat-tails with 5 and 15 degrees for Mach 0.8 appear to induce similar flow patterns, characterised by substantial shock interaction with the boat-tail section in both cases. In contrast, the 34-degree boat-tail exhibits the anticipated wake-like separated flow over an extended region, as discussed in subsection 2.2.2. Notably, at 0-degree angle of attack and Mach 0.8, the 15-degree boat-tail experiences significant shock interaction with the boat-tail and triggers the wake-like separated flow, resulting in a combination of the flow patterns induced by the 5 and 34-degree configurations.

Future research should focus on a more comprehensive assessment of the specific unsteady levels induced by these different geometries. While boat-tails with 5 and 15-degree angles may induce wider regions of unsteadiness, the evaluation conducted in this study pertains solely to unsteadiness arising from shock wave oscillations. A more comprehensive assessment might reveal that higher levels of unsteadiness exist across all aspects of the 34-degree case, potentially due to additional factors beyond shock wave oscillations.

### 4.2.3. Nose and Boat-Tail Effects Dependence

To have a better comparison into the commented cases with equal boat-tail and different nose, and the opposite, Figure 4.19 compiles the pixel intensity standard deviation fields for cases with bi-conic nose and 34 and 5-degree boat-tails, and ogive nose and again 34 and 5-degree boat-tails (a, b, c and d, respectively), which correspond to the two most used nose geometries by the industry.

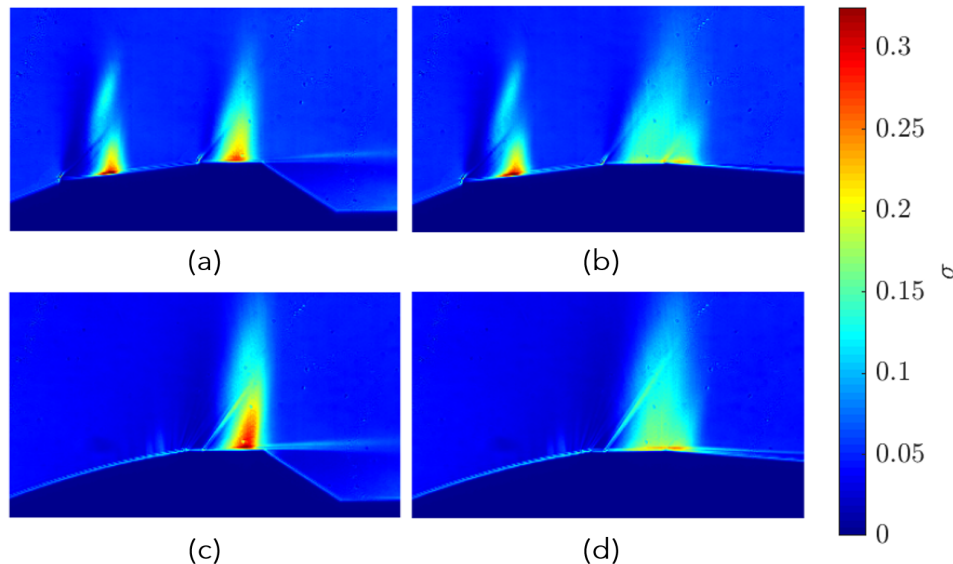


**Figure 4.19:** Pixel intensity standard deviation of schlieren images for  $Ma = 0.8$ ,  $AoA = 0$  degrees and geometries (a) BC34, (b) BC5, (c) SH34, and (d) SH5 (runs 5, 7, 13 and 15 at Table B.2).

The effect of the nose and the boat-tail on the flow is differentiable from those fields. This influence remains distinct from other factors, manifesting as an independent effect. Opting for a bi-conic nose design over an ogive counterpart induces the formation of two shock waves, which display a diminished degree of variability compared to the singular shock wave produced by the ogive nose design (lower standard deviation). In a complementary manner, the introduction of a 5-degree boat-tail triggers the emergence of an additional shock wave (can be better observed in Figure 4.20, where a sequence of instantaneous schlieren images illustrates the evolution of shock waves for an ogive nose combined with a 5-degree boat-tail, operating at Mach 0.8 and a zero angle of attack). Notably, this configuration encourages the interaction between the shock waves and the boat-tail section.

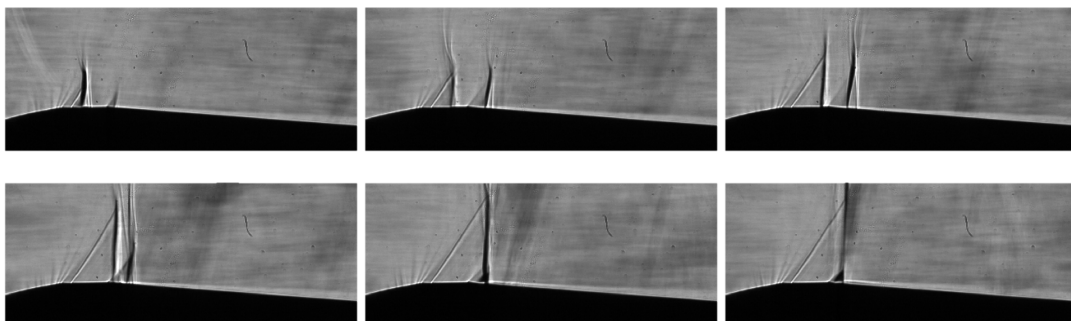


**Figure 4.20:** Time sequence with schlieren instantaneous images, each taken with a time interval of  $\Delta t = 0.2$  ms between them. Focus made on the ogive nose and 5-degree boat-tail regions at  $Ma = 0.8$  and  $AoA = 0$  degrees (run 15 at Table B.2).

Observations from Figure 4.20 further substantiate the autonomy of this distinctive effect, where the progressive oscillation of the shock waves, coupled with their intermittent convergence, bears a notable resemblance to the patterns observed in the plots for scenarios involving bi-conic nose configurations (refer to Figures 4.17 or 4.18).

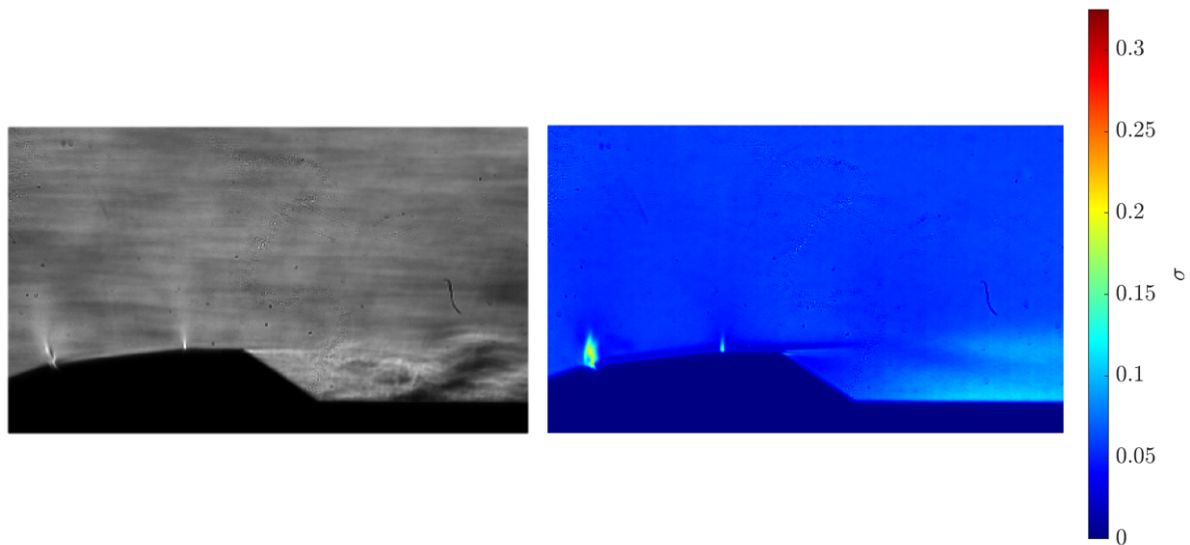
### 4.3. Mach Number Effect

During the experimental campaigns, two Mach numbers were usually tested for all configurations: 0.7 and 0.8. As discussed in section 4.1, the effective Mach number at the test section may be considerably higher than the nominal value set in the control room. This discrepancy arises due to the presence of the model and its blockage effects. Consequently, when interpreting the outcomes, it becomes imperative to acknowledge that the results exclusively facilitate conclusions regarding the effects of increasing the Mach number without establishing a direct correlation to any specific numerical value.

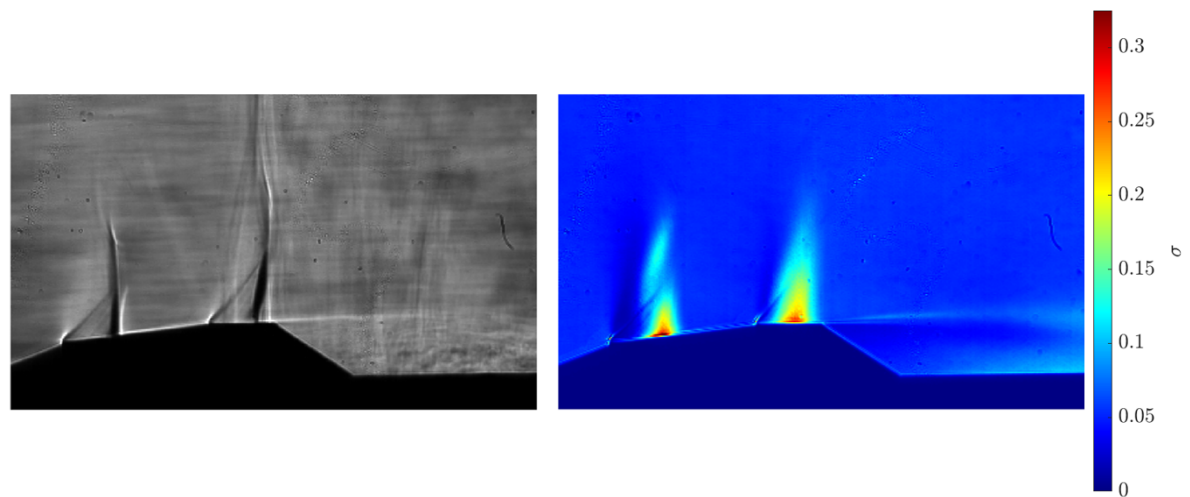
The effect of an increase in Mach number is consistent across all cases, resulting in heightened levels of both shock wave instability and intensity. A case in point is illustrated in Figure 4.21, which provides a comparative depiction of pixel intensity standard deviation derived from schlieren images alongside instantaneous captures for two specific runs (2 and 5, as detailed in Table B.2). These runs correspond to the benchmark configuration, characterized by a bi-conic nose and 34-degree boat-tail, at a 0-degree angle of attack and Mach values of 0.7 and 0.8, respectively.

The observed trends in Figure 4.21 underscore two primary effects stemming from the increase in Mach number. Firstly, the intensity of the shock waves amplifies noticeably in both cases, albeit the shock wave at Mach 0.7 is nearly imperceptible in certain instances. Secondly, the unsteadiness of the shock waves intensifies, evident through sequential observation of the instantaneous shots or by gauging the standard deviation. This outcome aligns with theoretical expectations, as elevating the Mach number corresponds to a flow trajectory approaching supersonic conditions.

Moreover, a visual inspection of the images provides insight into additional observations. Notably, the expansion fans exhibit greater clarity at Mach 0.8 compared to the Mach 0.7 scenario, where they remain indiscernible from the imagery.



(a) Ma = 0.7 (run 2 at Table B.2)



(b) Ma = 0.8 (run 5 at Table B.2)

**Figure 4.21:** Instantaneous schlieren picture and pixel intensity standard deviation from schlieren images for the benchmark case (Coe and Nute's model 11 [34]) at AoA = 0 degrees for Mach numbers of 0.7 and 0.8.

The statistical data derived from the PIV images corroborates the observations made using schlieren images. In Figure 4.22, the average horizontal velocity  $U_x$  fields are displayed for increasing Mach numbers. This reveals that the supersonic pocket following the expansion fan grows with Mach, accompanied by higher maximum velocities. This suggests that with an increasing Mach number, the shock wave's position moves further downstream as observed when comparing the instantaneous schlieren image from Figure 4.21a with Figure 4.21b.

Moreover, the standard deviation field obtained from the horizontal velocity (Figure 4.23) reinforces this trend. In the Mach 0.8 case, areas with a higher standard deviation, indicative of shock wave oscillation, are observed at approximately 100% of the diameter  $D$ , while for Mach 0.7, this region is closer to 85%  $D$ , approximately where the bi-conic shoulder is located.

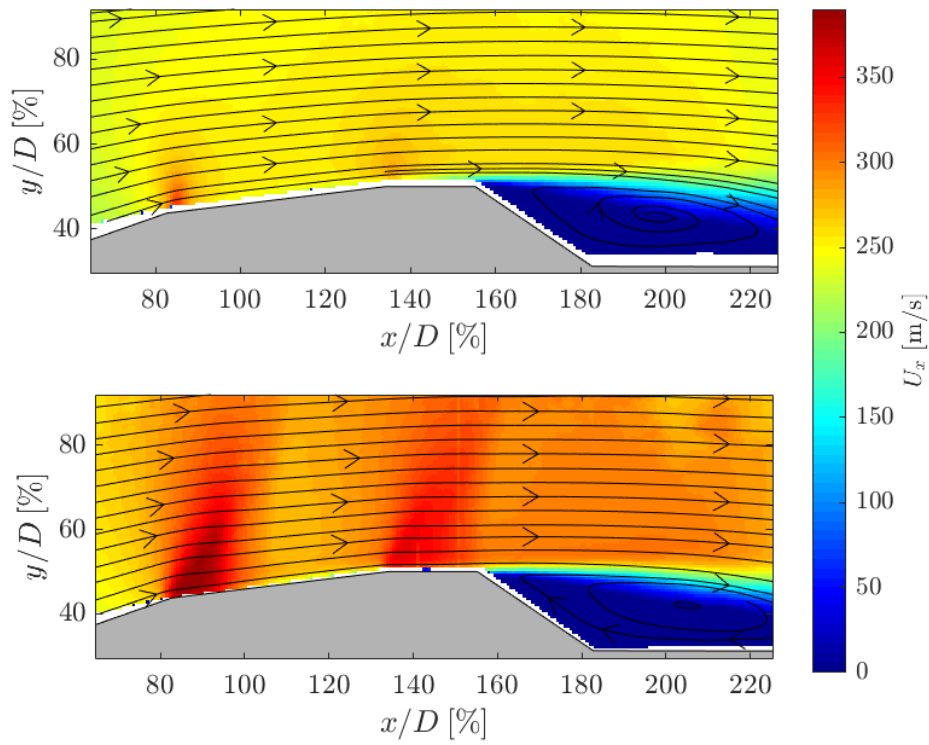


**Figure 4.22:** Horizontal velocity  $U_x$  average field for PIV runs with the benchmark configuration (BC34) at 0-degree angle of attack. Top plot corresponds to Mach 0.7, and bottom plot to 0.8 (PIV runs 1+2 and 3+4 in Table B.3).

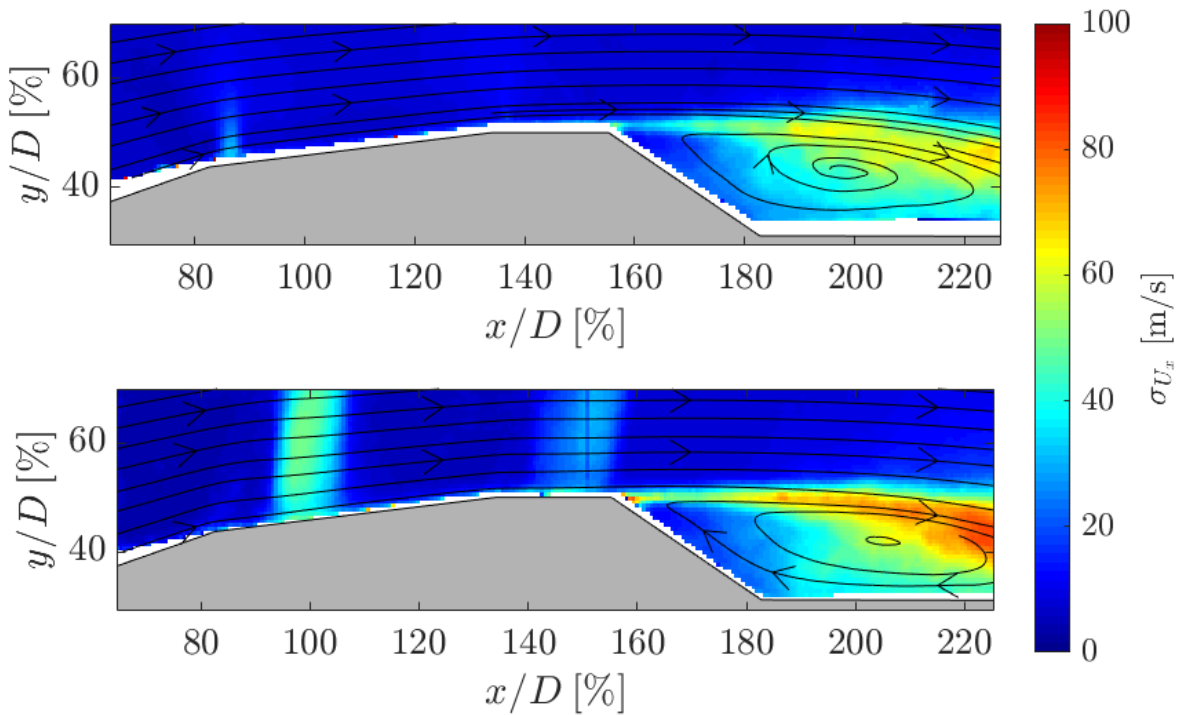
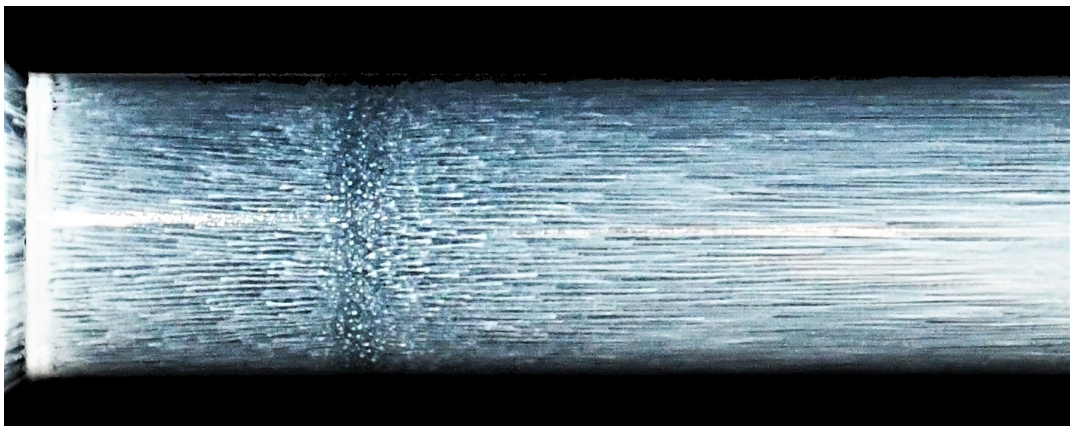


**Figure 4.23:** Horizontal velocity standard deviation  $\sigma_{U_x}$  field from PIV runs with the benchmark configuration (BC34) at 0-degree angle of attack. Top plot corresponds to Mach 0.7, and bottom plot to 0.8 (PIV runs 1+2 and 3+4 in Table B.3).

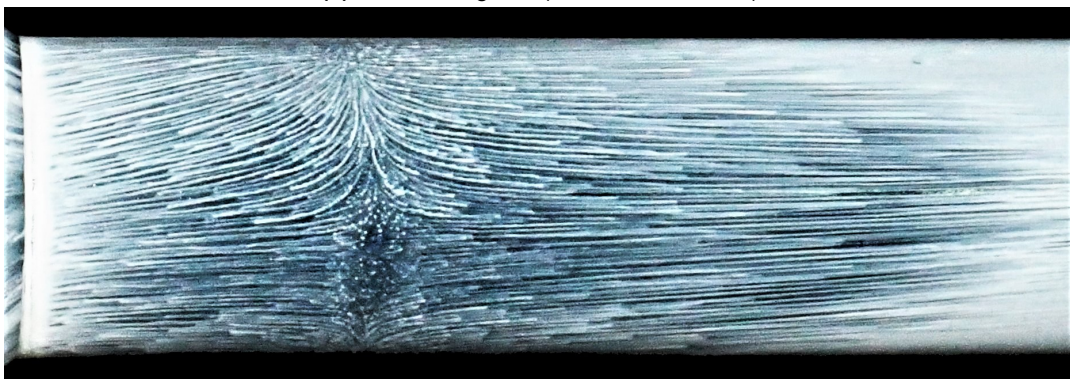
#### 4.4. Angle of Attack Effect

During the experimental campaigns, variations in the angle of attack were introduced to account for their potential influence on the vehicle's behaviour. It must be noted, that designers analysing launcher loads typically consider angle ranges spanning from  $-6$  to  $+6$  degrees [4]. This underscores the significance of accounting for angles, as even small deviations are pertinent due to the realistic inclination the vehicle encounters. In this study, two angles,  $0$  and  $4$  degrees, were chosen. There is no need to consider negative values as the model is axisymmetric. Moreover, the selected angles enable a meaningful comparison with earlier research conducted by Panda et al. [39], as the available shadowgraphy images from Panda's work pertain to a scenario with a  $4$ -degree angle of attack.

In an axisymmetric model, the natural symmetry of the design results in flow patterns that mirror the symmetry of the body itself. When angles of attack are introduced, this symmetry is disrupted, causing variations between the upper and lower regions of the body. This difference becomes particularly noticeable in the reattachment region, as observed in the oil flow visualisations for runs 30 and 28 (as detailed in Table B.1). These specific runs pertain to a benchmark scenario characterised by the bi-conic nose,  $34$ -degree boat-tail, a Mach number of  $0.8$ , and angle of attack values of  $0$  and  $4$  degrees.



(a) AoA = 0 degrees (run 30 at Table B.1)



(b) AoA = 4 degrees (run 28 at Table B.1)

**Figure 4.24:** Zoom into oil flow visualisation reattachment regions for benchmark case (Coe and Nute's model 11 [34]) at  $Ma = 0.8$  and angles of attack of  $0$  and  $4$  degrees.

Upon closer examination of this region in Figure 4.24, an apparent transformation is evident. The previously straight oil flow patterns observed at  $0$  degrees of angle of attack are replaced by curved trajectories when the model is inclined. This is explained by the fact that, in this case, the upper and lower portions of the model encounter flow from different surfaces due

to the loss of symmetry caused by inclination. As a result, reattachment occurs differently in these two parts, and when the flows converge on a common surface of the body, they no longer follow a straight path.

The PIV results indicate that the velocity jump encountered around the second wave location is bigger for the case with angle of attack. This is demonstrated by Figure 4.25, where lower velocity values are reached right after the second supersonic pocket for the 4-degree angle of attack case compared to the 0-degree one.

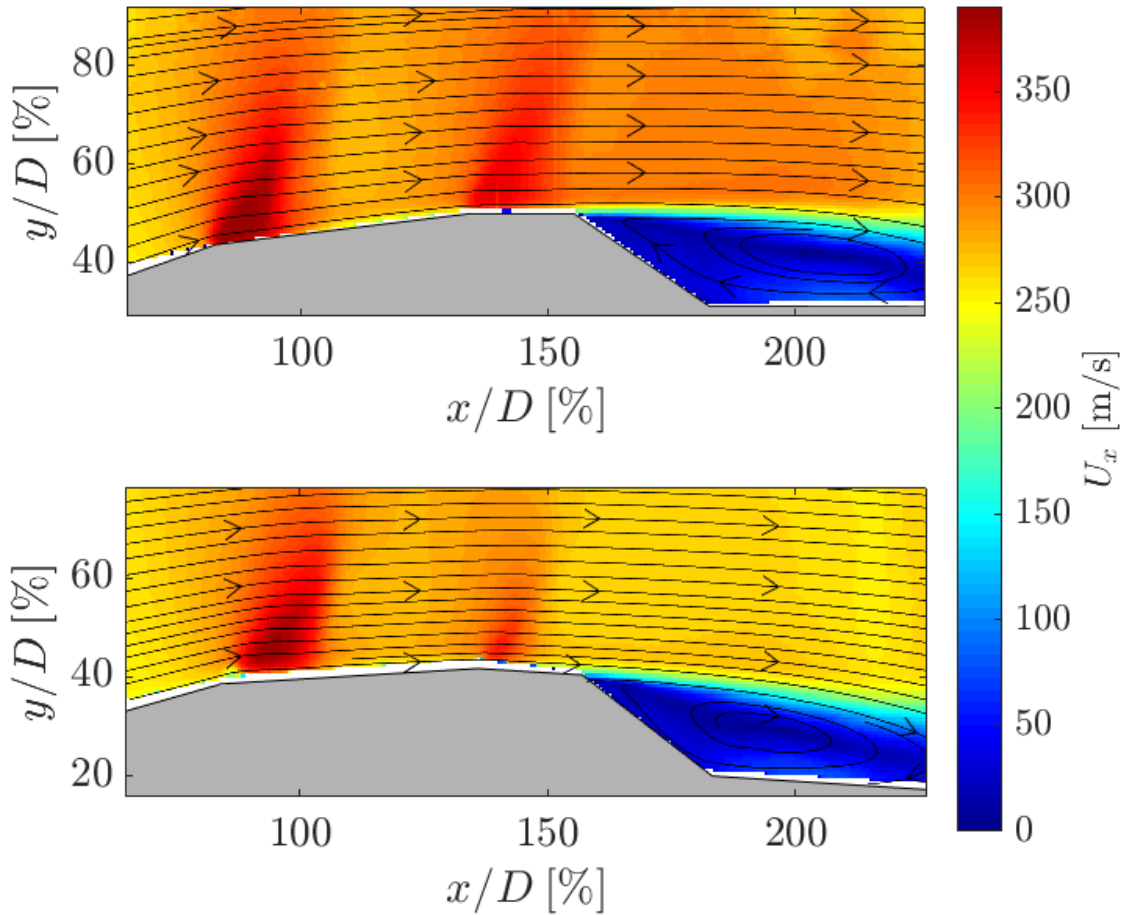
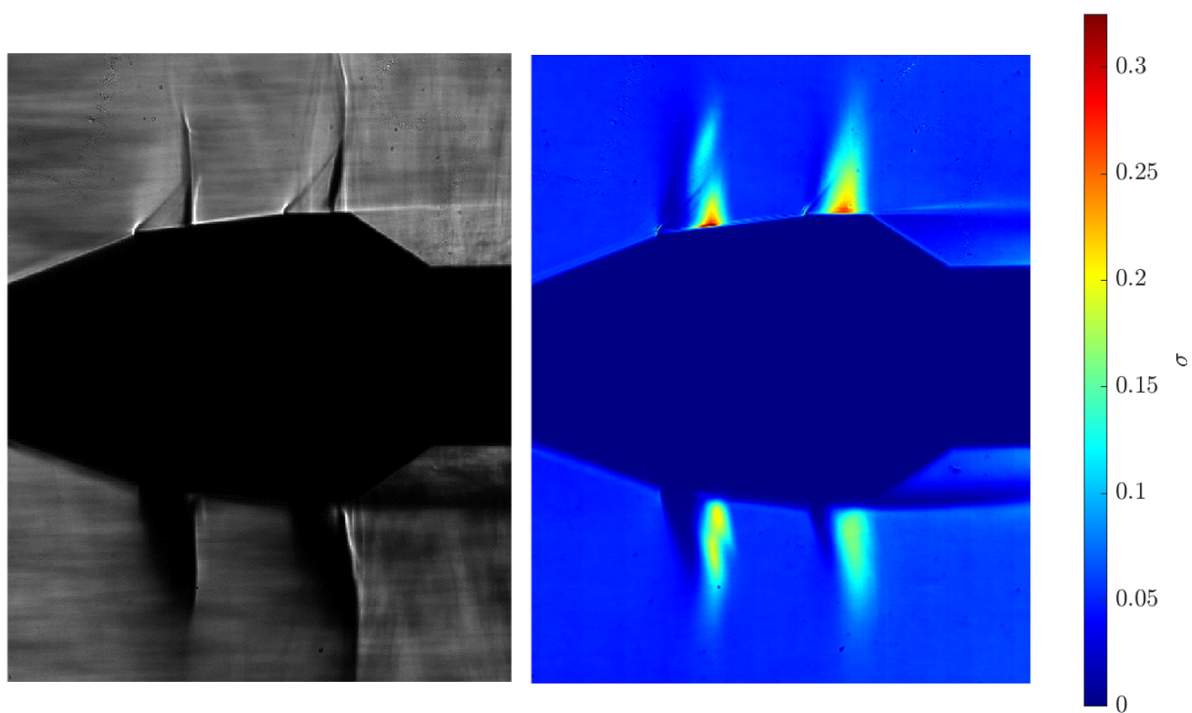
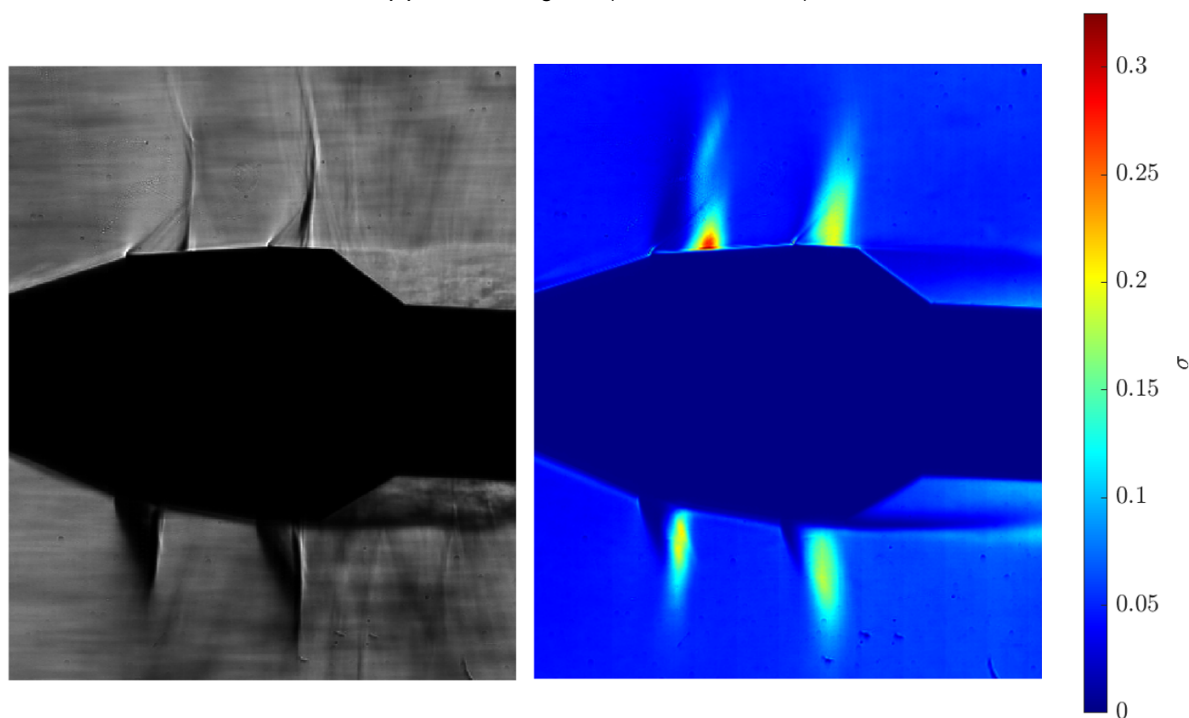


**Figure 4.25:** Horizontal velocity  $U_x$  average field for PIV runs with the benchmark configuration (BC34) at Mach 0.8. Top plot corresponds to 0-degree angle of attack, and bottom plot to 4-degree AoA (PIV runs 3+4 and 11+12 in Table B.3).

In contrast, the Schlieren results exhibit no substantial effects attributable to changes in the angle of attack. This assertion is substantiated by examining Figure 4.26, showcasing instantaneous images and pixel intensity standard deviations derived from the Schlieren images of runs 5 and 20 (as detailed in Table B.2). Those tests use the same configurations as the previously commented oil flow and PIV tests (refer to Figure 4.24 and Figure 4.25). Figure 4.26 shows an observable reduction in standard deviation along the upper section of the model when an angle of attack is introduced. This reduction implies a stabilization of shock waves. Nonetheless, it is important to acknowledge the possibility of minor experimental influences accounting for this distinction. Thus, the conclusion persists: minor inclinations appear to predominantly impact the detached region, thereby necessitating further experiments conducted at higher frequencies to attain conclusive insights.



(a) AoA = 0 degrees (run 5 at Table B.2)



(b) AoA = 4 degrees (run 20 at Table B.2)

**Figure 4.26:** Instantaneous schlieren picture and pixel intensity standard deviation from schlieren images for the benchmark case (Coe and Nute's model 11 [34]) at AoA = 0 and 4 degrees for Mach number of 0.8.

## 4.5. Shock Wave Spectral Analysis

As discussed in previous sections, the originated shock waves oscillate along the model. To gain a deeper understanding of these oscillations—whether they exhibit randomness or, in cases where multiple waves are present, if they synchronise in phase—an in-depth spectral analysis has been performed.

Before delving into the results of this analysis, it is crucial to understand how the locations of the shock waves evolve. This comprehension provides a rationale for the subsequent spectral analysis. Figure 4.28 provides a clear visualisation of how the positions of shock waves change over time, as the plot illustrates the evolution of a pixel line extracted from Schlieren images at a height encompassing the shock waves (refer to Figure 4.27 where the line is marked in red for BC34 at Mach number 0.8 and 0-degree angle of attack). The image is constructed using data from 500 consecutive instances. Notably, the enclosed area within the blue square at Figure 4.28 highlights two distinct regions characterised by fluctuations. These fluctuations directly correspond to variations in the position of the shock waves across the depicted instances.

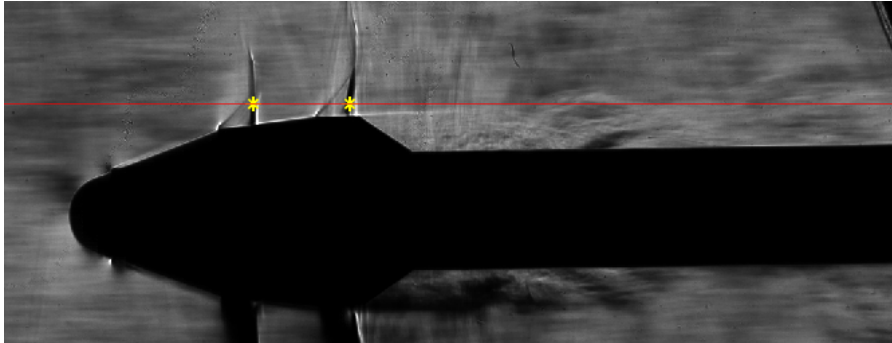


**Figure 4.27:** Zoom in to Schlieren instantaneous image for benchmark configuration (Coe and Nute’s model 11 [34] with bi-conic nose and 34-degree boat-tail) at 0-degree angle of attack and Mach 0.8 highlighting in red the pixel line represented along time in Figure 4.28, and in yellow the regions considered for the PSD curves (see Figure 4.29).

Table 4.2 presents the range within which the first two shock waves oscillate for all configurations tested in the Schlieren campaign. The results demonstrate that, as anticipated, the range of oscillation of the shock waves increases with the Mach number. This aligns with observations from the pixel intensity standard deviation fields extracted from the Schlieren images (refer to Figure 4.21), where the area with higher standard deviation, indicating shock wave oscillation, is wider for higher Mach numbers. For example, in the benchmark case (bi-conic nose and 34-degree boat-tail), the shock waves oscillate at 5 and 8% of the diameter  $D$  for Mach 0.7. These ranges increase to 20 and 22% for Mach 0.8.

Furthermore, as noted in earlier sections, the range of oscillation varies depending on the nose shape. At Mach 0.8, the conic nose exhibits a broader range at 31% (albeit with only one shock wave), while the ogive shows a range of 23%. This aligns with the discussion in subsection 4.2.1, which suggests that the conic nose induces greater unsteadiness. It is important to note that the main difference between ogive and bi-conic noses is that, although the ogive’s range appears slightly wider, only one shock wave exists.

Additionally, when considering the combined oscillation regions resulting from the appearance of an additional shock wave—occasionally merging with another shock wave for boat-tails at 5 and 15 degrees (as discussed in subsection 4.2.2)—only the range of the primary shock wave has been accounted. This range aligns with the oscillation observed for the 34-degree configuration.

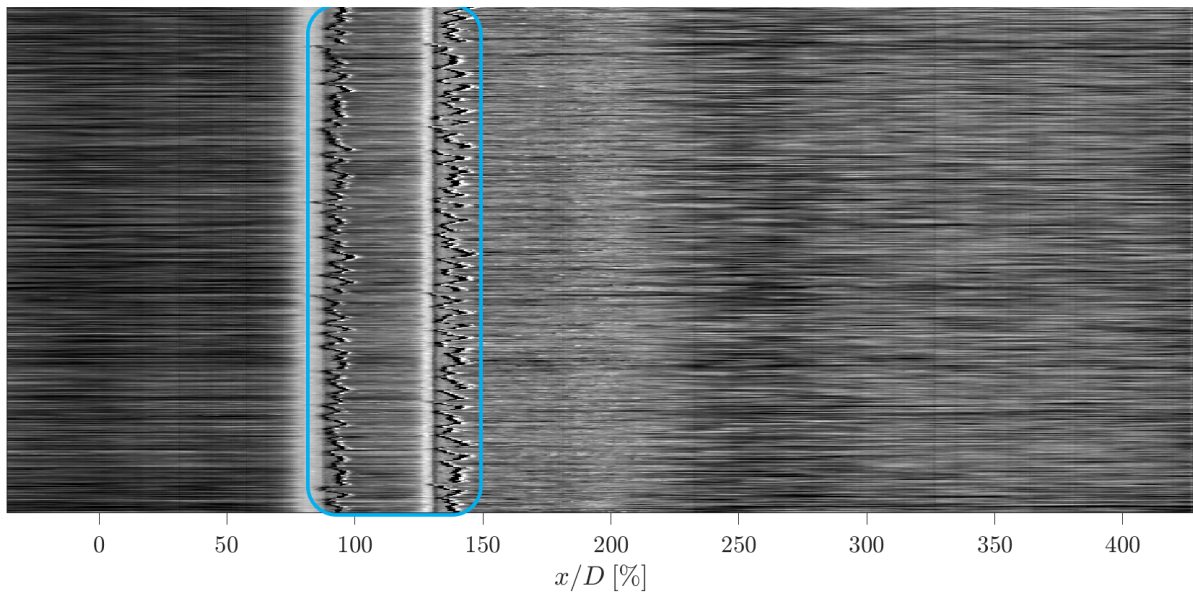


**Figure 4.28:** Selected pixel line (red line in Figure 4.27) along 500 timesteps for Schlieren run of the benchmark case (Coe and Nute's model 11 [34]) at  $Ma = 0.8$  and  $AoA = 0$  degrees (run 5 at Table B.2). In blue, highlighted the region where the shock waves location variation is observed.

**Table 4.2:** Shock wave average position for all tested configurations in the schlieren campaign. Numbers indicate the first two shock waves, with (1) representing the most upstream and (2) the subsequent shock wave. A hyphen (-) signifies the absence of an extracted value, indicating the non-discernibility or non-existence of a second shock wave.

Run	Nose	BT [deg]	Ma	AoA [deg]	$\bar{X}_{sw1}/D$ [%]	$\bar{X}_{sw2}/D$ [%]
2	BC	34	0.7	0	83±4	132±3
5	BC	34	0.8	0	92±10	139±11
6	BC	5	0.7	0	81±3	-
7	BC	5	0.8	0	91±9	148±18
8	BC	15	0.7	0	81±3	128±2
9	BC	15	0.8	0	91±11	148±18
10	C	34	0.7	0	133±5	-
11	C	34	0.8	0	146±16	-
12	SH	34	0.7	0	122±3	-
13	SH	34	0.8	0	141±12	-
14	SH	5	0.7	0	124±4	-
15	SH	5	0.8	0	146±16	-
16	SH	34	0.7	4	121±4	-
17	SH	34	0.8	4	141±12	-
19	BC	34	0.7	4	85±16	132±2
20	BC	34	0.8	4	88-109	144±10
21	BC	5	0.7	4	81-89	131±1
22	BC	5	0.8	4	88-107	150±18
23	BC	15	0.7	4	82-88	133±1
24	BC	15	0.8	4	90-106	149±14
25	C	34	0.7	4	138±6	-
26	C	34	0.8	4	152±11	-

To analyse the shock oscillation characteristics, a spectral analysis was conducted by assessing the Power Spectral Density (PSD), as elaborated in Section 3.6.1, utilising the Welch method [75]. Each PSD was then normalised based on its respective variance. The maximum resolved frequency is 2.5 kHz.

For the specific run mentioned earlier (Run 5 for bi-conic nose, 34-degree boat-tail, Mach 0.8 and 0-degree angle of attack), the PSD ( $P(f)$ ) is depicted in Figure 4.29, presented in pre-multiplied form ( $f \cdot P(f)$ ). The multiple curves correspond to data extracted from two distinct areas marked in yellow within Figure 4.27, in the two shock wave locations. For such a case, the analysis revealed a predominant peak at 427.25 Hz for the first shock wave and 852.05 Hz for the second. Notably, the peak frequency for the second shock wave is harmonically related to the frequency peak of the first shock wave.

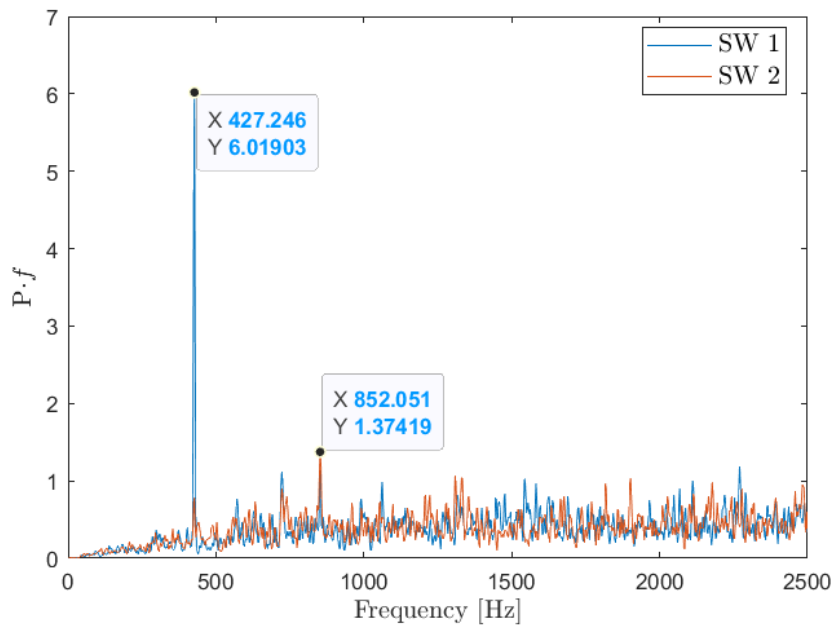


**Figure 4.29:** Power spectral density multiplied by frequency over frequency for selected pixels (see Figure 4.27 points in blue) along time from Schlieren test of the benchmark case (Coe and Nute's model 11 [34]) at Ma = 0.8 and AoA = 0 degrees (run 5 at Table B.2).

Summarised in Table 4.3 are the peak frequencies from the PSD for shock wave positions across each Schlieren run considered (as indicated in Table B.2). Across all cases, a consistent trend emerges, with the peak frequency consistently falling within two distinct ranges: 417-432 Hz and 832-864 Hz. Notably, the higher range is a harmonic of the lower one.

This prevalence of harmonic frequencies over the fundamental can be attributed to the extraction process of the PSD. A probe introduces some level of spurious data and amplifies harmonic effects. This is because there is inherent uncertainty regarding whether the probe is always precisely at the centre of the shock wave or not. This uncertainty amplifies the influence of the harmonic frequencies, either accentuating or diminishing its prominence relative to the fundamental frequency.

Solana [74] conducted experiments within the same wind tunnel (TST-27) utilised in this research. Specifically, the empty tunnel section was examined to decipher potential disturbances. His findings indicated noise propagation in the form of pressure waves downstream and upstream through the test section. Comparable phenomena were captured in the imagery acquired during this study. Solana's analysis of the empty section without the laser probe—

corresponding to the experimental setup of this Schlieren investigation—identified a primary frequency peak of 415 Hz. Notably, this peak’s amplitude seems scaled by the Mach number, mirroring the outcomes outlined in Table 4.3, where the  $f \cdot |P(f)|$  peak is similarly scaled with Mach.

In light of these findings, it is plausible to deduce that the inherent pressure waves predominantly influence the observed oscillations in the shock waves within this study in the wind tunnel environment. Consequently, differentiating whether the geometry-induced shock wave oscillations occur at a specific frequency remains inconclusive based solely on these results.

Notably, in cases where a third shock wave manifested, such as in run 9, the nearby region to that shock wave did not exhibit any discernible frequency peak.

Finally, in cases involving multiple shock waves, a cross-correlation analysis was conducted to evaluate variations in the locations of the first two shock waves. To do this, the same areas corresponding to the locations of the first and second shock waves (as previously indicated by the yellow markings in Figure 4.27) were considered.

The cross-correlation between pixel intensities over time for pixels close to each shock wave shows a very weak correlation. In future studies, it will be important to determine whether this low correlation is attributable to physical factors or it is influenced by the assessment of the signal at a point affected by pressure waves. To address this, the cross-correlation should be conducted at the precise location of the shock wave rather than at a fixed nearby pixel location.

**Table 4.3:** PSD peak frequencies on main shock wave positions for all tested configurations during Schlieren campaign. Numbers indicate the first two shock waves, with (1) representing the most upstream and (2) the subsequent shock wave. Hyphen (-) denotes the absence of an extracted value due to the non-discernibility or non-existence of a second shock wave.

Run	Nose	BT [deg]	Ma	AoA [deg]	$f_1$ [Hz]	$f_1 \cdot  P(f) $	$f_2$ [Hz]	$f_2 \cdot  P(f) $
2	BC	34	0.7	0	417.48	7.36	417.48	3.53
5	BC	34	0.8	0	427.25	6.02	852.05	1.37
6	BC	5	0.7	0	832.52	6.69	-	-
7	BC	5	0.8	0	424.81	8.05	424.81	2.47
8	BC	15	0.7	0	417.48	19.44	417.48	10.73
9	BC	15	0.8	0	427.25	18.18	427.25	7.27
10	C	34	0.7	0	422.36	9.80	-	-
11	C	34	0.8	0	432.13	14.64	-	-
12	SH	34	0.7	0	844.73	2.56	-	-
13	SH	34	0.8	0	864.26	1.68	-	-
14	SH	5	0.7	0	422.36	18.35	-	-
15	SH	5	0.8	0	429.69	3.13	-	-
16	SH	34	0.7	4	422.36	9.16	-	-
17	SH	34	0.8	4	429.69	7.78	-	-
19	BC	34	0.7	4	419.92	18.63	-	-
20	BC	34	0.8	4	429.69	4.83	859.38	1.72
21	BC	5	0.7	4	844.73	10.96	-	-
22	BC	5	0.8	4	427.25	6.23	-	-
23	BC	15	0.7	4	842.29	13.25	419.92	25.34
24	BC	15	0.8	4	429.69	5.53	429.69	4.51
25	C	34	0.7	4	419.92	15.79	-	-
26	C	34	0.8	4	424.81	2.65	-	-

## 4.6. Wake Reattachment Location

The boat-tail often leads to a significant phenomenon: the shear layer detachment. This, in turn, causes a recirculation region to form along the boat-tail. Following this recirculation area, there is a reattachment of airflow further downstream along the vehicle, as depicted in the PIV visualisation showing the average absolute velocity field within the boat-tail region for run 11 at Figure 4.4 (refer to Table B.3).

Understanding the specific scenarios in which recirculation occurs and pinpointing the exact location of reattachment is crucial due to its potential impact on the structure and overall system performance. This section presents the reattachment locations extracted from all cases studied using oil flow visualisation and PIV techniques.

Using the oil flow visualisation images (attached in Appendix C), the reattachment location ( $L$ ) relative to the boat-tail's start (at 76.8 mm from the model's leading edge, LE), as well as the extent of the reattachment region, termed  $w$ , have been quantified by taking as calibration reference the length of the PLF's main diameter (see Figure 4.30), denoted as  $D$  (50 mm). The extracted values are compiled in Table 4.4. The reattachment location is not a precise point but a region, justifying why  $w$  is computed.

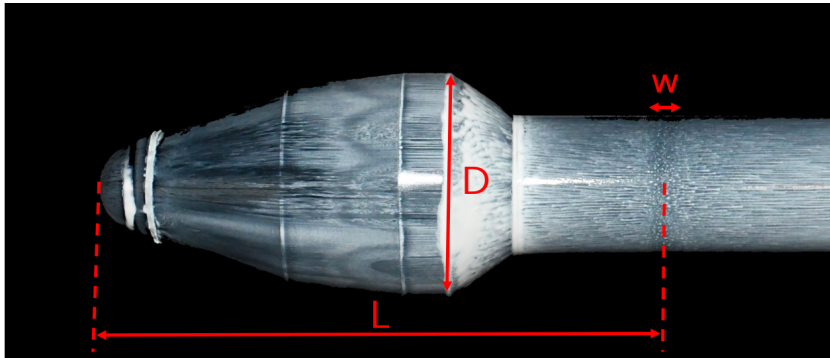


**Figure 4.30:** Reattachment location  $L$  and its width  $w$  determined from oil-flow image by using the PLF's diameter  $D = 50 \text{ mm}$ .

Reattachment is also observed in the PIV results, as demonstrated and discussed in Figure 4.4. Bi-colour graphs for each PIV case were made, which highlight positive and negative velocity components parallel to the model (see Figure 4.31). This visual representation effectively emphasises the region where the velocity reaches zero, indicating the flow reattachment point. It is worth noting that the associated measurement uncertainty averages around  $\pm 0.05 \text{ mm}$ , with a maximum of  $\pm 4 \text{ mm}$  in cases where the separation between data and the actual surface is most significant due to reflections during measurements.

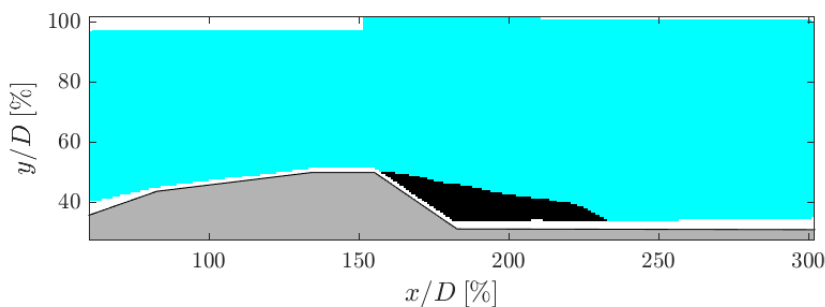


**Figure 4.31:** Bi-colour plot for PIV run 1 (refer to Table B.3) differentiating between positive (light blue) and negative (black) average horizontal velocity  $U_x$ .

The procedure outlined allows to obtain reattachment locations from the available particle image velocimetry runs (summarised in Table 4.4). However, there are two considerations to address when interpreting these results.

Firstly, the location is determined based on average fields derived from approximately 400 images in each configuration. Upon closer examination of individual instantaneous images instead of average fields, it becomes apparent that reattachment occurs at varying positions over time. For instance, in Figure 4.32, two instantaneous images are provided for the case of a bi-conic nose, 34-degree boat-tail, Mach 0.7, and 0 degrees angle of attack (runs 1 and 2 in Table B.3). These plots show different reattachment locations for the same configuration, demonstrating that rather than a single point, there exists a reattachment region. Therefore, the values extracted correspond to average positions.

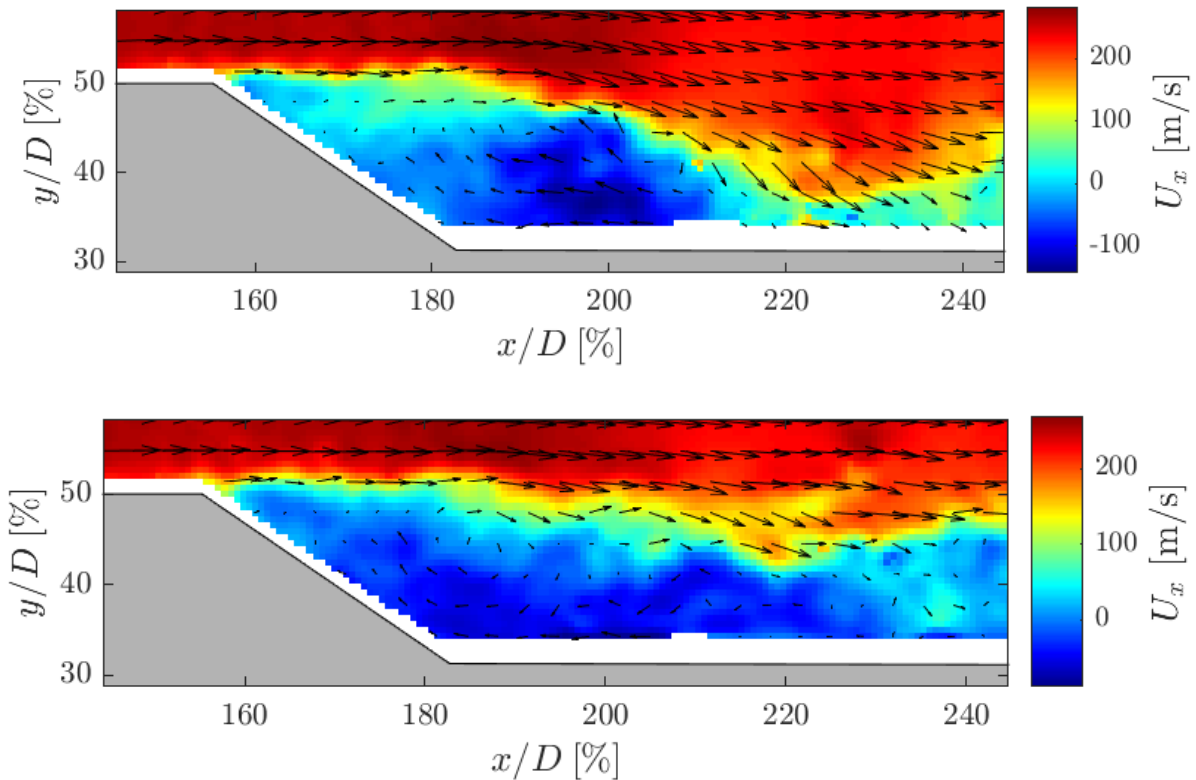


**Figure 4.32:** Instantaneous horizontal velocity  $U_x$  fields for PIV run 1 (refer to Table B.3) corresponding to bi-conic nose, 34-degree boat-tail, 0-degree angle of attack and Mach 0.7.

Secondly, in cases involving a 15-degree boat-tail configuration at Mach 0.7, there is no clear evidence of detachment in the average velocity fields. This contrasts with the same configuration at Mach 0.8, where distinct detachment and recirculation are observable in the corresponding average velocity fields (as seen in Figure 4.33, which provides a magnified view of the boat-tail region for the average fields of PIV cases 5+6 and 7+8).

Figure 4.34 presents the horizontal velocity standard deviation fields for BC15 at 0-degree angle of attack and Mach numbers of 0.7 and 0.8. The case for Mach 0.8 (Figure 4.34b) shows higher deviation, aligning with the average velocity field in Figure 4.33b, which shows complete detachment and recirculation in the boat-tail. In contrast, Figure 4.34a displays a lower standard deviation, consistent with the fully attached average flow from Figure 4.33a.

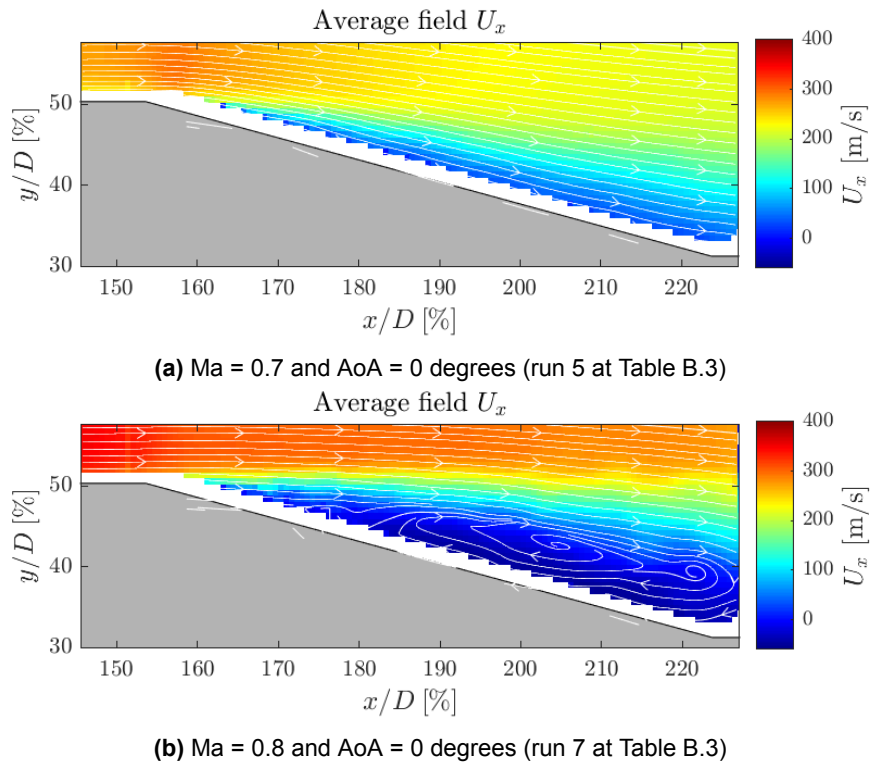


**Figure 4.33:** Average horizontal velocity  $U_x$  fields together with streamlines around boat-tail area for cases with bi-conic nose, 15-degree boat-tail and 0-degree angle of attack.

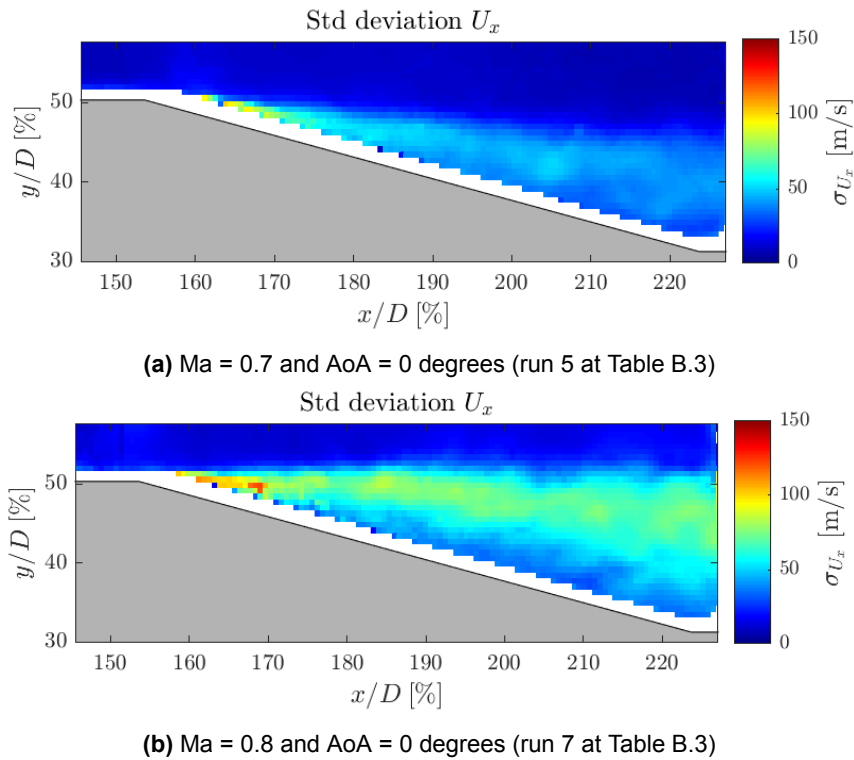


**Figure 4.34:** Standard deviation of the horizontal velocity  $\sigma_{U_x}$  fields around boat-tail area for cases with bi-conic nose, 15-degree boat-tail and 0-degree angle of attack.

This stands in contrast to what is observed in instantaneous images, where instances of detachment become apparent in the 15-degree boat-tail cases at Mach 0.7 (refer to Figure 4.35). It is important to note that this detachment is not a constant state throughout the entire flow; rather, the flow periodically reattaches during specific time intervals. For a clearer understanding of these occurrences, Figure 4.36 illustrates the percentage of instances with reverse flow in each pixel, relative to the total number of available images, for PIV runs 5+6 and 13 (see Table B.3).

From the plots in Figure 4.36, two observations can be made. Firstly, the percentage of occurrences and the area characterised by sporadic reverse flow are higher when considering a non-zero angle of attack. Secondly, in both cases, this reverse flow phenomenon does not manifest for all instances; it reaches a peak of around 50% for the 4-degree angle of attack and approximately 20% for the run without any angle of attack. These findings elucidate why detachment is not discernible in the average flow field.

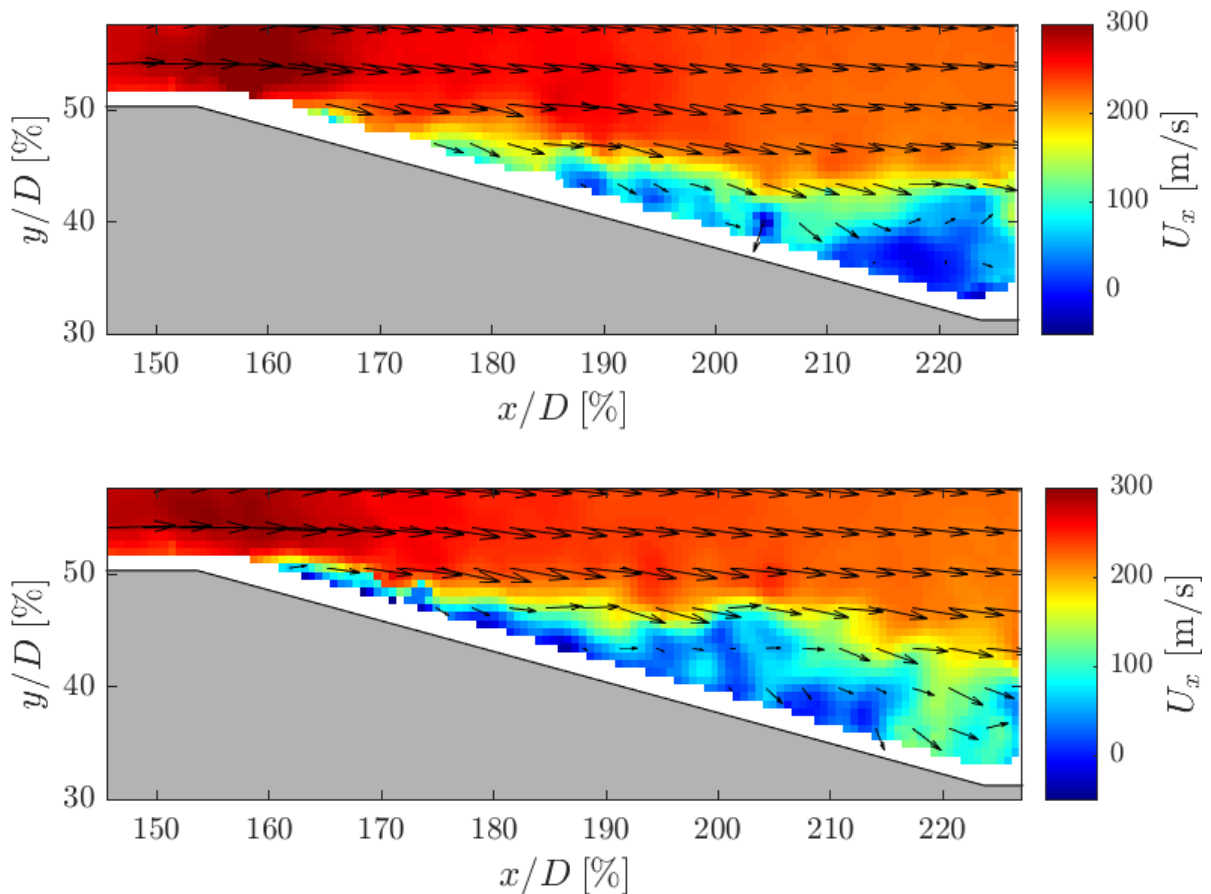


**Figure 4.35:** Instantaneous horizontal-velocity  $U_x$  together with vector fields for PIV run 5 (refer to Table B.3) corresponding to bi-conic nose, 15-degree boat-tail, 0-degree angle of attack and Mach 0.7.

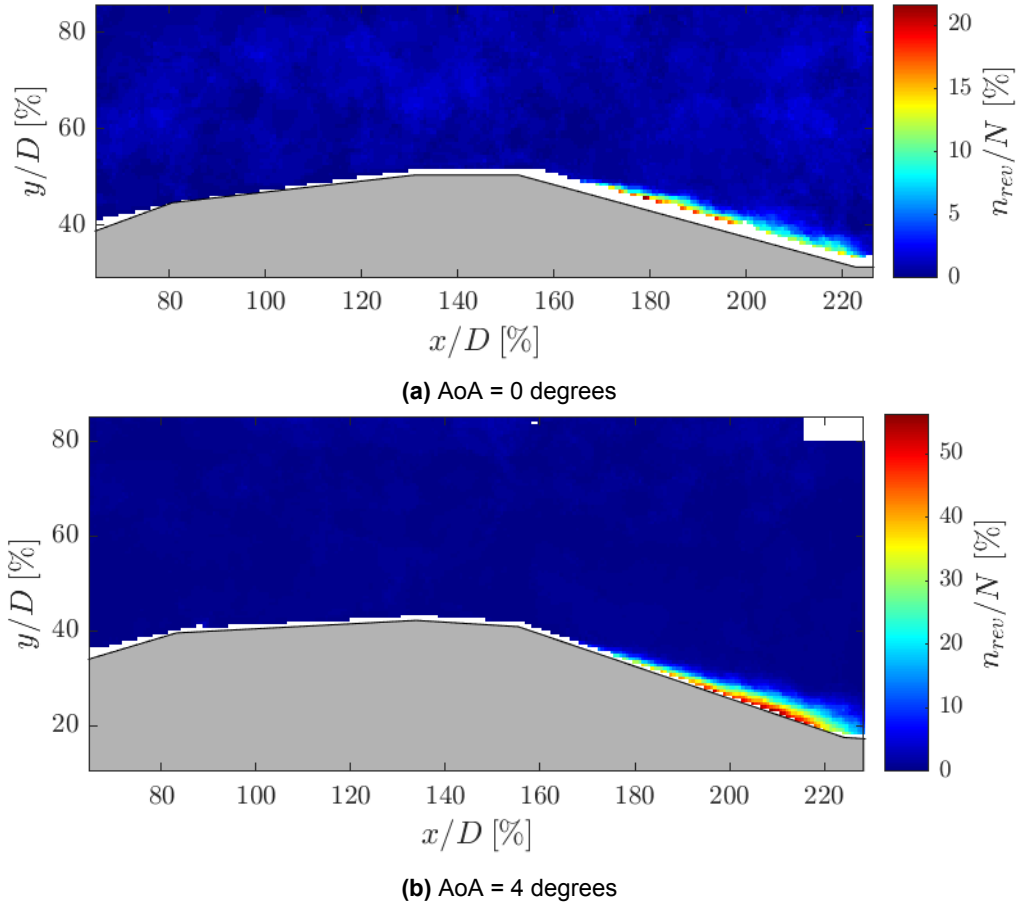


**Figure 4.36:** Number of times each velocity vector had reverse flow over the total number of images for PIV cases tested at Mach 0.7 and boat-tail of 15 degrees (runs 5 and 13 at Table B.3).

While it can be stated that reattachment introduces unsteadiness to the structural load due to the impact of the flow and the variation along time of the reattachment point, no further discernible conclusions can be drawn from the data at hand.

Table 4.4 compiles the computed parameters for all conducted OF visualisations and PIV runs (as displayed in Tables B.1 and B.3) using the described methodology. In all cases, the compiled reattachment locations have been measured from the boat-tail start or the “edge of the step” to facilitate comparison with studies involving BFS (refer to Figure 2.1.2), as this is the customary convention for measuring reattachment distance.

In previous studies focused on axisymmetric BFS, which differ from the boat-tails examined in this study due to their 90-degree step configuration, the reattachment location is non-dimensionalised using either the step height,  $h$ , or the diameter,  $D$ . Here, the same has been done so that comparison with two-dimensional studies could be made. In this case,  $h$  corresponds to the difference between the two diameters, which is 18.75 mm as the diameter ratio  $D/d$  is 1.6 (equivalent to  $d/D$  of 0.625), as indicated in section 3.2.

The results in Table 4.4 show that reattachment occurs at distances ranging from 0.8 to 1.3 times  $D$ , equivalent to 2-4 times the step height. These findings closely align with those reported by Schrijer et al. [58], who observed reattachment at approximately 3.0 times  $h$ , and Hudy et al. [76], who reported values of  $L/h$  between 4.2 and 5. Although Gentile et al. [77] investigated various afterbody diameters, none of their configurations precisely matched the present case with  $d/D = 0.625$  and  $h/D = 0.375$ . Nonetheless, their findings indicated a reattachment location of approximately  $0.8D$  for  $d/D$  of 0.6 and  $h/D$  of 0.2, and over  $1D$

**Table 4.4:** Parameters characterising the reattachment region (distance  $L$  and width  $w$ ) obtained from both oil flow (OF) and PIV runs, denoted as  $R_{OF}$  and  $R_{PIV}$  respectively (same numbering as in Tables B.1 and B.3). Nose configurations are identified by BC (bi-conic), C (conic), and SH (Sears-Haack or ogive). PIV runs with the same configuration are combined for statistical reliability. Hyphen - indicates no extracted value, signifying either the absence of the run or no reattachment.

Nose	BT [deg]	Ma	AoA[deg]	$R_{OF}$	$L_{OF}/D$	$w_{OF}/D$	$R_{PIV}$	$L_{PIV}/D$
BC	34	0.7	0	3	1.04	0.10	1+2	0.79
				29	0.88	0.10		
				34	0.92	0.06		
BC	34	0.8	0	30	0.94	0.14	3+4	0.79
SH	34	0.8	0	31	0.92	0.10	-	-
C	34	0.8	0	32	1.32	0.08	-	-
BC	34	0.7	4	27	0.90	0.12	-	-
BC	34	0.8	4	28	1.04	0.08	11+12	0.86
BC	15	0.7	0	-	-	-	5+6	-
BC	15	0.8	0	-	-	-	7+8	0.86
BC	15	0.7	4	-	-	-	13	-
BC	15	0.8	4	-	-	-	15+16	0.78

for  $d/D$  of 0.4 and  $h/D$  of 0.3. These results lie within the range of the data presented in Table 4.4.

In cases where oil flow and PIV results were available to determine the reattachment location, discrepancies exist between the outcomes. Nevertheless, these differences diminish when accounting for the associated uncertainties. The uncertainty in the oil flow results is reflected in the width of the reattachment zone (see Table 4.4). Additionally, there is an uncertainty in the data extracted from PIV, which is only noteworthy for runs 3+4 and 7+8, where it reaches  $\pm 4$  mm. For the remaining cases, it is below  $\pm 0.05$  mm and can be considered negligible.

The most downstream reattachment is observed for the conic nose configuration. This observation aligns with the findings discussed in previous sections, as this geometry seems to enhance a stronger shock wave, resulting in higher unsteadiness in the detached region and an extended length required for the flow reattachment. In contrast, the bi-conic shape seems to mitigate such shock wave strength with the pre-separation region at the shoulder, as stated by Ericsson [32]. This allows for earlier reattachment, occurring at similar distances as observed with the ogive shape.



# 5

## Conclusions and Future Work

*Research is seeing what everybody else has seen  
and thinking what nobody else has thought.*

Albert Szent-Györgyi

In this project, an extensive experimental study was conducted to investigate the aerodynamics of hammerhead payload configurations within the transonic regime. The primary objective was to analyse the aerodynamic flow patterns influenced by various geometric parameters, such as nose and boat-tail shapes, in conjunction with different Mach numbers and angles of attack.

To achieve this goal, a three-part experimental approach was employed. An experimental campaign encompassing all potential geometry combinations was initially executed using Schlieren visualisation. This phase aimed to uncover the effects of Mach number, angle of attack, boat-tail, and nose shapes on flow dynamics. Concurrently, a complementary oil flow visualisation campaign was carried out on specific configurations to provide a more comprehensive understanding of overall flow patterns. This approach extended beyond the capabilities of Schlieren visualisation, revealing details like reattachment locations. Subsequently, the final campaign utilised Particle Image Velocimetry (PIV) to deepen insights into phenomena such as recirculation and reattachment. This technique not only built upon observations from previous campaigns but also added new perspectives.

Upon examining the overall flow field of the benchmark case (referred to as Coe and Nute's model 11 [34]), it became evident that the transonic flow patterns typical of hammerhead configurations, such as expansion fans in geometric transitions preceding shock waves, were indeed present. However, comparing the Schlieren imagery results from this study and Panda's shadowgraphy images [39] raised a noteworthy consideration regarding potential blockage effects during the current research. This inference was based on the closer resemblance between this study results at Mach 0.8 and Panda's images at 0.85 than with Panda's at Mach 0.8.

### Geometry, Mach Number and Angle of Attack Effects

Concerning the effects of different nose shapes, the conic nose induced the highest shock wave oscillations. In contrast, the bi-conic nose introduced an additional shock wave compared to the conic and ogive noses. This behaviour was attributed to the bi-conic shoulder and the conic-cylinder transition, which, as stated by Ericsson [32], enhances a pre-separation of the flow compared to conic noses. Using the bi-conic nose altered flow detachment behaviour, making it contingent on the boat-tail angle rather than an inherent detachment from the shock

wave, as observed in the conic case. Overall, the shock wave for the conic nose is more energetic than in the other configurations, as it presents more oscillations and curves the detached shear layer.

Regarding the influence of the boat-tail, the five and 15-degree cases introduced an extra shock wave that interacted with the shock wave arising from the conic-cylinder transition, occasionally merging. This interaction expanded the region with a high pixel intensity standard deviation (extracted from the 5457 schlieren images taken per run), implying that the interaction with the boat-tail region expands. Such widening of the region where the shock waves oscillate results, for sure, in higher unsteadiness, as shock wave-boundary layer interaction also increases. However, as shock wave oscillation is not the only possible unsteadiness source, further tests are required to determine which geometry produces more unsteady loads.

Cross-comparing the effects of nose and boat-tail revealed their independent impacts. Altering the nose shape while keeping the boat-tail constant, or vice versa, resulted in similar effects on flow dynamics.

As for the other assessed parameters, raising the Mach number heightened shock wave oscillations and size and flow detachment. On the other hand, the angle of attack disrupts model symmetry, mainly affecting the oil patterns around reattachment, as indicated by flow curvature for the 4-degree angle of attack cases compared to 0-degree ones.

### Shock Wave Location and Spectral Analysis

Selecting probes near the shock waves in the schlieren images allowed to evaluate how the shock wave location changes and to perform a spectral analysis from such variations. As the Mach number increased, there was a corresponding expansion in the range of shock wave locations. This aligns with the previously noted trend of stronger shock waves at higher Mach numbers. Furthermore, the results affirm that the conic nose exhibits greater unsteadiness due to oscillations in the shock waves compared to the other geometries, with a range of 31% the diameter  $D$ , over the 23% variation for the ogive nose at Mach 0.8 and 0-degree angle of attack, for example.

Examining shock wave spectral characteristics revealed peak frequencies in the 417-432 Hz range or at the harmonic range between 832-864 Hz. These values closely match the 415 Hz peak frequency observed by Solana [74] during experiments at the TST-27 (same facility used in this study) due to inherent pressure waves. Therefore, the results suggest a potential influence of the pressure waves on the shock wave oscillatory behaviour. However, low correlation values were obtained when performing a cross-correlation of probes near the two primary shock wave positions.

### Wake Reattachment

When examining flow detachment and wake reattachment locations through both oil flow visualisation and PIV results, a consistent pattern emerged across all tested cases except for those with a 15-degree boat-tail at Mach 0.7, where the average field did not exhibit signs of detachment. Upon closer examination of individual PIV images, though, intermittent detachment was identified. Specifically, regions of reverse flow were observed in approximately 20 and 50% of the roughly 400 PIV images analysed for the 0 and 4-degree angle of attack cases, respectively.

Regarding wake reattachment locations, the results in all cases closely align with prior studies on axisymmetric BFS. It is important to note that this holds despite the difference in boat-tail angle, as backward-facing steps correspond to a 90-degree configuration, not tested in the current study.

Furthermore, these findings support the idea that the conic nose generates stronger shock waves. In cases with a conic nose, reattachment occurred further downstream compared to

the other nose configurations, where reattachment points were relatively proximate to each other. This observation lends weight to Ericsson's assertion [32] that the pre-separation in the bi-conic shoulder allows for a more sustained flow attachment in bi-conic noses compared to conic geometries.

While no distinct phenomena specifically tied to reattachment were identified, a consistent variation in the reattachment point over time was discerned.

## 5.1. Design Recommendations

The conclusions drawn from this study offer valuable design insights. Boat-tails set at five and 15-degree angles have been observed to broaden the range of shock wave oscillations, introducing an additional shock wave that may merge with existing ones. While precise quantification of the increase in unsteadiness remains a subject for further investigation, it is clear that configurations involving sensitive payloads should approach such designs with caution due to the potential operational complications arising from their unpredictable oscillations. The presence of an additional shock wave, a propagating disturbance characterised by energy fluctuations in pressure increases followed by abrupt decreases, inherently introduces unsteadiness. This is generally preferred to be avoided, as it brings additional pressure loads, vibrations from the oscillations, and shear loads.

Further comprehensive studies are necessary to determine whether the 34-degree configuration would lead to more or less loads in the area compared to 5 and 15-degree angles. However, considering that fairing's design always aims to maximise payload, for which a 90-degree boat-tail would be ideal, and that the solutions with better results seem to be boat-tails with five and 34 degrees, this last solution seems, with the current results, the best balance between payload optimisation and loads reduction.

Additionally, the choice of nose significantly impacts stability. It is advised to steer away from the conic nose design for stability reasons. Instead, the selection between bi-conic and ogive nose designs should be based on considerations of unsteady loads and manufacturing precision, as deviations in manufacturing ogive shapes can lead to significant variations (refer to subsection 2.2.1). This underscores the importance of future research in accurately quantifying the implications of these design choices. Still, bi-conic noses seem the safest option in terms of manufacturing and phenomena observed, followed by boat-tails with angles around 34 degrees.

## 5.2. Future Work

Several avenues for future research are identified to enhance the current understanding:

- **Unsteady Loads:** Future investigations should focus on quantifying the unsteady loads present along the nose and shock wave locations and their interaction with the boat-tail region. This would enable a more accurate evaluation of the impact of nose and boat-tail design on unsteadiness, particularly in scenarios involving sensitive payloads.
- **CFD Validation and Insight Enhancement:** The integration of Computational Fluid Dynamics (CFD) studies, replicating the experimental conditions, is recommended. This approach would validate the experimental findings and provide a more nuanced understanding of the aerodynamic behaviours, such as blockage effects.
- **Shock Wave Oscillation:** The shock wave positions should be precisely detected so that the specific oscillation range and a proper cross-correlation between their movements can be made. This would allow to discern if the current low correlation values are due to the physics of the shock waves or due to other effects.

- **Effect of Cylindrical Section Length:** Given that many industry payload launchers feature extended cylindrical sections, future research should explore the implications of varying cylindrical section lengths on aerodynamic behaviour.

To conclude, future research efforts should focus on CFD validation, a more accurate assessment of nose design effects, and the investigation of extended cylindrical sections. These endeavours are expected to refine the understanding of hammerhead payload configurations and contribute significantly to this field.

# References

- [1] Arianespace SA. *VEGA C User's Manual*. May 2018. url: [https://www.arianespace.com/wp-content/uploads/2018/07/Vega-C-user-manual-Issue-0-Revision-0\\_20180705.pdf](https://www.arianespace.com/wp-content/uploads/2018/07/Vega-C-user-manual-Issue-0-Revision-0_20180705.pdf) (visited on 01/18/2023).
- [2] SpaceX. *Falcon User's Guide*. SpaceX. Sept. 2021. 88 pp. url: <https://www.spacex.com/media/falcon-users-guide-2021-09.pdf> (visited on 01/18/2023).
- [3] J.G. de Medeiros, A.C. Avelar, and J.B.P. Falcão Filho. "Experimental Study of Geometric Variations Effect on the Flow Patterns on a Hammerhead Satellite Launch Vehicle". In: *Proc. 30th Congress of the International Council of the Aeronautical Sciences*. International Council of the Aeronautical Sciences. Sept. 2016.
- [4] B.N. Suresh and K. Sivan. *Integrated design for space transportation system*. Springer, 2015.
- [5] J.D. Anderson. *Fundamentals of Aerodynamics*. New York: McGraw-Hill, 2009.
- [6] R. C. Mehta. "Computational Fluid Dynamics Analysis and Design of Payload Shroud of Satellite Launch Vehicle". In: *Sch J Eng Tech* 4 (2022), pp. 16–34.
- [7] L.E. Ericsson. "Aeroelastic instability caused by slender payloads." In: *Journal of Spacecraft and Rockets* 4.1 (1967), pp. 65–73.
- [8] D.M. Driver, H.L. Seegmiller, and J.G. Marvin. "Time-dependent behavior of a reattaching shear layer". In: *AIAA journal* 25.7 (1987), pp. 914–919.
- [9] H. Babinsky and J.K. Harvey. *Shock wave-boundary-layer interactions*. Vol. 32. Cambridge University Press, 2011.
- [10] J. Délery and J.P. Dussauge. "Some physical aspects of shock wave/boundary layer interactions". In: *Shock waves* 19.6 (2009), pp. 453–468.
- [11] W. Hu. "Dynamics of a supersonic flow over a backward/forward-facing step". In: (2020).
- [12] Y. Kim et al. "Prediction of Pressure Fluctuations on Hammerhead Vehicle at Transonic Speeds Using CFD and Semi-empirical Formula Considering Spatial Distribution". In: *Journal of the Korean Society for Aeronautical & Space Sciences* 49.6 (2021), pp. 457–464.
- [13] R. Kumar, P. R. Viswanath, and A. Prabhu. "Mean and fluctuating pressure field in boat-tail separated flows at transonic speeds". In: *39th Aerospace Sciences Meeting and Exhibit*. 2001. doi: 10.2514/6.2001-582. url: <https://arc.aiaa.org/doi/10.2514/6.2001-582>.
- [14] H.A. Cole, A.L. Erickson, and A.G. Rainey. *Buffeting during atmospheric ascent - Space vehicle design criteria/structures*. Tech. rep. NASA SP-8001. Nov. 1970.
- [15] B.T.C. Zandbergen. *Lecture notes in Rocket Design Details for AE1222-II Aerospace Design & Systems Engineering Elements I - Part Launch Vehicle Design and Sizing*. TU Delft Faculteit Luchtvaart- en Ruimtevaarttechniek, Nov. 2022.
- [16] C.F. Coe. *The effects of some variations in launch-vehicle nose shape on steady and fluctuating pressures at transonic speeds*. NASA-TM-X-646. National Aeronautics and Space Administration, 1962.

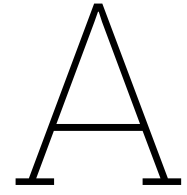
- [17] J.B. Dods Jr and C.F. Coe. *Crossflow effects on steady and fluctuating pressures on an ogive-cylinder cone-frustum model in supersonic separated flow*. Tech. rep. 1981.
- [18] A.G. Rainey. "Progress on the launch-vehicle buffeting problem". In: *Journal of Spacecraft and Rockets* 2.3 (1965), pp. 289–299.
- [19] F.F.J. Schrijer et al. "Experimental investigation of base flow buffeting on the Ariane 5 launcher using high speed PIV". In: *7th European Aerothermodynamics Symposium on Space Vehicles*. Vol. 692. 2011, p. 103.
- [20] M. Ozair and M.N. Qureshi. "Numerical Prediction of Aeroacoustic Loads on a Hammerhead Nose Cone Configuration". In: *2019 16th International Bhurban Conference on Applied Sciences and Technology (IBCAST)*. IEEE. 2019, pp. 806–810.
- [21] J.S. Andrews. "Effects of transonic buffeting on a hammerhead-shaped payload." In: *Journal of Spacecraft and Rockets* 3.8 (1966), pp. 1285–1291.
- [22] R. Camussi et al. "Wall pressure fluctuations induced by transonic boundary layers on a launcher model". In: *Aerospace Science and Technology* 11.5 (2007), pp. 349–359. issn: 12709638. doi: 10.1016/j.ast.2007.01.004.
- [23] B. Imperatore et al. "Aeroacoustic of the VEGA Launcher: Wind Tunnel Tests and Full Scale Extrapolations". In: *11th AIAA/CEAS Aeroacoustics Conference*. 2005, p. 2913.
- [24] Y. Liu et al. "Numerical analysis of transonic buffet flow around a hammerhead payload fairing". In: *Aerospace Science and Technology* 84 (2019), pp. 604–619.
- [25] J. Panda. "Aeroacoustics of space vehicles". In: *Stanford Fluid Mechanics Seminar*. ARC-E-DAA-TN12911. 2014.
- [26] B. Troclet and M. Depuydt. "Experience learned from ARIANE 5 wind tunnel tests regarding aerodynamic noise on upper part and buffeting loads on rear part". In: *The 29th Internal Conference and Exhibition on Noise Control Engineering*. 2000, pp. 27–20.
- [27] M.G. Chae, S.H. Park, and J.S. Bae. "Analysis of Numerical Factors Affecting the Simulation of Pressure Perturbation around a Hammerhead Launch Vehicle". In: *Journal of Computational Fluids Engineering* 22.2 (2017), pp. 59–65.
- [28] P.R. Spalart et al. "Comments on the feasibility of LES for wings, and on hybrid RAN-S/LES approach, advances in DNS/LES". In: *Proceedings of 1st AFOSR International Conference on DNS/LES, 1997*. 1997.
- [29] S.M. Murman and L. Diosady. "Simulation of a hammerhead payload fairing in the transonic regime". In: *54th AIAA Aerospace Sciences Meeting*. 2016, p. 1548.
- [30] R. Camussi et al. "Wind tunnel measurements of the surface pressure fluctuations on the new VEGA-C space launcher". In: *Aerospace Science and Technology* 99 (2020), p. 105772.
- [31] S.M. Murman, L.T. Diosady, and P.J. Blonigan. "Comparison of transonic buffet simulations with unsteady PSP measurements for a hammerhead payload fairing". In: *55th AIAA Aerospace Sciences Meeting*. 2017, p. 1404.
- [32] L.E. Ericsson. "Hammerhead wake effects on elastic vehicle dynamics". In: *Journal of spacecraft and rockets* 34.2 (1997), pp. 145–151.
- [33] P.W. Hanson. *Wind Tunnel Measurements of Aerodynamic Damping Derivatives of a Launch Vehicle Vibrating in Free-free Bending Modes at Mach Numbers from 0.70 to 2.87 and Comparisons with Theory*. NASA TNF-1391. National Aeronautics and Space Administration, Oct. 1962.

- [34] C.F. Coe and J.B. Nute. *Steady and fluctuating pressures at transonic speeds on hammerhead launch vehicles*. Tech. rep. NASA TM X-778. Aug. 1962.
- [35] L.E. Ericsson and N.J. French. *The aeroelastic characteristics of the Saturn IB SA-203 launch vehicle*. Tech. rep. NASA CR-76563. Apr. 1966.
- [36] A. Chaphalkar et al. “Multi-Objective Optimization of Ogive Payload Fairing for a Launch Vehicle”. In: Nov. 2021.
- [37] A. Sachdeva, M. Singh Malik, and P. Priyadarshi. “Boat-tail Shape Optimization Studies for a Payload Fairing”. In: *Symposium on Applied Aerodynamics and Design of Aerospace Vehicle (SAROD 2015)*. Dec. 2015.
- [38] K. Sunil, I. Johri, and P. Priyadarshi. “Aerodynamic Shape Optimization of Payload Fairing Boat Tail for Various Diameter Ratios”. In: *Journal of Spacecraft and Rockets* 59.4 (2022), pp. 1–14.
- [39] J. Panda et al. “Unsteady pressure fluctuations measured on a hammerhead space vehicle and comparison with Coe and Nute’s 1962 data”. In: *International Journal of Aeroacoustics* 17 (1-2 Mar. 2018), pp. 70–87. issn: 20484003. doi: 10.1177/1475472X17743626.
- [40] Agência Espacial Brasileira. *Programa Espacial Brasileiro: Transporte Espacial VLS-1*. 2020. url: <https://www.gov.br/aeb/pt-br/programa-espacial-brasileiro/transporte-espacial/vls-1> (visited on 01/18/2023).
- [41] S.R. Cole and T.L. Henning. “Buffet response of a hammerhead launch vehicle wind-tunnel model”. In: *Journal of Spacecraft and Rockets* 29.3 (1992), pp. 379–385.
- [42] P. Catalano et al. “CFD contribution to the aerodynamic data set of the Vega launcher”. In: *Journal of Spacecraft and Rockets* 44.1 (2007), pp. 42–51.
- [43] A. Nicoli et al. “Wind Tunnel Tests and Ground-to-flight Extrapolation of the Vega Launcher Aerodynamics”. In: *XVIII Congresso Nazionale AIDAA* (Sept. 2005).
- [44] A. Nicoli et al. “Wind tunnel test campaigns of the VEGA launcher”. In: *44th AIAA Aerospace Sciences Meeting and Exhibit*. 2006, p. 257.
- [45] P.L. Vitagliano et al. “Aerodynamic Characterisation of Vega-C Launcher”. In: *XXV International Congress of the Italian Association of Aeronautics and Astronautics*. Sept. 2019.
- [46] R. C. Mehta. “Drag reduction for payload fairing of satellite launch vehicle with aerospike in transonic and low supersonic speeds”. In: *Advances in Aircraft and Spacecraft Science* 7 (4 July 2020), pp. 371–385. issn: 22875271. doi: 10.12989/aas.2020.7.4.371.
- [47] R.C. Robinson. *A Wind-Tunnel Investigation of the Dynamic Stability of Axisymmetric Models with Hammerhead Noses in Transonic Flow*. NASA Ames Research Center, Apr. 1963. url: <https://ntrs.nasa.gov/citations/19660029075>.
- [48] F. Scarano. “Overview of PIV in supersonic flows”. In: *Particle Image Velocimetry: New Developments and Recent Applications* (2008), pp. 445–463.
- [49] M. Raffel et al. “Experimental aspects of PIV measurements of transonic flow fields and their benefit for the optimization of gas turbines”. In: *Proc. Eighth International Symposium on Applications of Laser Techniques to Fluid Mechanics*. 1996, pp. 28–1.
- [50] A. D’Aguanno. “Physics and Control of Transonic Buffet”. PhD thesis. Delft, the Netherlands, Jan. 2023.

- [51] F.F.J. Schrijer, R. Solana Perez, and B.W. van Oudheusden. "Investigation of transonic buffet using high speed PIV". In: *Proceedings of the 5th International Conference on Experimental Fluid Mechanics (ICEFM 2018)*. 2018.
- [52] K. Hannemann et al. "Launch vehicle base buffeting-recent experimental and numerical investigations". In: *7th European Aerothermodynamics Symposium on Space Vehicles*. Vol. 692. 2011, p. 102.
- [53] S. Koike, K. Nakakita, and S. Tsutsumi. "Particle Image Velocimetry for Transonic Unsteady Flow Field around a Rocket Fairing Model". In: *54th AIAA Aerospace Sciences Meeting*. 2016, p. 0027.
- [54] TU Delft. *TST-27 Transonic/Supersonic wind tunnel*. url: <https://www.tudelft.nl/lr/organisatie/afdelingen/flow-physics-and-technology/facilities/high-speed-wind-tunnels/tst-27-transonicsupersonic-windtunnel> (visited on 01/23/2023).
- [55] C. Camps Pons. "Experimental investigation of transonic buffet on swept wings: A comparative study between 2D and 3D flow and analysis of sweep angle influence using stereoscopic PIV and Background Oriented Schlieren". MA thesis. TU Delft, 2019.
- [56] N. van Rijswijk. "TST-27 Transonic Control". MA thesis. TU Delft, 2012.
- [57] T.J. Garbeff et al. "Experimental Visualizations of a Generic Launch Vehicle Flow Field: Time-Resolved Shadowgraph and Infrared Imaging". In: *55th AIAA Aerospace Sciences Meeting*. 2017, p. 1403.
- [58] F.F.J. Schrijer, A. Sciacchitano, and F. Scarano. "Spatio-temporal and modal analysis of unsteady fluctuations in a high-subsonic base flow". In: *Physics of Fluids* 26.8 (2014).
- [59] K.L. Goin and A. Pope. "High-speed wind tunnel testing". In: *New York, JOHN WILEY AND SONS, INC., 1965. p.320* (1965).
- [60] Ernad Bešliagić, Samir Lemeš, and Fuad Hadžikadunić. "Procedure for determining the wind tunnel blockage correction factor". In: *New Technologies, Development and Application III* 6. Springer. 2020, pp. 331–339.
- [61] C. Tropea et al. *Springer handbook of experimental fluid mechanics*. Vol. 1. Springer, 2007.
- [62] B. Schmidt. *Lecture notes in Schlieren Visualization for Ae 104b Experimental Methods*. CALTECH - California Institute of Technology, Dec. 2015.
- [63] M. Raffel, C.E. Willert, J. Kompenhans, et al. *Particle image velocimetry: a practical guide*. Vol. 2. Springer, 2018.
- [64] F.J. Donker Duyvis. "Laser sheet probe design for PIV in high speed wind tunnels". In: *Proc. PIVNET II International Workshop on the Application of PIV in Compressible Flows, Delft, the Netherlands*. 2005.
- [65] Z Sun. "Micro ramps in supersonic turbulent boundary layers: an experimental and numerical study". MA thesis. 2014.
- [66] D. Ragni et al. "Particle tracer response across shocks measured by PIV". In: *Experiments in fluids* 50 (2011), pp. 53–64.
- [67] F. Scarano. *Reader in Experimental Aerodynamics for AE4180 Flow Measurement Techniques*. TU Delft Faculteit Luchtvaart- en Ruimtevaarttechniek, Feb. 2013.
- [68] A. Melling. "Tracer particles and seeding for particle image velocimetry". In: *Measurement science and technology* 8.12 (1997), p. 1406.

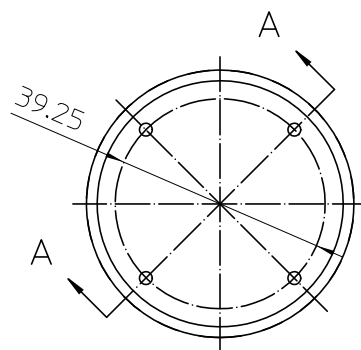
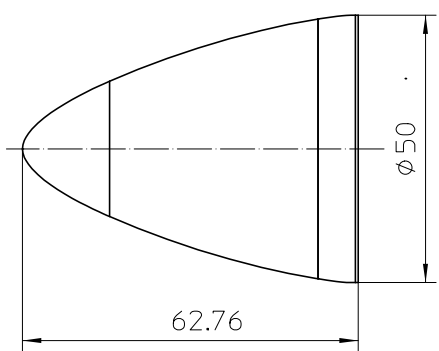
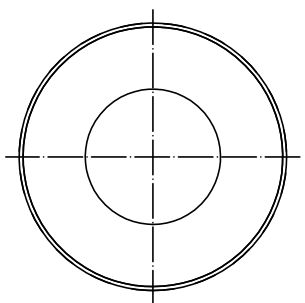
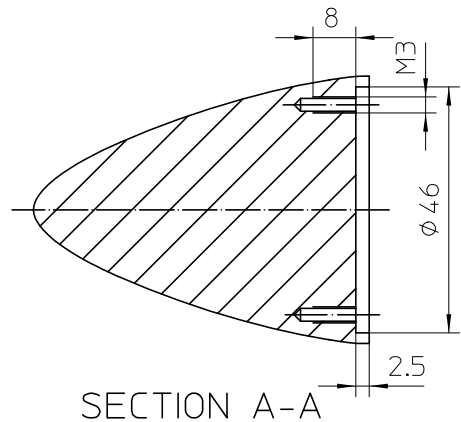
- [69] R.A. Humble, F. Scarano, and B.W. van Oudheusden. “Unsteady flow organization of a shock wave/turbulent boundary layer interaction”. In: *IUTAM Symposium on Unsteady Separated Flows and their Control: Proceedings of the IUTAM Symposium “Unsteady Separated Flows and their Control”, Corfu, Greece, 18–22 June 2007*. Springer, 2009, pp. 319–330.
- [70] F.F.J. Schrijer and F. Scarano. “Effect of predictor–corrector filtering on the stability and spatial resolution of iterative PIV interrogation”. In: *Experiments in fluids* 45 (2008), pp. 927–941.
- [71] S.G. Brust. “The Effects of Nozzle Length and Exhaust Plume Interaction on High-Speed Base Flows: An experimental investigation using Tomographic PIV”. MA thesis. TU Delft, 2017.
- [72] A. Sciacchitano and F. Scarano. “Elimination of PIV light reflections via a temporal high pass filter”. In: *Measurement Science and Technology* 25.8 (2014), p. 084009.
- [73] J. Westerweel and F. Scarano. “Universal outlier detection for PIV data”. In: *Experiments in fluids* 39 (2005), pp. 1096–1100.
- [74] R. Solana Perez. “On the unsteady development of the flow under transonic Buffet conditions: Experimental study of the interaction of shock and pressure waves using PIV and Schlieren visualization”. MA thesis. TU Delft, 2017.
- [75] P. Welch. “The use of fast Fourier transform for the estimation of power spectra: a method based on time averaging over short, modified periodograms”. In: *IEEE Transactions on audio and electroacoustics* 15.2 (1967), pp. 70–73.
- [76] L.M. Hudy et al. “Particle image velocimetry measurements of a two/three-dimensional separating/reattaching boundary layer downstream of an axisymmetric backward-facing step”. In: *43rd AIAA Aerospace Sciences Meeting and Exhibit*. AIAA Paper 2005-0114. 2005.
- [77] V. Gentile et al. “Afterbody effects on axisymmetric base flows”. In: *AIAA Journal* 54.8 (2016), pp. 2285–2294.



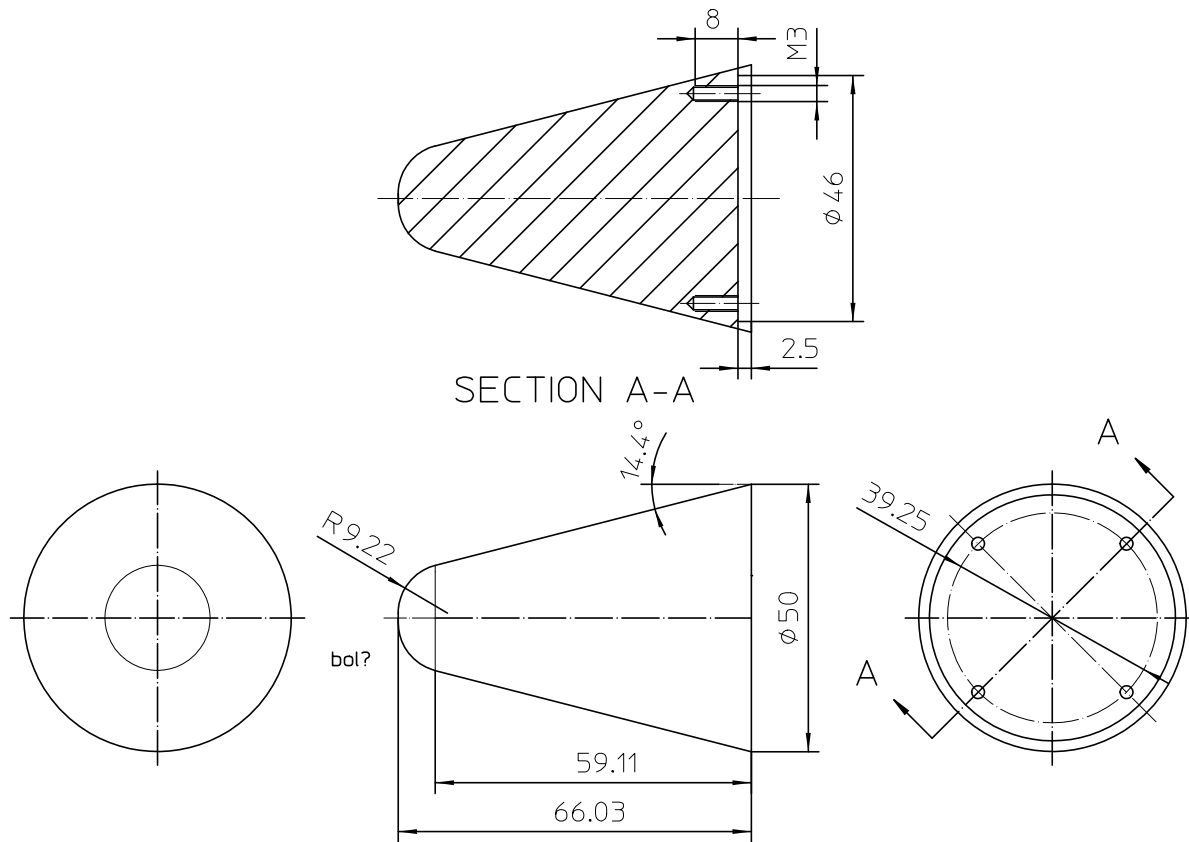


## Model Drawings

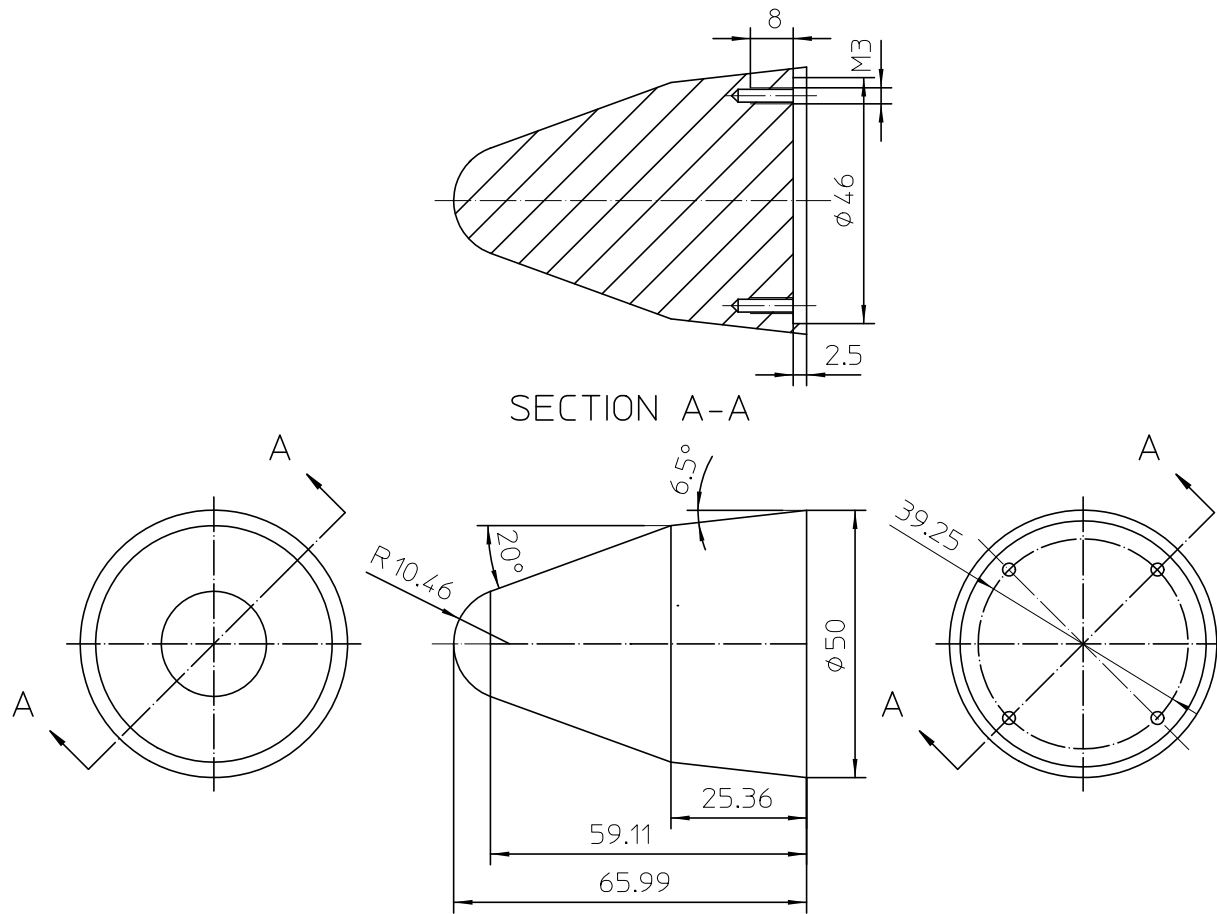
This section presents all the drawings with dimensions instrumental in the manufacturing process of all the pieces necessary for the model tested in this project.



	1	Head-A-Karman	Aluminium	ø 50
Pos. :	Aantal :	Benaming :	Materiaal :	Opmerking / Afmeting :
Schaal :	1:1	Datum :	Opmerkingen :	
Getekend:	F.J. Donker Duyvis	05-04-'23	Zwart Anodiseren	
Gecontr. :		tel. 87395		
Filename:	'CADfiles/'			
Benaming: Hammerhead Type A-Karman				
 <b>AEROSPACE ENGINEERING</b> <b>TU Delft</b>			Nummer	
			<b>A3 LR-</b>	
			Aantal bladen : 1    Blad nr. : 1	
Auteursrechten voorbeh. volgens de wet				

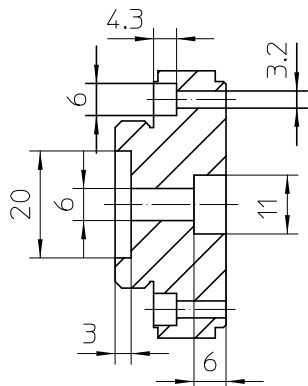


	1	Head-B-Conic	Aluminium	ø 50
Pos. :	Aantal :	Benaming :	Materiaal :	Opmerking / Afmeting :
Schaal :	1:1	Datum :	Opmerkingen :	
Getekend:	F.J. Donker Duyvis	05-04-'23	Zwart Anodiseren	
Gecontr. :		tel. 87395		
Filename:	'CADfiles/'			
Benaming: Hammerhead Type B-Conic				
 AEROSPACE ENGINEERING TUDelft			Nummer	
			A3 LR-	
			Auteursrechten voorbeh. volgens de wet	

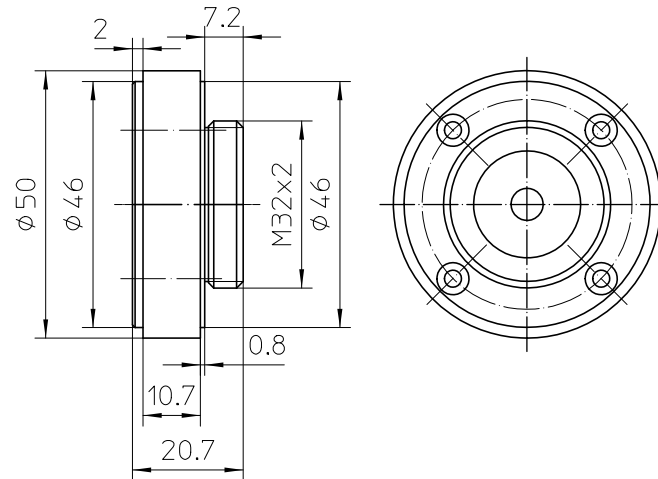
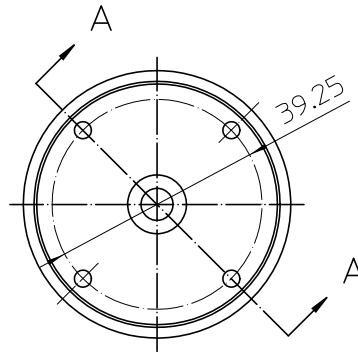


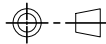
SECTION A-A

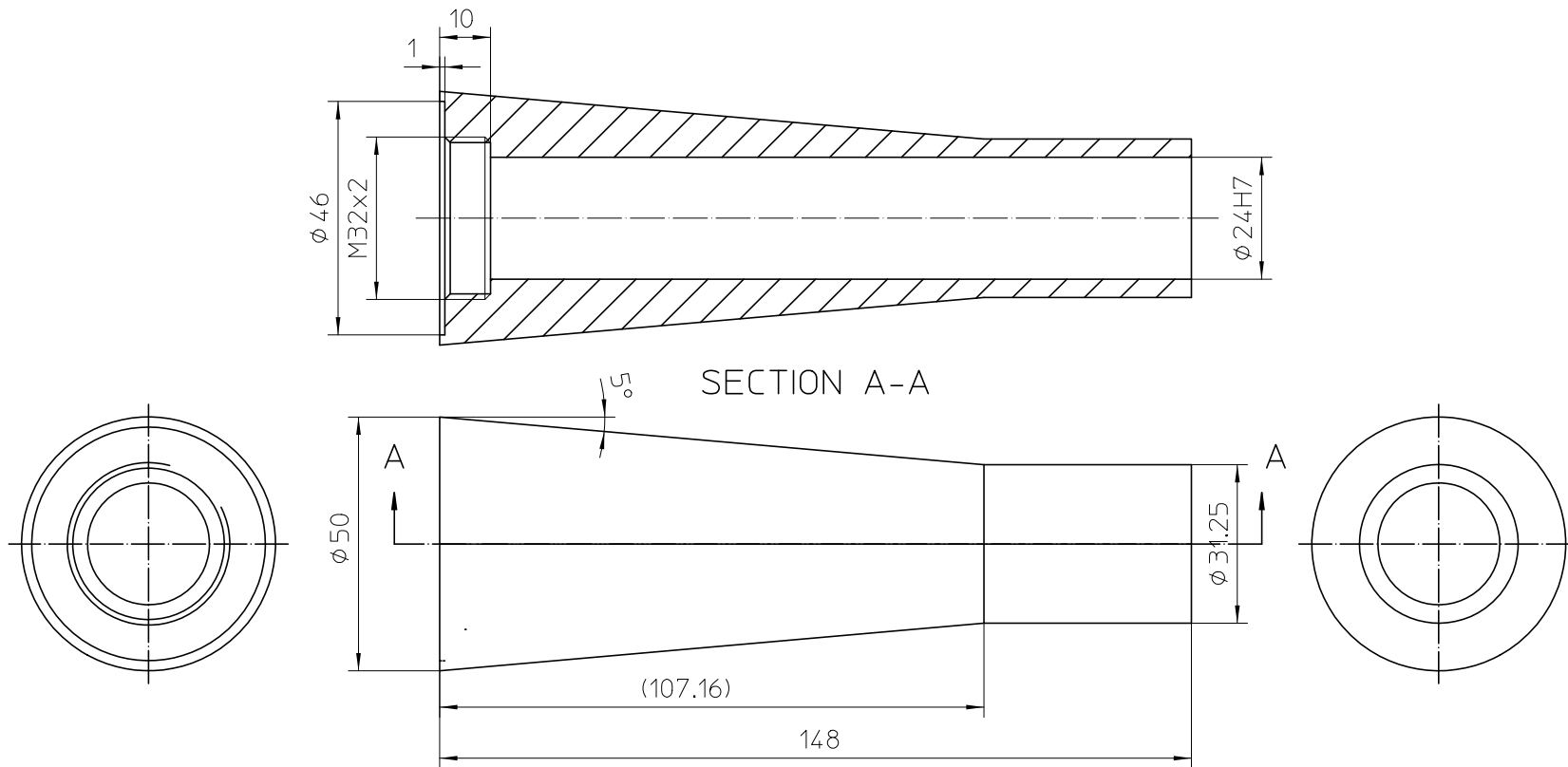
	1	Head-C-Biconic	Aluminium	ø 50
Pos. :	Aantal :	Benaming :	Materiaal :	Opmerking / Afmeting :
Schaal :	1:1	Datum :	Opmerkingen :	
Getekend :	F.J. Donker Duyvis	05-04-'23	Zwart Anodiseren	
Gecontr. :		tel. 87395		
Filename:	'CADfiles/'			
Benaming: Hammerhead Type C-Biconic				
 AEROSPACE ENGINEERING TUDelft			Nummer	
			<b>A3 LR-</b>	
			Aantal bladen : 1 Blad nr. : 1	
Auteursrechten voorbeh. volgens de wet				



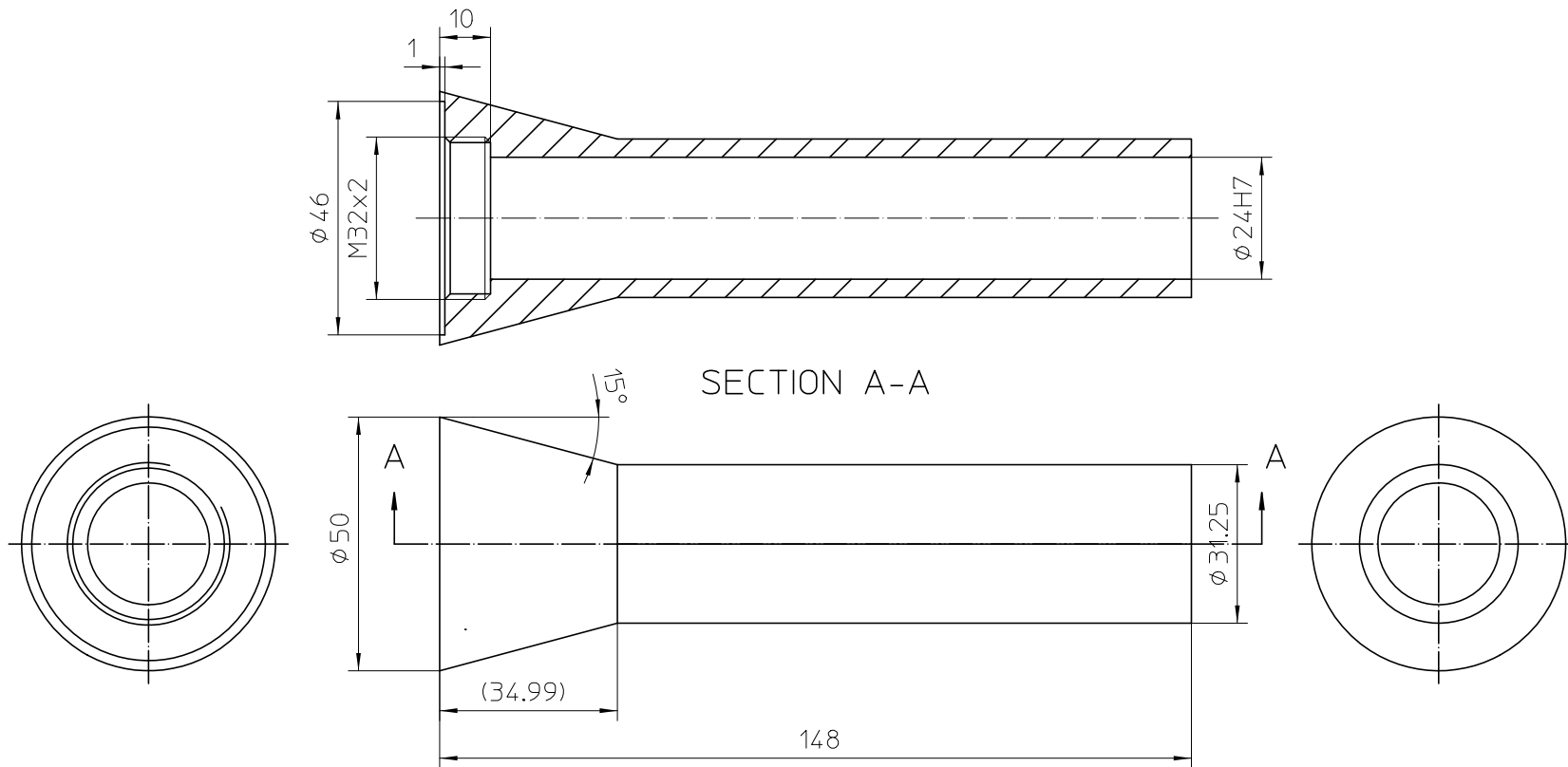
SECTION A-A



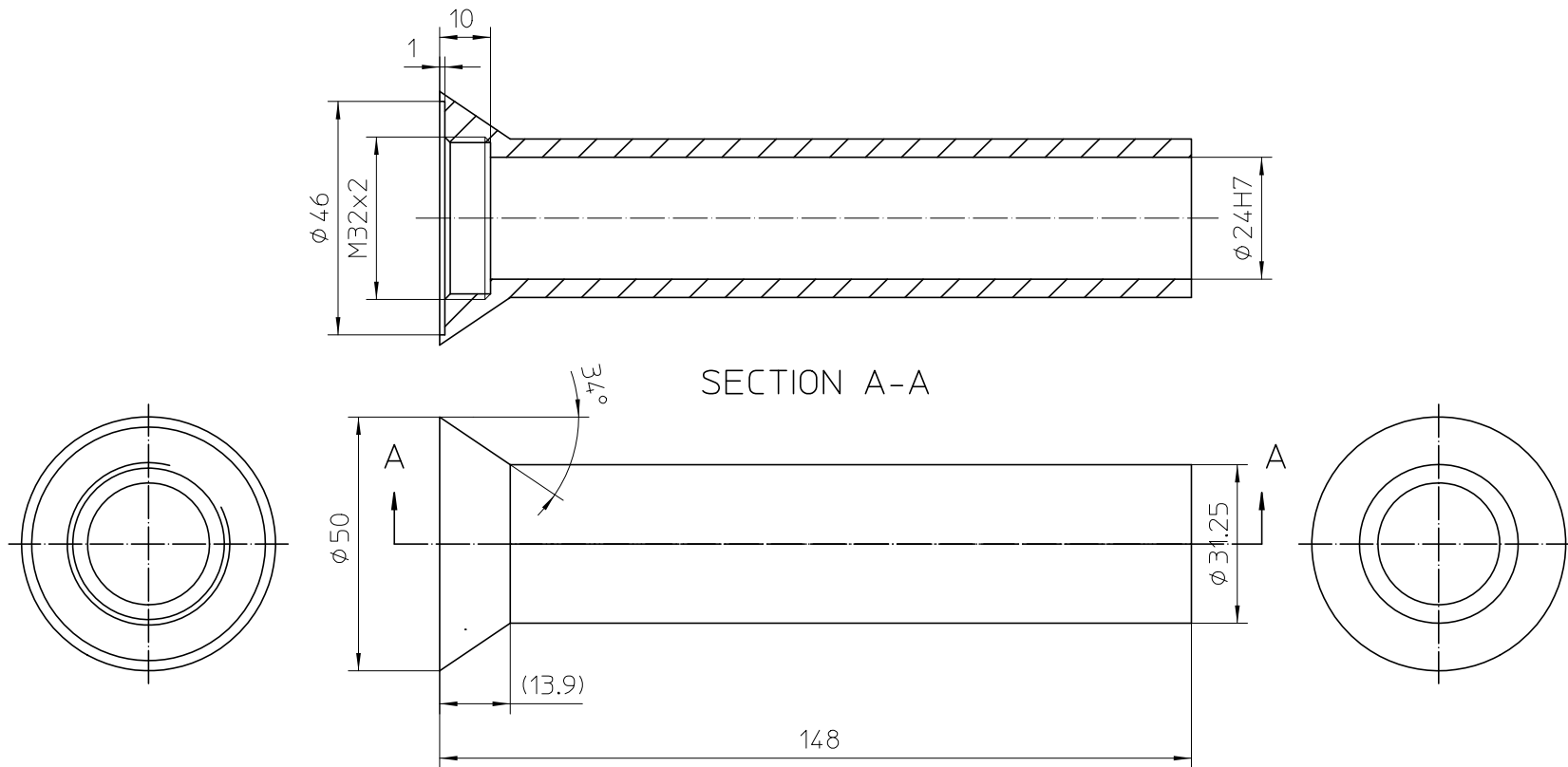
	1	Center cylindrical flange	Aluminium	ø 50
Pos. :	Aantal :	Benaming :	Materiaal :	Opmerking / Afmeting :
Schaal :	1:1	Datum :	Opmerkingen :	
Getekend:	F.J. Donker Duyvis	05-04-'23	Zwart Anodiseren	
Gecontr. :		tel. 87395		
Filename:	'CADfiles/'			
Benaming: Hammerhead Center Cylindrical Flange				
 AEROSPACE ENGINEERING TU Delft			Nummer	
			A3 LR-	
			Aantal bladen : 1 Blad nr. : 1	
Auteursrechten voorbeh. volgens de wet				



	1	Benaming	Aluminium	ø 50
Pos. :	Aantal :	Benaming :	Materiaal :	Opmerking / Afmeting :
Schaal :	1:1	Datum :	Opmerkingen :	
Getekend :	F.J. Donker Duyvis	5-04-'23		
Gecontr. :		tel. 87395		
Filename:	'CADfiles/'			
Benaming: Hammerhead Conical Fairing 5 degr.				
			Nummer	
			A3 LR-	
			Aantal bladen : 1 Blad nr. : 1	
Auteursrechten voorbeh. volgens de wet				



	1	Benaming	Aluminium	ø 50
Pos. :	Aantal :	Benaming :	Materiaal :	Opmerking / Afmeting :
Schaal :	1:1	Datum :	Opmerkingen :	
Getekend :	F.J. Donker Duyvis	5-04-'23		
Gecontr. :		tel. 87395		
Filename:	'CADfiles/'			
Benaming: Hammerhead Conical Fairing 15 degr.				
			Nummer	
			A3 LR-	
			Aantal bladen : 1 Blad nr. : 1	
Auteursrechten voorbeh. volgens de wet				



	1	Benaming	Aluminium	Ø 50
Pos. :	Aantal :	Benaming :	Materiaal :	Opmerking / Afmeting :
Schaal :	1:1	Datum :	Opmerkingen :	
Getekend:	F.J. Donker Duyvis	5-04-'23		
Gecontr. :		tel. 87395		
Filename:	'CADfiles/'			
Benaming: Hammerhead Conical Fairing 34 degr.				
 AEROSPACE ENGINEERING TUDelft			Nummer	
			A3 LR-	
			Aantal bladen : 1 Blad nr. : 1	
Auteursrechten voorbeh. volgens de wet				





# B

## Test Matrices

This section presents the complete test matrices for the various experimental campaigns. Each wind tunnel run includes detailed information about the model and setup configurations. Additionally, it provides the average Mach number, denoted as  $\overline{Ma}$ , and the corresponding standard deviation, represented as  $\sigma_{Ma}$ , along the entire run. This data helps to quantify and analyze the variability of the Mach number in each experimental campaign.

The various nose geometries are categorized as BC (bi-conic), SH (Sears-Haack or ogive), and C (conic). These designations are used to differentiate between the different shapes and configurations of the nose geometries employed in the experimental analysis.

The Schlieren and oil flow visualization campaigns were conducted in parallel, which is why the numbering of the runs follows that specific sequence. This means that the numbering of the runs corresponds to the order in which the Schlieren and oil flow visualization experiments were performed concurrently.

Finally, it must be noted that the results from run 8 at the PIV campaign could not be used as the transition strip partially flew in the middle of the run, as shown and discussed in section 3.2.

**Table B.1:** Oil flow visualisation campaign full test matrix.

Run	Nose	BT [deg]	AoA [deg]	p [bar]	Ma	$\overline{Ma}$	$\sigma_{Ma}$
3	BC	34	0	2	0.7	0.7001	$1.00 \cdot 10^{-3}$
27	BC	34	4	2	0.7	0.7056	$0.92 \cdot 10^{-3}$
28	BC	34	4	2	0.8	0.8003	$1.50 \cdot 10^{-3}$
29	BC	34	0	2	0.7	0.6996	$7.30 \cdot 10^{-3}$
30	BC	34	0	2	0.8	0.8027	$3.30 \cdot 10^{-3}$
31	SH	34	0	2	0.8	0.8051	$1.10 \cdot 10^{-3}$
32	C	34	0	2	0.8	0.7979	$1.10 \cdot 10^{-3}$
34	BC	34	0	2	0.7	0.7002	$7.19 \cdot 10^{-4}$

**Table B.2:** Schlieren visualisation campaign full test matrix.

Run	Nose	BT [deg]	Ma	AoA [deg]	f [Hz]	Exp. [ $\mu$ s]	Lens [mm]	p [bar]	Ma	$\sigma_{Ma}$
1	BC	34	0.7	0	5000	58.22	300	2	0.7002	$8.48 \cdot 10^{-4}$
2	BC	34	0.7	0	5000	49.02	300	2	0.7002	$1.10 \cdot 10^{-3}$
4	BC	34	0.8	0	5000	49.02	300	2	0.8031	$5.40 \cdot 10^{-3}$
5	BC	34	0.8	0	5000	49.02	300	2	0.8001	$6.91 \cdot 10^{-4}$
6	BC	5	0.7	0	5000	49.02	300	2	0.7022	$6.76 \cdot 10^{-4}$
7	BC	5	0.8	0	5000	49.02	300	2	0.7996	$6.70 \cdot 10^{-3}$
8	BC	15	0.7	0	5000	49.02	300	2	0.7016	$6.48 \cdot 10^{-4}$
9	BC	15	0.8	0	5000	49.02	300	2	0.8012	$7.25 \cdot 10^{-4}$
10	C	34	0.7	0	5000	49.02	300	2	0.7014	$6.86 \cdot 10^{-4}$
11	C	34	0.8	0	5000	49.02	300	2	0.7994	$7.37 \cdot 10^{-4}$
12	SH	34	0.7	0	5000	49.02	300	2	0.7013	$9.42 \cdot 10^{-4}$
13	SH	34	0.8	0	5000	49.02	300	2	0.8021	$9.74 \cdot 10^{-4}$
14	SH	5	0.7	0	5000	49.02	300	2	0.7028	$1.00 \cdot 10^{-3}$
15	SH	5	0.8	0	5000	49.02	300	2	0.8000	$7.40 \cdot 10^{-3}$
16	SH	34	0.7	4	5000	49.02	300	2	0.7020	$1.00 \cdot 10^{-3}$
17	SH	34	0.8	4	5000	49.02	300	2	0.8024	$2.90 \cdot 10^{-3}$
18	BC	34	0.6	4	5000	49.02	300	2	0.6020	$9.64 \cdot 10^{-4}$
19	BC	34	0.7	4	5000	49.02	300	2	0.7009	$6.72 \cdot 10^{-4}$
20	BC	34	0.8	4	5000	49.02	300	2	0.8028	$5.50 \cdot 10^{-3}$
21	BC	5	0.7	4	5000	49.02	300	2	0.7024	$1.60 \cdot 10^{-3}$
22	BC	5	0.8	4	5000	49.02	300	2	0.7996	$7.50 \cdot 10^{-3}$
23	BC	15	0.7	4	5000	49.02	300	2	0.7020	$7.61 \cdot 10^{-4}$
24	BC	15	0.8	4	5000	49.02	300	2	0.8015	$8.62 \cdot 10^{-4}$
25	C	34	0.7	4	5000	49.02	300	2	0.7032	$1.10 \cdot 10^{-3}$
26	C	34	0.8	4	5000	49.02	300	2	0.7987	$3.70 \cdot 10^{-3}$
33	BC	34	0.7	0	5000	49.02	300	2	0.7002	$1.10 \cdot 10^{-3}$

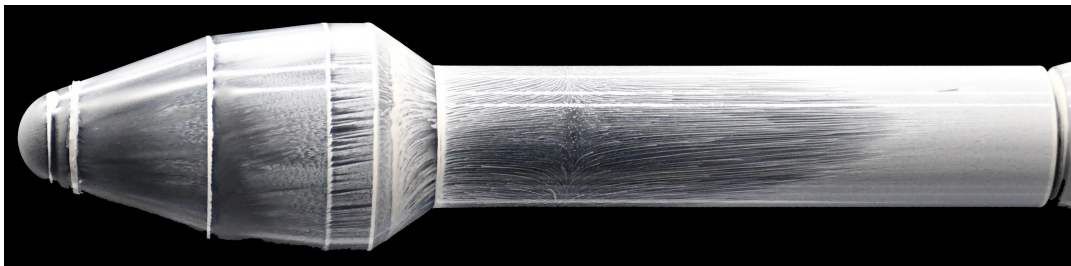
**Table B.3:** PIV campaign full test matrix.  $N$  refers to the number of images taken per run.

Run	Nose	BT [deg]	Ma	AoA [deg]	p [bar]	f [Hz]	$\Delta t$ [ $\mu$ s]	N	Ma	$\sigma_{Ma}$
1	BC	34	0.7	0	2	5	1.5	200	0.6995	$6.30 \cdot 10^{-3}$
2	BC	34	0.7	0	2	5	1.5	200	0.6997	$5.60 \cdot 10^{-3}$
3	BC	34	0.8	0	2	5	1.5	250	0.7993	$6.60 \cdot 10^{-3}$
4	BC	34	0.8	0	2	5	1.5	250	0.7988	$7.00 \cdot 10^{-3}$
5	BC	15	0.7	0	2	5	1.5	250	0.6999	$6.40 \cdot 10^{-3}$
6	BC	15	0.7	0	2	5	1.5	250	0.6997	$3.60 \cdot 10^{-3}$
7	BC	15	0.8	0	2	5	1.5	250	0.7989	$7.60 \cdot 10^{-3}$
8	BC	15	0.8	0	2	5	1.5	250	0.8001	$3.70 \cdot 10^{-3}$
11	BC	34	0.8	4	2	5	1.5	250	0.8004	$3.00 \cdot 10^{-3}$
12	BC	34	0.8	4	2	5	1.5	250	0.8003	$2.80 \cdot 10^{-3}$
13	BC	15	0.7	4	2	5	1.5	250	0.6999	$3.60 \cdot 10^{-3}$
15	BC	15	0.8	4	2	5	1.5	300	0.8002	$2.80 \cdot 10^{-3}$
16	BC	15	0.8	4	2	5	1.5	150	0.8009	$6.30 \cdot 10^{-4}$

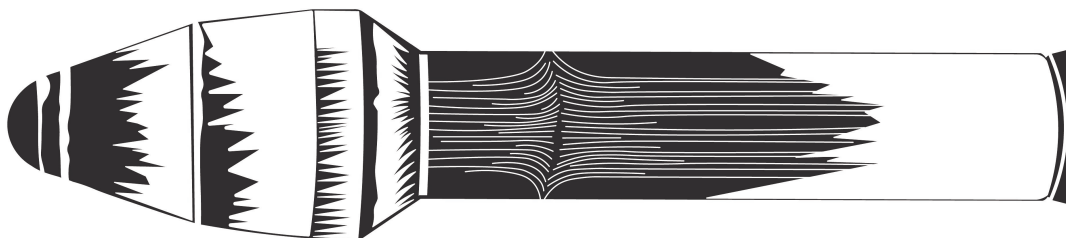
# C

## Oil Flow Visualisation Images and Diagrams Comparison

This chapter compiles all the oil flow visualisation pictures taken after each run and the schematic representation done for each case. The order in which are presented correspond to the run numbering presented in Table B.1.

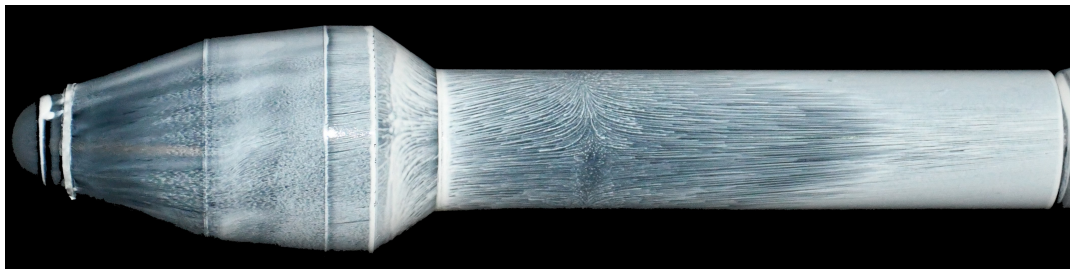


(a) Photography

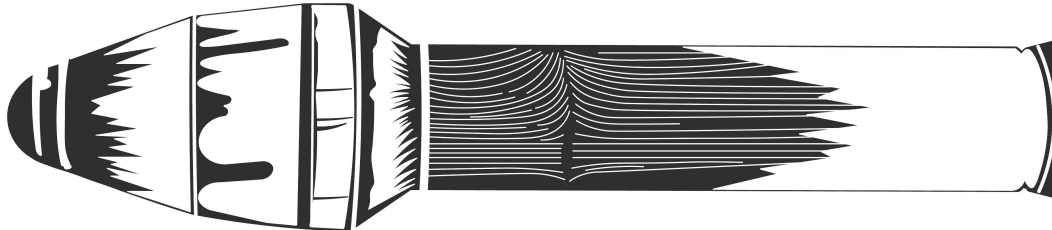


(b) Schematic representation

**Figure C.1:** Comparison between real photography and schematic representation of the oil flow patterns obtained for run 27 at Table B.1: benchmark case based on Coe and Nute's model 11 [34] with bi-conic nose, boat-tail of 34-degrees,  $Ma = 0.7$  and  $AoA = 4$  degrees.

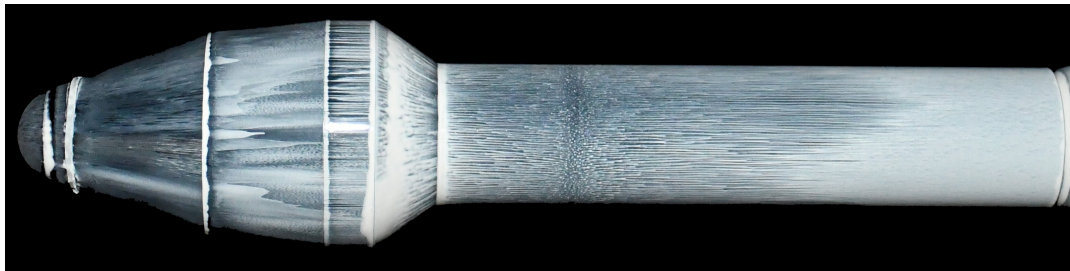


(a) Photography

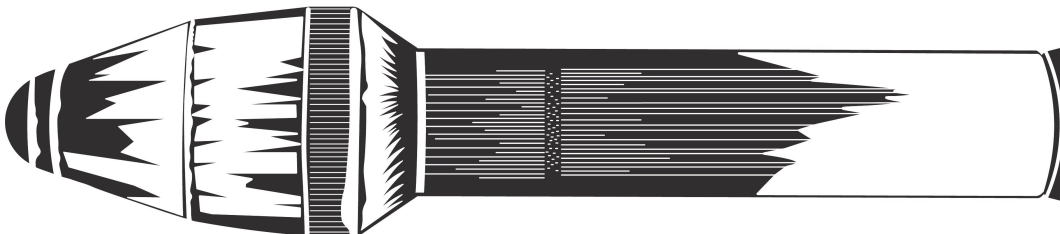


(b) Schematic representation

**Figure C.2:** Comparison between real photography and schematic representation of the oil flow patterns obtained for run 28 at Table B.1: benchmark case based on Coe and Nute's model 11 [34] with bi-conic nose, boat-tail of 34-degrees,  $Ma = 0.8$  and  $AoA = 4$  degrees.

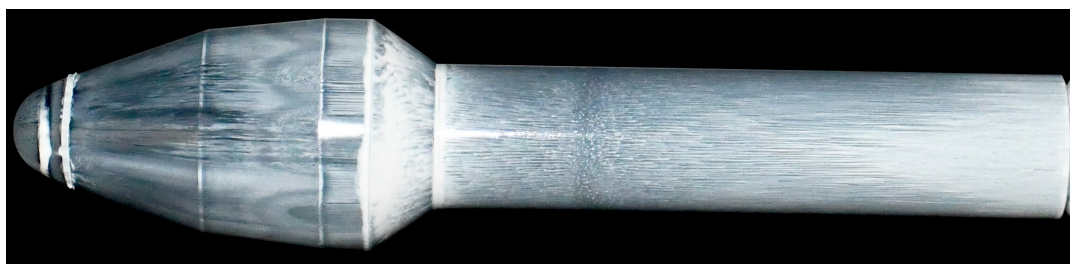


(a) Photography

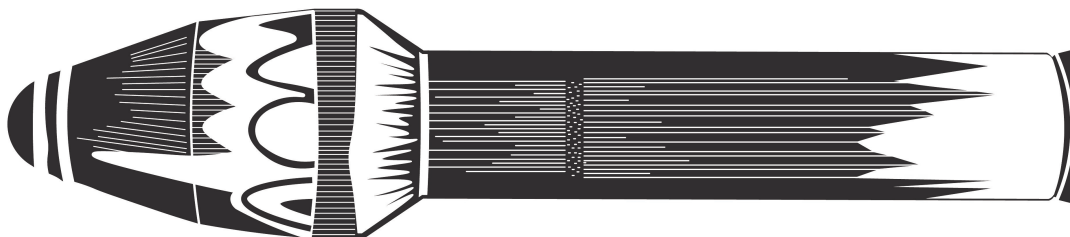


(b) Schematic representation

**Figure C.3:** Comparison between real photography and schematic representation of the oil flow patterns obtained for run 29 at Table B.1: benchmark case based on Coe and Nute's model 11 [34] with bi-conic nose, boat-tail of 34-degrees,  $Ma = 0.7$  and  $AoA = 0$  degrees.

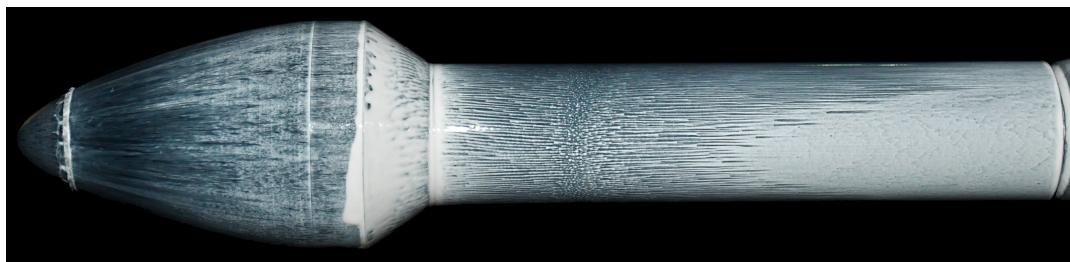


(a) Photography

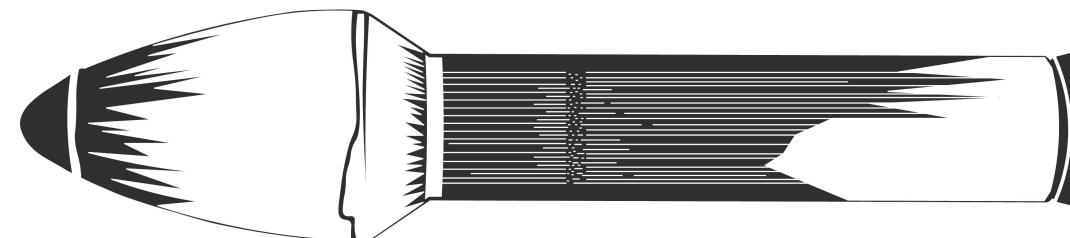


(b) Schematic representation

**Figure C.4:** Comparison between real photography and schematic representation of the oil flow patterns obtained for run 30 at Table B.1: benchmark case based on Coe and Nute's model 11 [34] with bi-conic nose, boat-tail of 34-degrees,  $Ma = 0.8$  and  $AoA = 0$  degrees.

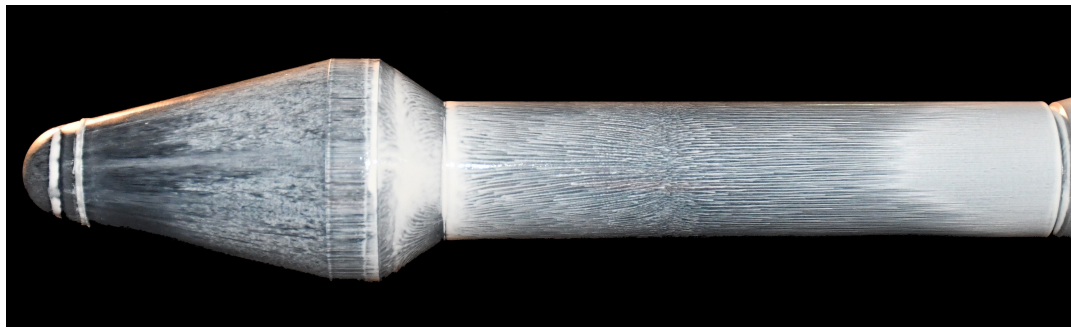


(a) Photography

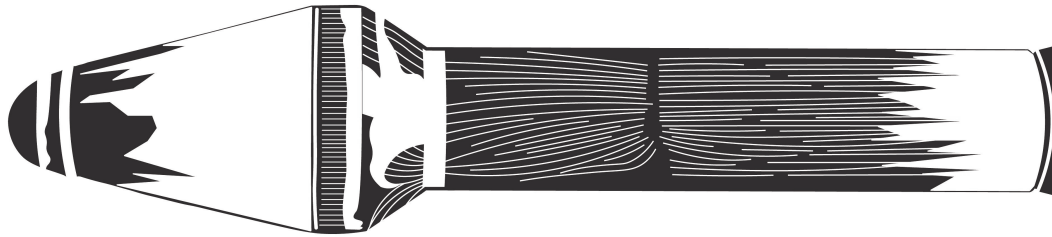


(b) Schematic representation

**Figure C.5:** Comparison between real photography and schematic representation of the oil flow patterns obtained for run 31 at Table B.1: ogive (based on Sears-Haack curve) nose, boat-tail of 34-degrees,  $Ma = 0.8$  and  $AoA = 0$  degrees.

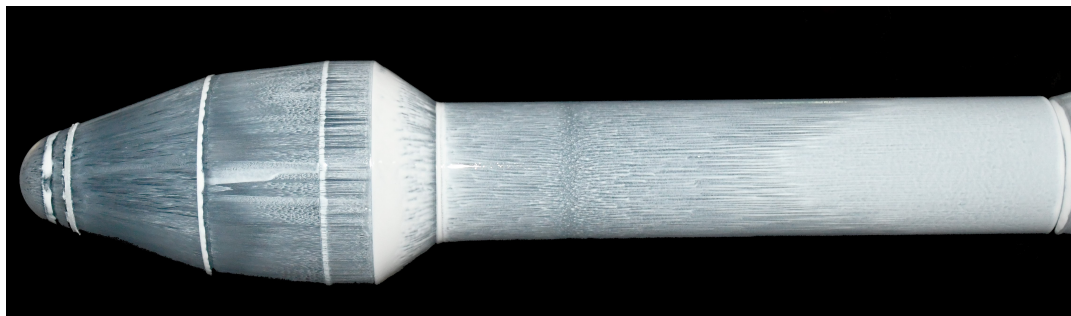


(a) Photography

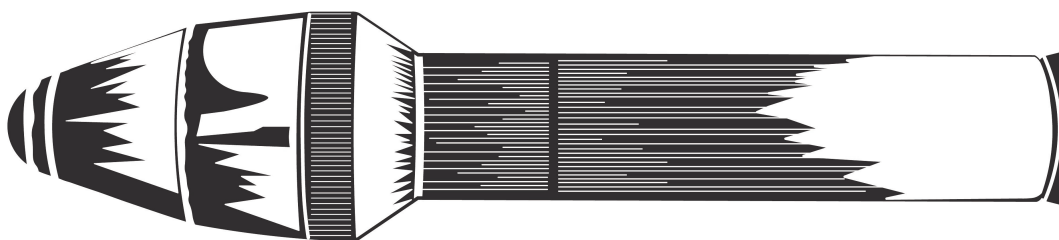


(b) Schematic representation

**Figure C.6:** Comparison between real photography and schematic representation of the oil flow patterns obtained for run 32 at Table B.1: conic nose, boat-tail of 34-degrees,  $Ma = 0.8$  and  $AoA = 0$  degrees.



(a) Photography



(b) Schematic representation

**Figure C.7:** Comparison between real photography and schematic representation of the oil flow patterns obtained for run 34 at Table B.1: benchmark case based on Coe and Nute's model 11 [34] with bi-conic nose, boat-tail of 34-degrees,  $Ma = 0.7$  and  $AoA = 0$  degrees.